National Library of Canada
Bibliothèque nationale du Canada

Canadian Theses Service
Services des thèses canadiennes

Ottawa, Canada
K1A 0N4

CANADIAN THESES

THÈSES CANADIENNES

NOTICE

The quality of this microfiche is heavily dependent upon the quality of the original thesis submitted for microfilming. Every effort has been made to ensure the highest quality of reproduction possible.

If pages are missing, contact the university which granted the degree.

Some pages may have indistinct print especially if the original pages were typed with a poor typewriter ribbon or if the university sent us an inferior photocopy.

Previously copyrighted materials (journal articles, published tests, etc.) are not filmed.

Reproduction in full or in part of this film is governed by the Canadian Copyright Act, R.S.C. 1970, c. C-30.

AVIS

La qualité de cette microfiche dépend grandement de la qualité de la thèse soumise au microfilmage. Nous avons tout fait pour assurer une qualité supérieure de reproduction.

S'il manque des pages, veuillez communiquer avec l'université qui a conféré le grade.

La qualité d'impression de certaines pages peut laisser à désirer, surtout si les pages originales ont été dactylographiées à l'aide d'un ruban usé ou si l'université nous a fait parvenir une photocopie de qualité inférieure.

Les documents qui font déjà l'objet d'un droit d'auteur (articles de revue, examens publiés, etc.) ne sont pas microfilmés.

La reproduction, même partielle, de ce microfilm est soumise à la Loi canadienne sur le droit d'auteur, SRC 1970, c. C-30.

THIS DISSERTATION HAS BEEN MICROFILMED EXACTLY AS RECEIVED

LA THÈSE A ÉTÉ MICROFILMÉE TELLE QUE NOUS L'AVONS REÇUE

NL-339 (r.86/06)

Canada

KINETICS OF RECOVERY AND RECRYSTALLIZATION OF HOT WORKED COPPER UNDER STRESS RELAXATION

Lucio Vazquez-Briseño

A Thesis

in

The Department

of

Mechanical Engineering

Presented in Partial Fulfillment of the Requirements
for the Degree of Doctor of Philosophy at
Concordia University
Montréal, Québec, Canada

January 1986

© Lucio Vazquez-Briseño, 1985

Permission has been granted to the National Library of Canada to microfilm this thesis and to lend or sell copies of the film.

The author (copyright owner) has reserved other publication rights, and neither the thesis nor extensive extracts from it may be printed or otherwise reproduced without his/her written permission.

L'autorisation a été accordée à la Bibliothèque nationale du Canada de microfilmer cette thèse et de prêter ou de vendre des exemplaires du film.

L'auteur (titulaire du droit d'auteur) se réserve les autres droits de publication; ni la thèse ni de longs extraits de celle-ci ne doivent être imprimés ou autrement reproduits sans son autorisation écrite.

ISBN 0-315-30692-0

ABSTRACT

Kinetics of Recovery and Recrystallization of Hot Worked Copper under Stress Relaxation

Lucio Vazquez-Briseño, Ph.D.
Concordia University, 1985

The kinetics of recovery and recrystallization of ETP copper under stress relaxation is studied after high temperature compression and torsion. One group of specimens was strained in compression at 450°C, $1.8X10^{-3}$ s^{-1} and 540°C, $9.3X10^{-2}$ s^{-1} (Z_1); a second group in both compression and torsion at 450°C, $1.8X10^{-1}$ s^{-1} ($100Z_1$); and a third group in torsion at 500°C, 1.8 s^{-1} ($100Z_1$) or 450°C, 1.8 s^{-1} ($1000Z_1$). After straining to 0.15, the samples of the first two groups were stress relaxed or load-free annealed at the deformation temperature, while those of the third group were only stress-free annealed. The progress of restoration was followed by mechanical and microscopic methods. Recovery and recrystallization occurred under both relaxation and load-free annealing. The former followed an exponential law and the latter the Mehl-Avrami relationship.

The rates of recovery and recrystallization under relaxation were lower and higher, respectively, than for load-free annealing. Plastic flow in stress relaxation, by generating some degree of hardening, retards recovery which in turn enhances recrystallization. The restoration kinetics in compression and in torsion are similar but show differences related to the restoration gradient. The stress relaxation curve can be used to determine approximately the amount of softening and the onset and end of recrystallization.

ACKNOWLEDGEMENTS

The author would like to express his sincere appreciation and gratitude to Prof. H.J. McQueen, director of this research, for his invaluable advice and encouragement. He thanks his fellow graduate students at Concordia University for providing a stimulating atmosphere. He is grateful to Ms. D. Rogers for word processing his thesis and Ms. M. McQueen for editing it.

The author would like to thank Prof. J.J. Jonas for making available laboratory facilities, for encouragement and for partial funding during the final year of this research. He acknowledges the help provided by the graduate students at McGill University.

He expresses his thanks to Dr. G. Carpenter for his advice, to Mr. Mark Charest for his guidance in the electronmicroscopy and to the Physical Metallurgy Research Laboratory CANMET EMR for the use of its facilities.

Thanks are due to the Consejo Nacional de Ciencia y Technologia de Mexico for the award of a Graduate Fellowship. He acknowledges with gratitude the financial

support received from the Natural Sciences and Engineering Research Council of Canada and Fonds pour la Formation de Cherches et l'Aide a la Recherche.

TABLE OF CONTENTS

		Page
ABSTRACT		iii
ACKNOWLEDGEMENTS		v
TABLE OF CONTENTS		vii
LIST OF FIGURES		xi
LIST OF TABLES		xviii
LIST OF SYMBOLS		xix
CHAPTER 1.	INTRODUCTION	1
CHAPTER 2.	DEFORMATION, RESTORATION AND RELAXATION PROCESSES AT HIGH TEMPERATURE	3
2.1	Background on Stress Relaxation	3
2.1.1	Definitions	3
2.1.2	Stress Relaxation at Low and Medium Temperatures, Stable Microstructures	5
2.1.3	High Temperature Relaxation	11
2.2	Hardening and Softening During High Temperature Deformation	16
2.2.1	Hardening and Softening	16
2.2.2	Hot Working	17
2.2.2.1	Dynamic Recovery Flow Curves	18
2.2.2.2	Flow Curves for Dynamic Recovery and Recrystallization	21
2.2.2.3	Creep Curves	23
2.2.2.4	Stress Relaxation Phenomena at High Temperature	26
2.2.2.5	Stress, Strain Rate and Temperature Relations	27
2.2.2.5.1	Empirical Relationships	27
2.2.2.5.2	Flow Stress Relationships	29
2.2.2.6	Flow Stresses at High Temperatures	30
2.2.2.7	Yield and Steady-State Stresses at High Temperatures	31
2.3	Restoration After High Temperature Deformation	32
2.3.1	Microstructure After Deformation	32
2.3.2	Static Recovery	34
2.3.2.1	Static Recovery Mechanisms	36
2.3.2.2	Static Recovery Kinetics	37
2.3.3	Static Recrystallization	40
2.3.3.1	Static Recrystallization Mechanisms	42
2.3.3.2	Static Recrystallization Kinetics	43

		Page
2.3.3.2.1	Johnson and Mehl Theory	43
2.3.3.2.2	Avrami's Theory	44
2.4	Restoration During Hot Working	45
2.4.1	Dynamic Recovery	45
2.4.1.1	Dynamic Recovery Mechanisms	45
2.4.1.2	Dynamic Recovery Kinetics	47
2.4.2	Dynamic Recrystallization	47
2.4.2.1	Dynamic Recrystallization Mechanisms	49
2.4.2.2	Dynamic Recrystallization Kinetics	49
2.4.3	Metadynamic Recrystallization	50
CHAPTER 3.	EXPERIMENTAL EQUIPMENT, MATERIALS, AND METHODS WITH PROCEDURES FOR ANALYSIS OF DATA	53
3.1	Experimental Equipment	53
3.1.1	Compression Testing	53
3.1.1.1	Testing Assembly	53
3.1.1.2	Compression Tools for High Temperature	54
3.1.1.3	Control of Test Variables	53
3.1.1.3.1	Temperature Control	54
3.1.1.3.2	Atmosphere Control	54
3.1.1.3.3	Strain Rate Control	56
3.1.1.4	Instron Monitoring, Data Acquisition and Handling	57
3.1.2	Torsion Testing	58
3.1.2.1	Testing Assembly	58
3.1.2.2	Torsion Tools for High Temperature	61
3.1.2.3	Control of Test Variables	61
3.1.2.3.1	Temperature Control	61
3.1.2.3.2	Atmosphere Control	61
3.1.2.3.3	Strain, Strain Rate and Stress Control	62
3.1.2.4	Machine Monitoring, Data Acquisition and Handling	63
3.2	Experimental Material	64
3.2.1	Machining	64
3.2.1.1	Compression Samples	64
3.2.1.2	Torsion Samples	66
3.2.2	Heat Treatment	68
3.3	Experimental Methods	70
3.3.1	Compression Tests	70
3.3.2	Torsion Tests	72
3.3.3	Advantages of Compression and Torsion Tests	72
3.3.4	Test Conditions	74
3.3.5	Preparation of Metallographic Samples	76
3.3.6	Preparation of Specimens for Electronmicroscopy	77
3.3.7	Metallographic Measurements	78
3.3.7.1	Grain Size	78
3.3.7.2	Volume Fraction Recrystallized	84
3.3.8	Electronmicroscopic Measurements and Observations	85

		Page
3.3.8.1	Subgrain Misorientation Measurement	86
3.4	Analysis of Data	88
3.4.1	Yield Stress Determination Methods	88
3.4.1.1	The Back Extrapolation Method	88
3.4.1.2	The Offset Yield Stress Method	89
3.4.2	Fractional Softening	90
3.4.2	Fractional Relaxation	92
3.4.4	Recrystallization Kinetic Curves	92
3.4.4.1	The Mehl-Avrami Law	93
3.4.4.2	Modified Mehl-Avrami Law, Sequential Mechanisms	95
3.4.4.3	Modified Mehl-Avrami Law, Parallel Mechanisms	97
3.4.5	Plotting of the Recovery Kinetic Curve	99
CHAPTER 4.	EXPERIMENTAL RESULTS	108
4.1	Flow Curves for Initial Deformation and Reloading	108
4.1.1	General Description	108
4.1.2	Effect of Stress Relaxation	109
4.1.3	Influence of Temperature	112
4.1.4	Effect of Strain Rate	112
4.1.5	Compression and Torsion Flow Curves	115
4.1.6	Torsion Flow Curves at High Strain Rates	115
4.2	Stress Relaxation Curves	118
4.2.1	Fractional Relaxation	125
4.3	Fractional Softening From Mechanical Testing	125
4.3.1	General Description	125
4.3.2	Stress Relaxation and Time for Full Softening	128
4.3.3	Effect of Temperature on the Time for Full Softening	130
4.3.4	Effect of Strain Rate on the Time for Full Softening	132
4.3.5	Compression and Torsion Softening Curves	133
4.3.6	Torsion Softening Curves at High Strain Rates	133
4.3.7	Softening Kinetics	135
4.4	Recrystallization	139
4.4.1	Volume Fraction Recrystallized	139
4.4.2	Comparison of Softening and Recrystallization	141
4.4.3	Recrystallization Kinetics	141
4.4.4	Metallography	142
4.4.4.1	Hot Worked and Partially Recrystallized Microstructures	142
4.4.4.2	Fully Recrystallized Microstructures	154
4.5	Recovery	161
4.5.1	Recovery Kinetics	161

		Page
4.5.2	Analysis of the Substructure	161
4.5.3	Misorientations	172
CHAPTER 5.	DISCUSSION	174
5.1	Effect of the Experimental Variables on the Restoration Kinetics	174
5.1.1	The Unloaded Tests	174
5.1.2	The Stress Relaxation Tests	181
5.1.3	Stress Relaxation and Structural Changes	184
5.1.4	Comparison of Relaxation and Unloaded Tests	186
5.1.5	Comparison with Other Work	189
5.1.5.1	Effect of Decreased Strain on Restoration Kinetics	189
5.1.5.2	Restoration under Creep or Constant Strain Rate	191
CHAPTER 6.	CONCLUSIONS	195
REFERENCES		199
APPENDIX A.	ADDITIONAL EXPERIMENTAL DATA	207

LIST OF FIGURES

	Page
Fig. 2.1 Relaxation curve in semi-logarithmic coordinates. (after Oding and Tseitlin (22))	8
Fig. 2.2 Influence of strain rate and temperature on the shape of the flow curve of aluminum. Shape characteristic of DRV. Dotted line: $\dot{\varepsilon} = 1.7X10^{-2}$ s^{-1}. Continuous line: $\varepsilon = 1.7X10^{-4}$ s^{-1}. (from Kocks et.al. (42))	19
Fig. 2.3 Effect of strain rate on the flow curves of austenitic steel at 1100°C. Shape characteristic of DRX. (after Rossard and Blain (50))	22
Fig. 2.4a Schematic representation of a creep-rupture curve. (Garofalo (40))	25
Fig. 2.4b Dynamic recrystallization during creep at high stress and temperature (upper curve) and dynamic recovery during creep at low stresses (lower curve). (McQueen and Jonas (37))	25
Fig. 3.1 The hot compression train. (after Weiss (154))	53
Fig. 3.2 The hot compression tools. (after Weiss (154))	55
Fig. 3.3 The hot torsion machine. (after Fulop et.al. (158))	59
Fig. 3.4 Strain control and measurement subsystem. (after Fulop et.al. (158))	59
Fig. 3.5 Torque cell assembly. (after Fulop et.al. (158))	60
Fig. 3.6 Schematic diagram of the control and data acquisition systems. (after Fulop et.al. (158))	60
Fig. 3.7 Compression specimen dimensions and groove geometry.	65

Page

Fig. 3.8 Torsion specimen dimensions. 67

Fig. 3.9 Initial and reloading flow curves; 0.001 offset yield stress method. 71

Fig. 3.10 Test pattern for intercept counting (ASTM E-112). 79

Fig. 3.11 Grain size worksheet (ASTM E-112). 80

Fig. 3.12 Chart for direct determination of mean intercept distance from intercept count on 500 mm test pattern (ASTM E-112). 81

Fig. 3.13 Chart for determination of confidence limit on estimation of mean intercept distance (ASTM E-112). 83

Fig. 3.14 Kikuchi patterns of two neighboring subgrains. 87

Fig. 3.15a Fraction recrystallized X_R as a function of log time showing incubation time. 94

Fig. 3.15b Fractional softening curve (X) for sequential recovery X_r and recrystallization X_R. (after Petkovic (81)) 96

Fig. 3.15c Fractional softening (X MECH) and volume fraction recrystallized (X_R MICR) curves for simultaneous recovery X_r and recrystallization; present work. 98

Fig. 3.16a Procedure for the determination of intersection stress to determine t_i. 100

Fig. 3.16b Preliminary recovery kinetic curve of σ_r vs log t to determine t'_o. 102

Fig. 3.16c Intermediate recovery kinetic curve to reevaluate t'_o. 103

Page

Fig. 4.1a Initial and reloading flow curves for the compression condition 450°C, $1.8X10^{-3}$ s^{-1} (Z_1). Unloaded (UL) annealing with fractional softenings for various intervals. 105

Fig. 4.1b Stress relaxation (SR) with fractional softenings and final relaxed stresses for various intervals. 106

Fig. 4.2a Initial and reloading flow curves for the compression condition 540°C, $9.3X10^{-2}$ s^{-1} (Z_1). UL annealing with fractional softenings for various intervals. 107

Fig. 4.2b Stress relaxation with fractional softenings and final relaxed stresses for various intervals. 108

Fig. 4.3a Initial and reloading flow curves for the compression condition 450°C, $1.8X10^{-1}$ s^{-1} (100 Z_1). UL annealing with fractional softenings for various intervals. 110

Fig. 4.3b Stress relaxation with fractional softenings and final relaxed stresses for various intervals. 111

Fig. 4.4a Initial and reloading flow curves for the torsion condition 450°C, $1.8X10^{-1}$ s^{-1} ($100Z_1$) UL annealing with fractional softenings for various intervals. 113

Fig. 4.4b Stress relaxation with fractional softenings and final relaxed stresses for various intervals. 114

Fig. 4.5 Initial and reloading flow curves for the torsion condition 450°C, 1.8 s^{-1} (1000 Z_1). UL annealing with fractional softenings for various intervals. 116

Fig. 4.6 Initial and reloading flow curves for the torsion condition 500°C, 1.8 s^{-1} (100 Z_1). UL annealing with fractional softenings for various intervals. 117

Page

Fig. 4.7 Stress relaxation curves after a compression of 0.15. The reloading yield stress values after different relaxation times are shown on the curves (IA), (IB) and (IIA) as the tips of the vertical bars. 119

Fig. 4.8 Relationship between σ_m and σ_m / σ_{SRST}. 123

Fig. 4.9 Evolution of fractional relaxation (FR) under conditions IA,IB and IIA. Comparison with the fractional softening (FS) curves. 124

Fig. 4.10 Evolution of softening and recrystallized volume fractions with load-free and stress relaxation annealing times after compression to the same stress level ($Z_1 = 1.4X10^{13}\ s^{-1}$, $\sigma_m = 80.8$ MPa). 126

Fig. 4.11 Evolution of softening and recrystallized volume fractions with load-free and stress relaxation annealing times after compression ($\sigma_m = 100.5$ MPa) and torsion ($\sigma_m = 91.2$ MPa) at about the same stress level ($Z = 1.4X10^{15}\ s^{-1} = 100\ Z_1$). 127

Fig. 4.12 Evolution of softening with UL annealing time after torsion at the conditions: IV 1000 Z_1, σ_m = 100.5 MPa, for 450°C, 1.8 s^{-1} and III 100 Z_1, σ_m = 83.2 MPa, for 500°C, 1.8 s^{-1}. 129

Fig. 4.13 Softening (MECH) and recrystallization (MICR) kinetics according to Avrami relationship (eqn. (2.27)) under conditions IA UL and SR, and IB UL and SR (Z_1) (Table 4.4). 136

Fig. 4.14 Softening kinetics (MECH) according to Avrami relationship (eqn. (2.27)) under conditions IIA UL and SR, and IIB UL and SR; recrystalization kinetics (MICR) for IIA UL and SR (100 Z_1) (Table 4.4). 137

Fig. 4.15 Softening kinetics according to Avrami relationship (eqn. (2.27)) under conditions III (100 Z_1) and IV (1000 Z_1). 138

Page

Fig. 4.16 Conditions and times at which samples were selected for metallography. 143

Fig. 4.17 Fully recrystallized microstructure before testing. (300 μm) (75X) 144

Fig. 4.18 Microstructure from IA, 450°C, $1.8X10^{-3}$ s^{-1} (Z_1) and immediately quenched. (75X) 145

Fig. 4.19 Microstructure from IA stress relaxed for 5s. (75X) 145

Fig. 4.20 Microstructure from IA UL annealed for 20s. (75X) 146

Fig. 4.21 Microstructure from IA SR for 20s. (75X) 146

Fig. 4.22 Microstructure from IA SR for 80s. (75X) 147

Fig. 4.23 Microstructure from IA UL annealed for 100s. (75X) 147

Fig. 4.24 Microstructure from IA UL annealed for 400s. (75X) 149

Fig. 4.25 Microstructure from IB, 540°C, $9.3X10^{-2}$ s^{-1} (Z_1), immediately quenched. (75X) 149

Fig. 4.26 Microstructure from IB UL annealed for 5s. (75X) 150

Fig. 4.27 Microstructure from IIA 450°C, $1.8X10^{-1}$ s^{-1} (Z_1) as deformed. (75X) 150

Fig. 4.28 Microstructure from IIA, SR for 12s. (75X) 151

Fig. 4.29 Microstructure from IIA, UL annealed for 10s. (75X) 151

Fig. 4.30 Microstructure from IIA SR for 20s. (75X) 152

Fig. 4.31 Microstructure from IIA UL annealed for 20s. (75X) 152

Page

Fig. 4.32 Microstructure from IIA UL annealed for 50s. (75X) 153

Fig. 4.33 New grains around inclusions, IIA UL annealed for 20s. (250X) 153

Fig. 4.34 Fully recrystallized microstructure from IA; compression at 450°C, $1.8X10^{-3}$ s^{-1}, UL annealed for 1000s. (195 μm) (75X) 155

Fig. 4.35 Fully recrystallized microstructure from IA; SR for 400s. (194 μm) (75X) 155

Fig. 4.36 Fully recrystallized microstructure from IB; compression at 540°C, $9.3X10^{-2}$ s^{-1}, UL annealed for 40s. (170 μm) (75X) 156

Fig. 4.37 Fully recrystallized microstructure from IB; SR for 8s. (185 μm) (75X) 156

Fig. 4.38 Fully recrystallized microstructure IIA; compression at 450°C, $1.8X10^{-1}$ s^{-1}, UL annealed for 265s. (162 μm) (75X) 157

Fig. 4.39 Fully recrystallized microstructure IIA; SR for 100s. (157 μm) (75X) 157

Fig. 4.40 Fully recrystallized microstructure IIB; torsion at 450°C, $1.8X10^{-1}$ s^{-1}, UL annealed for 200s. (157 μm) (75X) 158

Fig. 4.41 Fully recrystallized microstructure IIB; SR for 100s. (169 μm) (75X) 158

Fig. 4.42 Fully recrystallized microstructure III; torsion at 500°C, 1.8 s^{-1} UL annealed for 30s. (76 μm) (75X) 159

Fig. 4.43 Fully recrystallized microstructure IV; torsion at 450°C, 1.8 s^{-1} UL annealed for 80s. (62 μm) (75X) 159

Fig. 4.44 Recovery kinetics under conditions IA UL and SR (Z_1), IB UL (Z_1) and IIA UL (100 Z_1). 162

Fig. 4.45 Conditions and times at which samples were selected for TEM. 163

Page

Fig. 4.46 Substructure from IA, 450°C $1.8X10^{-3}$ (Z_1) as deformed. 165

Fig. 4.47 Substructure from IA, UL annealed for 20s. 166

Fig. 4.48 Substructure from IA, UL annealed for 100s. 166

Fig. 4.49 Substructure from IA, SR for 5s. 167

Fig. 4.50 Substructure from IA, SR for 20s. 167

Fig. 4.51 Substructure from IIA, 450°C, $1.8X10^{-1}$ s^{-1} (100 Z_1) as deformed. 169

Fig. 4.52 Substructure from IIA, UL annealed for 10s. 170

Fig. 4.53 Substructure from IIA, UL annealed for 20s. 170

Fig. 4.54 Substructure from IIA, SR for 12s. 171

Fig. 4.55 Substructure from IIA, SR for 20s. 171

Fig. 5.1 Evolution of softening with load-free and stress relaxation annealing after compression to ε = 0.05 (Z_1, $\sigma_m \sim$ 60 MPa) (32). 190

Fig. 5.2 Stress relaxation curve after ε = 0.05 at 450°C, $1.8X10^{-3}$ s^{-1} (Z_1). Points 1 and 2 denote changes in the chart speed (32). 192

Fig. 5.3 Stress relaxation curve after ε = 0.05 at 500°C, $1.8X10^{-2}$ s^{-1} (Z_1) (32). 192

LIST OF TABLES

Table	Page
3.1 Strain-Annealing Treatments	69
3.2 Testing Conditions	75
4.1 Reloading and Relaxation Stresses	120
4.2 Stresses and Stress Ratios	121
4.3 Times and Time Ratios for Different Fractional Softenings (X)	131
4.4 Softening and Recrystallization Parameters	134
4.5 Volume Fraction Recrystallized Values and 95% Confidence Limits	140
4.6 Fully Recrystallized Grain Size	160
4.7 Recovery Kinetic Parameters	160
4.8 Misorientation between Cells	173
A-1. Reloading Stresses and Fractional Softenings for UL Annealing after Compression	207
A-2. Reloading Stresses and Fractional Softenings for UL Annealing after Torsion	208

LIST OF SYMBOLS

A, A', A'', A''', A_1	Experimental constants
D_o	Initial grain size
D_s	Steady state grain size
$\bar{D}$	Mean grain size
E	Young's modulus
G'	Rate of linear growth
$\bar{I}$	Mean intercept distance
K, K', K''	Specific reaction rates
L	Camera length
L'	Length of torsion sample
M	Average Taylor factor
M_T	Torque
N	Number of revolutions, torsion
$\dot{N}$	Revolutions per second
$\bar{N}$	Density of germ nuclei
$\bar{N}'$	Average of the intercept count
Q_{DRV}	Activation energy for dynamic recovery
Q_R	Activation energy for recrystallization
Q_i	Activation energy for the ith mechanism
Q_r	Activation energy for recovery
R	Universal gas constant
R'	Torsion sample radius

S	Entropy
S_o	Coefficient of intergranular strength
T	Absolute temperature
T_m	Absolute melting temperature
V	Crosshead velocity
V_o	Variance
X	Fractional softening (= FS)
X_R	Volume fraction recrystallized
X_r	Fractional softening due to recovery
X'_R	Fractional softening due to recrystallization
X_∞	Total fractional softening at an infinite time
$X_{r\infty}$	Fractional softening due to recovery at infinite time
$X'_{R\infty}$	Fractional softening due to SRX at infinite time
X_{SR}	Fractional relaxation (= FR)
Y	Fractional retained work hardening
Z	Zener-Hollomon parameter
Z_C	Critical value of Z for grain refinement
BCC	Body-centered cubic
C.L.	Confidence limits
C.V.	Coefficient of variation
DRV	Dynamic recovery
DRX	Dynamic recrystallization
ETP	Electrolytic tough pitch (copper)
FCC	Face-centered cubic
HSLA	High strength low alloy (steel)

MECH	Mechanical
MICR	Microscopic
OFHC	Oxygen-free high conductivity (copper)
SFE	Stacking fault energy
SR	Stress relaxation
SRV	Static recovery
SRX	Static recrystallization
TEM	Transmission electronmicroscopy
UL	Unloaded
b	Burger's vector
h	Instantaneous sample height
h_o	Initial sample height
k	Avrami time coefficient
k'	Boltzmann constant
m	Kinetic order
m'	Strain rate sensitivity
n	Sample size
n'	Strain hardening exponent
p	Avrami reaction order constant
s	Recovery rate ($= \nu$)
s_o	Apparent standard deviation
s'_o	Preliminary value of recovery rate
s_{xv}	Mean standard deviation
t	Time
t'_o	Preliminary value of recovery parameter

t_o''	Coefficient of intragranular strength
t_{SR}	Stress relaxation time
t_{UL}	Unloading annealing time
t_X	Time to reach fractional softening X
v	Activation volume
$\bar{v}$	Mean activation volume
x	Displacement of the intersection points
y	Hardness of the material
ζ	Structure term
Θ	Work-hardening rate
Θ'	Subgrain misorientation
ΔG	Activation-free energy for recovery
ΔN	Deviation from the average
$\Delta\sigma$	Stress drop
$\Delta\sigma_{rr}$	Stress drop due to recovery
$\Delta\sigma_{rR}$	Stress drop due to recrystallization
α	Proportionality factor
α', β	Experimental constants
ε	Normal true strain
ε_{CDRX}	Critical strain for DRX
ε_m	Strain at the end of deformation
ε_o	Instantaneous strain in creep
ε_p	Peak strain
ε_r	Rupture strain in creep
ε_{ex}	Instantaneous value of elastic strain
ε_{ox}	Initial elastic strain

ε_{px}	Instantaneous value of plastic strain
ε_1	Strain at the end of 1st stage of creep
ε_2	Strain at the end of 2nd stage of creep
$\dot{\varepsilon}$	True strain rate
$\dot{\varepsilon}_c$	True strain rate in compression
γ	Shear strain
μ	Shear modulus
σ	Normal true stress
σ_m	Flow stress at the end of first stage
σ_o, σ_y	Yield strength
σ_p	Peak stress
σ_r	Reloading yield stress
σ_r'	Flow stress at the end of first stage for metal which only softens by recovery
σ_{rr}	Reloading yield stress after recovery
σ_s	Steady state flow stress
σ_u	Athermal stress
σ^*	Thermal or effective stress
σ_{int}'	Preliminary value of intersection stress
σ_{int}	Intersection stress
σ_{mav}	Average flow stress at the end of deformation
σ_{SR}	Instantaneous relaxation stress
σ_{SRST}	Relaxation stress at saturation
τ	Applied shear stress
τ_i	Internal shear stress
τ_u	Athermal shear stress

τ^* Thermal or effective shear stress

τ_{CDRX} Critical resolved shear stress for dynamic recrystallization

CHAPTER 1

INTRODUCTION

Understanding the behaviour of materials under stress relaxation is important both from the industrial and scientific points of view. Processes, such as continuous annealing or certain rolling operations with tension between stands or coilers, result in materials being held at high temperature under the influence of stress. Inspiration for this research arose from some apparently contradictory literature reports which are explained below. It has been shown that gently stressing, or straining, a cold-worked metal increases the rate and amount of recovery. As a further effect, this usually retards or supresses recrystallization. On the other hand, annealing of copper after a low strain under stress relaxation decreased the rates of recovery and recrystallization and also the amount of recovery.

The primary objective of the project was to determine the effect of stress relaxation compared to stress-free annealing, on the recovery and recrystallization of worked copper while holding it at constant temperature after hot deformation. A second objective of this research was to determine the correspondence between the restoration

kinetics in compression and torsion and thereby increase the range of strain rates examined. A final aim was to develop a method of separating the components of softening due to recovery and recrystallization.

CHAPTER 2

DEFORMATION, RESTORATION AND RELAXATION PROCESSES AT HIGH TEMPERATURE

2.1 Background on Stress Relaxation

2.1.1 Definitions

The following terms are given brief, preliminary definitions to eliminate any confusion that might arise from differences in usage. In many cases, more thorough explanations are given later.

Plastic deformation is an essentially irreversible shape change which occurs almost exclusively by the generation and motion of dislocations, which are linear, geometric, elastic defects in crystals.

Strain hardening is the increase of strength with strain which arises from the auto-limitation that the dislocation network, densifying with rising strain, imposes on the motion of dislocations.

Dislocation substructure is the strengthening arrangement which dislocations adopt during deformation. In particular, during hot deformation, dislocations initially become entangled, and at higher plastic strains form the walls of subgrains, leaving the interiors comparatively

empty.

Elongated grains or crystals are those extended preferentially along some direction in conformity with the outward change in shape of the object.

Recovery includes all processes of rearrangement and annihilation of dislocations which reduce the strength and energy of the substructure without marked change of the grain shape or orientation.

Recrystallization is the formation of small, nearly dislocation-free crystals which grow into the surrounding deformed material to ultimately give rise to low strength, equiaxed grains.

Restoration is the passage from a strain hardened state to a lower strength, less dislocated one through recovery and/or recrystallization. Dynamic restoration takes place during deformation at high temperature, while static restoration does so after deformation or during annealing at such temperatures.

High temperatures lie in the range $T > 0.5T_m$, where T_m is the absolute melting temperature of the metal.

Steady state deformation is a straining regime in which stress, temperature and strain rate remain constant due to dynamic equilibrium between hardening and restoration processes. This is found in creep where stress is fixed,

or in hot working where strain rate is fixed.

Thermal activation (of plastic deformation) is the assistance that thermal energy gives to the applied stress in causing dislocations to overcome internal barriers to motion.

2.1.2 Stress Relaxation at Low and Medium Temperatures, Stable Microstructures

Although the stress relaxation phenomenon is known since the last century (1), it is only in the last quarter of the present century that extensive stress relaxation of metals and alloys has been carried out. Most of the relaxation studies have concentrated on situations where it was important to keep constant the structure of the metal, i.e. under testing conditions which implied small plastic deformations and negligible recovery. To this end, the stress technique consists of the elastic deformation of a sample followed by a constancy of dimensions. If the condition of fixed strain in one direction is expressed by the equation

$$\varepsilon_{ox} = \varepsilon_{ex} + \varepsilon_{px} = \text{constant} \qquad (2.1)$$

where ε_{ox} is the initial elastic strain, ε_{ex} and ε_{px} are the instantaneous values of elastic and plastic strains. To be more precise, the only plastic deformation of the material during relaxation is that related to the elastic strains in both the specimen and the loading machine or device which

result from the load (2). In some cases, recovery of substructures is prevented by testing at low temperatures.

Some phenomena studied by stress relaxation at low temperatures are: rate controlling mechanisms of plastic deformation (3-6), work-hardening mechanisms (7-10), dislocation dynamics (11, 12), plastic flow prior to yielding (13), internal stresses (9, 14) and thermal activation parameters in plastic deformation (4, 5, 15).

Stress relaxation research at intermediate temperatures was carried out by Bystrov and Shakhmaev (16) examining dislocation mobility, and at high temperatures by Gibbs (17) to identify the rate-controlling processes in secondary creep.

Fox (18, 19) and Fox and Fuchs (20) accomplished stress relaxation experiments in the range 0.22 - 0.37T_m on copper and copper alloys to simulate service conditions of pressure-type electrical connections and springs in electromechanical switching devices. The specimens relaxed after preloading to a stress level equal to 50 or 100% of the yield stress. The rate of stress relaxation is higher for cold deformed metals than for annealed ones, and for heavier degrees of deformation. The rate of relaxation increases with temperature and initial level of stress. In cold rolled materials, transverse samples relaxed more slowly than longitudinal ones.

Oding et al. (21) made an extensive review of stress relaxation at both room and medium temperatures reporting mainly the results obtained by Russian workers. The specimens, usually without substructure, were loaded to an initial stress of less than 80% of the yield strength at the testing temperature σ_Y^T. Oding and Tseitlin (22) considered that relaxation of non-predeformed specimens is the result of two groups of processes proceeding simultaneously. The first takes place at the grain boundaries of polycrystalline metals and the second within the grains. When the relaxation results are plotted with the stress on a log scale and the time on a linear scale, two well defined stages are identified. The first is characterized by a rapid fall in stress and the second by a much slower decrease, as seen in Figure 2.1. In this figure, two important parameters can be established to characterize the resistance of metals to relaxation: The coefficient of intergranular strength S_o and the coefficient of intragranular durability t''_o. In the first stage of relaxation due to intergranular processes, S_o is the stress reduction ratio $S_o = \sigma'_o/\sigma_o$ where σ_o is the initial stress and σ'_o the stress at the start of the second stage of relaxation as extrapolated to zero time. The reciprocal of the slope of the second stage line gives the value of t''_o ($t''_o = \cot \alpha = ac/ad$). A third parameter characterizing the stress relaxation resistance of a metal, known as the service life, is defined as the time required for the

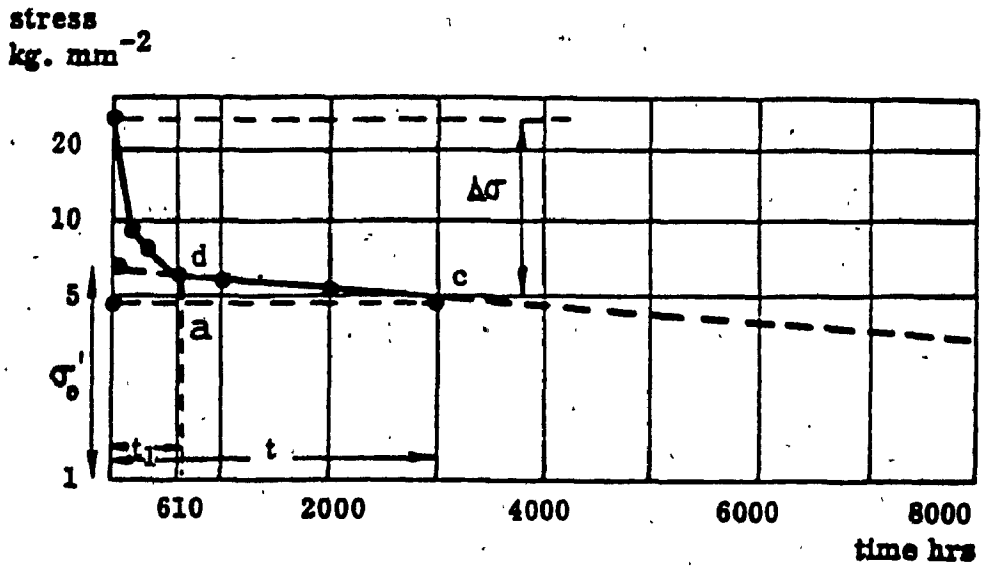

Fig. 2.1 Relaxation curve in semi-logarithmic coordinates. (after Oding and Tseitlin (22))

initial stress to fall to some specified value. Oding and Volosatova (23) studied the relaxation criteria in three austenitic stainless steels with different contents of Mo. In relaxation experiments at room temperature the second relaxation stage was eliminated, and the value of S_o increased with rise in Mo content.

The effect of prior relaxation tests on the relaxation rate was studied by Oding and Volosatova (24) in an investigation on annealed austenitic stainless steel and Armco iron at 575 - 625°C and 400 - 450°C, respectively. The experiments consisted of loading the samples to several values of pre-stress and measuring the fall in stress during relaxation. The sequence of loading and relaxing was repeated four times and the relaxation curves plotted. The stress falls very rapidly in the first relaxation stage of the first test whereas in the repeated relaxation tests this first stage fall in stress diminishes. For constant pre-stress, diminishment becomes successively less. The diminishment is enhanced if the pre-stress in the sequence of tests is successively reduced. The fall in stress during the first stage of relaxation is due to intergranular plastic flow. However, on repeated testing this diminishes as the grains become more "tightly wedged together." The principal effect of temperature increase in the relaxation tests was to decrease the value of S_o, i.e. to increase the initial stress drop. When experiments were carried out with

temperature cycling between two values, the relaxation curve was between the two isothermal relaxation curves. Determination of the temperature dependency of S_o for several FCC and BCC metals showed that its activation energy was about equal to that for boundary self-diffusion.

Experiments were carried out by Oding et al. (21) to clarify the diffusion mechanisms which operate during low and medium temperature stress relaxation and in load-free recovery after stress relaxation called by the authors relaxation recovery. They loaded three grades of austenitic stainless steels at 630°C in two successive tests at an initial stress of 176 MPa (18 kg/mm^2). During the first 150 h relaxation test, there was a large stress drop in the first stage. After relaxation for 150 h, a first group of samples was reloaded up to the same initial stress and relaxed for a further 150 h. The stress drop in the first stage was rather mild. A second group was unloaded and annealed for 150 h and then stress-relaxed for 150 h at the initial stress. The stress fall in the first stage was again pronounced.

The authors (21) explained that during stress relaxation the transfer of atoms into vacant sites in the crystal lattice occurs most rapidly in the direction of maximum shear stress. During the first stage of relaxation, this process occurs particularly rapidly at the grain boundaries, i.e. the areas with the maximum number of

vacancies and lattice disturbances. Thus, during stress relaxation the atoms diffuse into an ordered system according to the variation in the solution potential of the elastically strained crystal lattice. During load-free annealing after stress relaxation, on the other hand, the ordered system is restored to the disordered state by the random migration of atoms.

In tensile experiments on Ti at 27°C to a series of fixed stresses along the plastic flow curve (initial strains 0.02 to 0.12), Sargent et al. (25) observed the stress relaxation in repeated 5 minute intervals following re-straining to the original stress level. The decrease in stress drop in successive intervals is somewhat similar to Oding's results described above but does differ in that the reloading is right at the yield stress. The ratio of decrease in stress drop between one interval and the preceeding one to the strain increment needed to restore the stress level is defined as the strain hardening rate and is equal to the slope of the flow stress curve at the same stress level. The strain hardening decreases with strain.

2.1.3 High Temperature Relaxation

Wood and Suiter (26) by subjecting cold rolled Al to stress recovery caused 1 μm cells to grow to 50 μm at 250°C (ε=8%) and to 100 μm at 350°C (ε=14%), both substructures being resistant to recrystallization. Wilms in 1954 (27)

and later Auld et al. (28) annealed cold pre-strained (2.5-75%) specimens of Al 99.99% under low stress (1-4.8 MPa) creep conditions which are somewhat similar to those existing under high temperature (>0.6T_m) stress relaxation. The progress of restoration at 0.56 and 0.67T_m was followed by x-ray examination and metallographic monitoring. In samples pre-strained 5% at room temperature before creep testing, increases in stress progressively accelerated recovery and substructure growth. Recrystallization was observed at small values of creep stress (1.0 to 1.4 MPa), but it was retarded both in onset and rate of progress in comparison to stress-free annealing. Recrystallization was prevented altogether at a stress level of 1.7 MPa.

Thornton and Cahn (29) studied the kinetics of recovery and recrystallization of Al and of Cu (OFHC, 99.99% and 99.999%) in creep tests at high stress levels. The test temperatures varied from 0.53 to 0.64T_m for both materials. The pre-strains at room temperature were either 30 or 60% for Al and either 10 or 30% for Cu. Creep stresses in the range 5.9 to 30 MPa were applied to the aluminum samples and from 50 to 170 MPa to the copper ones. Hardness changes were used as the index of recovery and recrystallization. For both pre-strain levels, aluminum showed an increase in the rate and amount of recovery with creep stress. After 30% pre-strain, recrystallization was not observed in aluminum for the annealing times used, while after 60%

pre-strain it was considerably reduced or inhibited in comparison with the load-free annealed samples. OFHC copper underwent a small amount of recovery without recrystallization for all test conditions and likewise the 99.999% Cu at 10% pre-strain. After 30% pre-strain, recrystallization was accelerated in 99.999% copper, because the high creep stresses hardened the old grains additionally (and also the new recrystallized grains). Increased impurity content enhanced recovery over recrystallization.

Recently, Ucisik et al. (30) carried out multistage hot torsion tests on plain carbon and Nb-HSLA steels under isothermal or continuous cooling regimes. They deformed the samples 0.03, 0.06, or 0.12 at one of two strain rates 0.01 s^{-1} or 0.1 s^{-1} and relaxed, or load-free annealed them for 3, 5, 10 or 100s between deformation steps. The softening between passes was measured in terms of fractional softening, i.e. the reduction in flow stress during the unloading or relaxation interval relative to the amount of strain hardening since the yield stress of the initial fully-annealed steel. They found that the extent of fractional softening was somewhat lower under stress relaxation than for unloading arrests. This was because, according to the authors, relaxation diminishes the extent of isochronal softening by static recrystallization by prolonging the action of dynamic recovery. The multistage tests with relaxation during the arrests compared to

unloading resulted in less strain hardening and lower flow curves upon reloading because of the retained substructure as altered by relaxation. The degree of relaxation during an interruption, when compared at the same stress level, is greater for the carbon steel because it is not impeded by the presence of Nb as in the HSLA steel. The amount of softening increases with the stress for both steels even though the temperature is decreasing.

Wray (31) found in hot tensile experiments on austenitic iron that dynamic recrystallization can happen under stress relaxation conditions when the sample was previously strained close to the peak strain ε_p. The time which elapses between the beginning of relaxation and the onset of recrystallization, considered an incubation period, is longer for a lower average stress acting on the sample during that time.

This author (32) previously carried out experiments to determine the effect of stress relaxation on the kinetics of restoration of ETP copper. Samples were compressed to a strain of 0.05 at i) 450°C, 1.8×10^{-3} s^{-1} or ii) 500°C, 1.8×10^{-2} s^{-1} and then stress relaxed or annealed under load-free conditions at the deformation temperature. The progress of restoration was followed by reloading the samples after increasing delay times. The mechanical softening data were correlated with metallographic observations. Important conclusions of that work were that

a) recovery and recrystallization occur in sequence under both types of annealing, b) stress relaxation decreases the rate and amount of recovery, and c) relaxation decreases the rate of recrystallization.

This retardation of recovery at a stress near the flow stress contrasts with the previous enhancement of recovery by a creep stress considerably lower than the flow stress as reported by Wood and Suiter (26), Wilms (27), Auld et al. (28) and Thornton and Cahn (29). The retardation of static recrystallization agrees with the previous observations of Wood and Suiter (26), Wilms (27), Auld et al. (28) and Thornton and Cahn (29) under creep conditions and Ucisik et al. (30) under stress relaxation. However, the enhancement of recrystallization under high constant stresses by Thornton and Cahn (29) and by Wray (31) indicate a different effect. The present work was encouraged by the apparently inconsistent results reported above. The limited scope of the previous work by this author (32) was a further stimulus to extend the research to higher stresses, strains and strain rates, closer to those used in the industry. Although during most periods between stages of hot deformation the material is permitted to statically soften under stress-free conditions, there are a few situations where a stress is applied such as in a continuous annealing furnace, or in a continuous strip mill by a neighboring stand or by the coiler.

2.2 Hardening and Softening During High Temperature Deformation

The stress relaxation experiments in this work consisted of hot deforming the material to a given strain within the plastic range at a constant strain rate followed immediately by stress relaxation (at the deformation temperature). The samples were subjected to two common deformation modes, compression for low strain rates and torsion for high strain rates. Since the substructure developed during the initial strain has an important influence on the relaxation, the formation and characteristics of the dislocation structure are described.

2.2.1 Hardening and Softening

When a metal is sufficiently loaded at high temperature, plastic straining occurs (33), and dislocation generation and motion take place. The growing network of dislocations progressively limit the motion of the mobile dislocations causing a rise in stress (34). This increase of stress, called work or strain hardening, is gradually counteracted by intensifying softening mechanisms. The restoration processes occurring concurrently with deformation are dynamic recovery and dynamic recrystallization. Dynamic recovery refers to the rearrangement and annihilation of individual dislocations without a marked change in grain microstructure. In dynamic recrystallization, new crystal lattices and orientations are

produced due to the migration of grain boundaries with the simultaneous annihilation of lattice defects as recrystallization proceeds (34).

It is very well known that hardening, dynamic recovery and dynamic recrystallization occur during hot deformation and creep of metals and alloys. Less well known and accepted is that these phenomena take place during stress relaxation. The occurrence of hardening has been shown by Thornton and Cahn (29) and by Sargent et al. (25). Solomon et al. (35) working with polycrystals of Fe-3%Si and Mecking and Gottsteinn(36) with single crystals of Cu proved that dynamic recovery happens during stress relaxation. Wray (31) and Mecking (36) found that dynamic recrystallization takes place during relaxation of γ-Fe polycrystals and Cu single crystals, respectively, if the samples have been pre-strained near the peak stress before relaxation.

2.2.2 Hot Working

During hot working, some metals restore only by dynamic recovery, while others restore by dynamic recrystallization as well. There is a general agreement (36-40) that metals of high stacking fault energy (SFE) restore only by dynamic recovery; pure Al is the only FCC metal in this category. FCC metals of lower stacking fault energy, on the other hand, restore at low strains by dynamic

recovery and at high strains also by dynamic recrystallization. BCC metals generally dynamically recover, however, high purity α-Fe recrystallizes dynamically under certain conditions (41). Depending on the restoration mechanisms operating in a metal during high temperature deformation, the flow curve can adopt one of two shapes described below.

2.2.2.1 Dynamic Recovery Flow Curve

The flow curve for high SFE metals is shown in Figure 2.2 (42). As deformation proceeds the stress rises initially rather steeply but then at a slower rate, until finally at large strains, remains constant. Since the stress-strain curves consist of distinct regions where different microscopic processes are dominant (43), several authors have proposed to divide them in sections.

Lutón and Jonas (44) divide the flow curve on a phenomenological basis in three parts. The first part begins as soon as the material is loaded and extends to the vicinity of the yield stress, which is defined by a plastic strain offset of 0.1 or 0.2%. During this interval plastic microstrain occurs and the plastic strain rate goes from zero to about the strain rate of the test. The initial slopes of the curve vary from E/50 at high temperatures and low strain rates to E/5 at low temperatures and high strain rates (E, elastic modulus) (45). The second part starts at

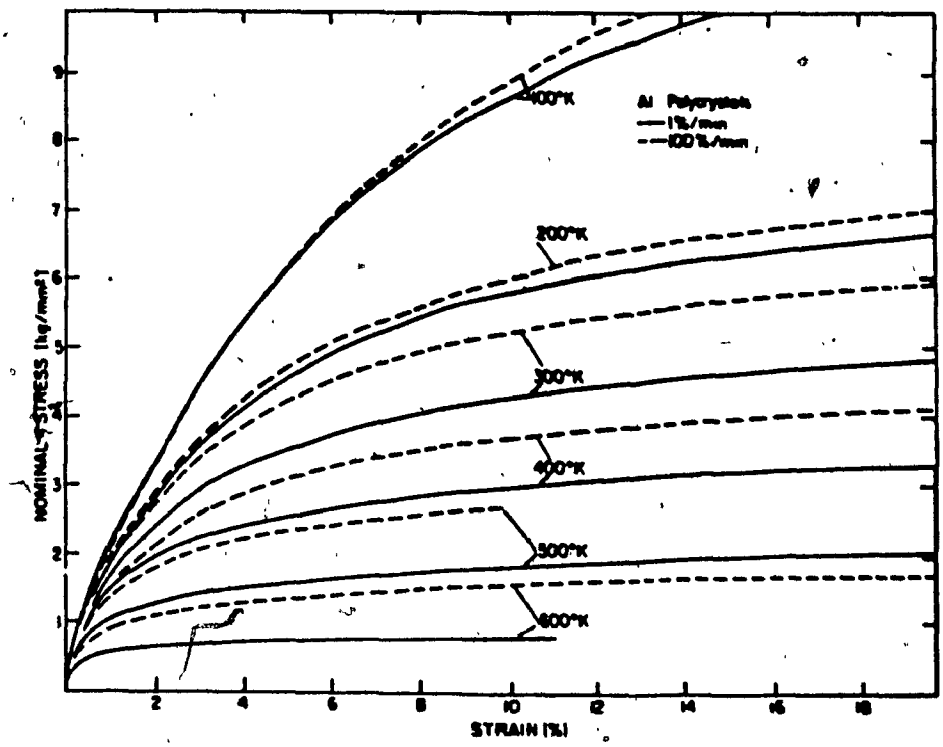

Fig. 2.2 Influence of strain rate and temperature on the shape of the flow curve of aluminum. Shape characteristic of DRV. Dotted line: $\dot{\varepsilon} = 1.7 \times 10^{-2}\ s^{-1}$. Continuous line: $\dot{\varepsilon} = 1.7 \times 10^{-4}\ s^{-1}$. (from Kocks et.al. (42))

the yield stress and goes up to the point where the hardening and softening processes counterbalance, which also indicates the beginning of the third part. The initial slopes of the flow curve in the second part go from E/800 at high temperatures and low strain rates to E/150 at low temperatures and high strain rates (45). During the third part, the temperature, strain rate and developed stress remain constant, a condition which also prevails during steady state creep.

Mecking (34) divides the flow curve on the basis of mechanism changes which occur during deformation. In polycrystals (where stage I is not found), stage II is the region of pure hardening where dislocation storage follows pure geometrical rules (34). This stage is independent of temperature and strain rate. Stage III is the region where simultaneous hardening and softening processes are occurring until the effectiveness of the latter rises to equal the former, and the net work-hardening rate ($\theta = d\sigma/d\varepsilon$) becomes zero. Stage II is defined (34) as the segment of a ($\theta - \sigma$) plot which commences on yielding and rises to a common plateau. The decrease of θ marks the start of stage III in which the rate of decline depends strongly on temperature and strain rate. Ultimately a saturation stress characteristic of the conditions is attained.

This kind of flow curve is observed in aluminum (38), some aluminum alloys (46), commercial purity ferritic

iron (47, 48), ferritic alloys (49, 50) and α-zirconium (51). Figure 2.2 shows that, as the temperature increases or the strain rate decreases, dynamic recovery becomes increasingly important and by contrast hardening declines in importance.

2.2.2.2 Flow Curves for Dynamic Recovery and Recrystallization

Examples of flow curves for metals undergoing dynamic recrystallization are shown in Figure 2.3, the shape depends on the metallurgical structure, temperature and strain rate. Upon loading, the stress rises continuously to a maximum at the peak strain ε_p. After a decline related to dynamic recrystallization, the flow curve follows an oscillating course to a plateau at either low strain rates or high temperatures, but declines directly to a constant plateau at either high strain rates or low temperatures.

Hardening and dynamic recovery are the only mechanisms taking place until near the maximum stress (34). Thus, the initial two divisions of the flow curve proposed by Luton and Jonas (44) can be applied; the first part being identified with microstrain and the second with hardening and dynamic recovery. However, a new third part begins with the nucleation of dynamic recrystallization which leads to the decline in the rate of hardening and which causes the peak, the fall after the peak and possibly an oscillating portion. In a fourth region, the steady stress σ_s is the

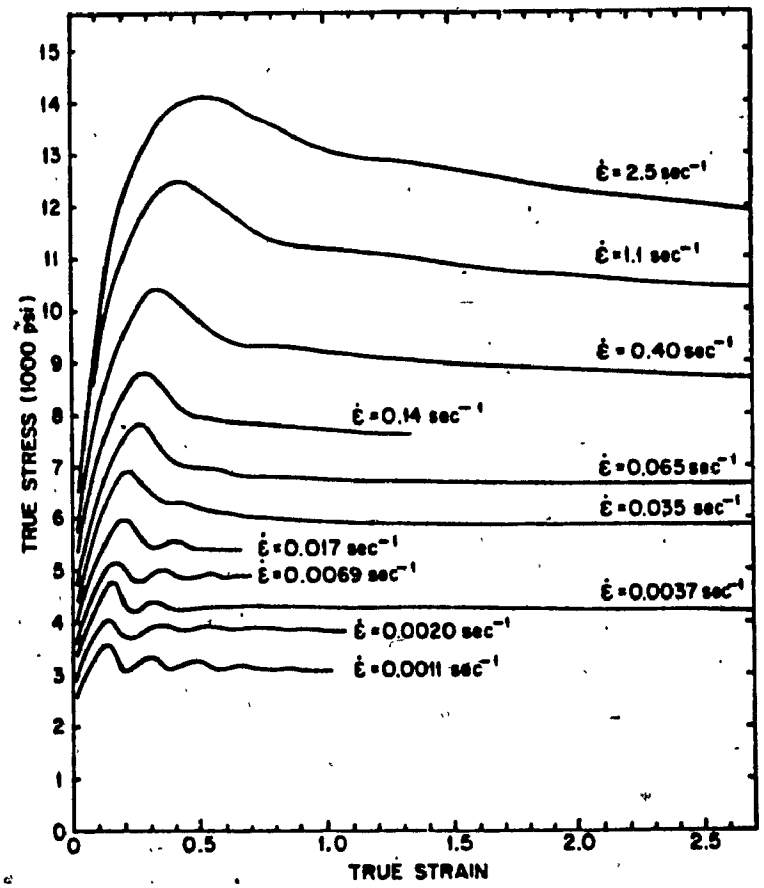

Fig. 2.3 Effect of strain rate on the flow curves of austenitic steel at 1100°C. Shape characteristic of DRX. (after Rossard and Blain (50))

result of equilibrium between hardening and recovery in the deforming recrystallized grains with additional softening due to formation of new recrystallized grains.

A critical strain ε_c is necessary to initiate dynamic recrystallization. Rossard (50) determined that ε_c is related to the peak strain, $\varepsilon_c = 0.85\varepsilon_p$. As the temperature increases, or the strain rate decreases (Figure 2.3), ε_c decreases. Thus, this restoration mechanism is favoured by high temperatures and low strain rates. The principal difference from the metals undergoing dynamic recovery is that the peak stress and the steady state stress are defined by the rate of recrystallization.

Some materials which display this type of flow curve are copper (38, 52), copper alloys (53), nickel (38), nickel alloys (52, 55, 56), high carbon steels (57), zone refined iron (58) and lead (59).

2.2.2.3 Creep Curves

Metals undergoing continuous deformation under constant load are said to creep. Under a wide range of conditions, the creep rate declines to a constant value as a result of attaining a balance between hardening and dynamic recovery. However, low SFE metals tested at high stresses and temperatures above $0.7T_m$ (60) exhibit an oscillating creep rate as a result of dynamic recrystallization. A creep curve of strain vs time for constant load in Figure

2.4a illustrates the stages observed in a metal which restores by dynamic recovery only. The strain ε_o is obtained immediately upon loading and is equivalent to the microstrain part of the flow curve. The first stage between ε_o and ε_1, which is characterized by a continuous decrease of the creep rate, is called primary or transient creep. This stage corresponds to the second part of the flow curve proposed by Luton and Jonas (61). The portion between ε_1 and ε_2 where the creep rate remains constant, called secondary or steady state creep, is identified with the third part of the flow curve where stress, strain rate and temperature stay constant. The stage betwen ε_2 and ε_r with creep rate increasing steadily is called tertiary creep. The equivalent section in the flow curve at constant strain rate is not usually clearly defined, although the fracture mechanisms are similar.

When dynamic recrystallization takes place, the creep curve exhibits alternating cycles of normal and accelerated creep. This is illustrated in Figure 2.4b. After a normal stage of primary creep the strain rate accelerates, indicating that dynamic recrystallization is occurring. At low stresses, there is insufficient build up in dislocation density to nucleate dynamic recrystallization, so that creep proceeds due only to dynamic recovery (60).

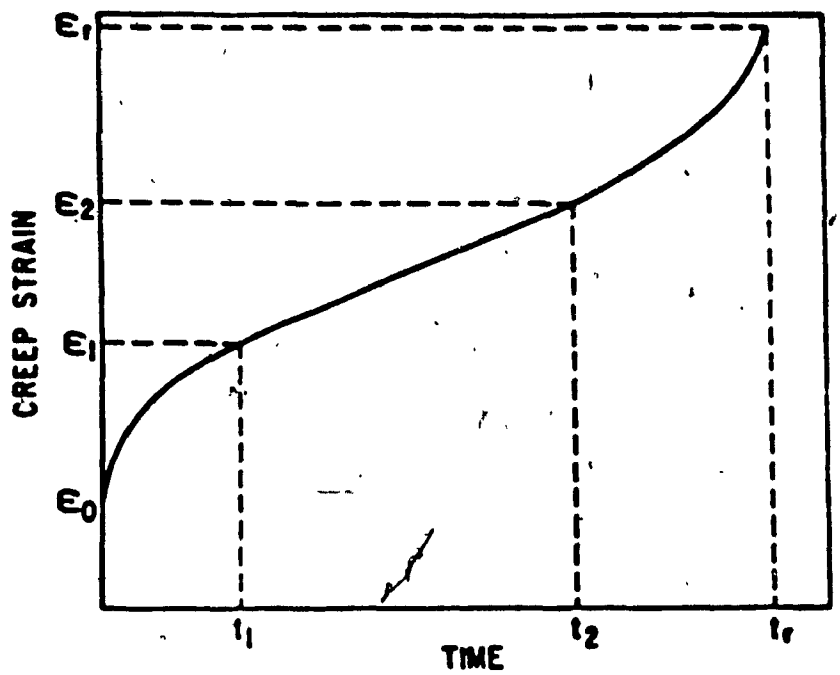

Fig. 2.4a Schematic representation of a creep-rupture curve. (Garofalo (40))

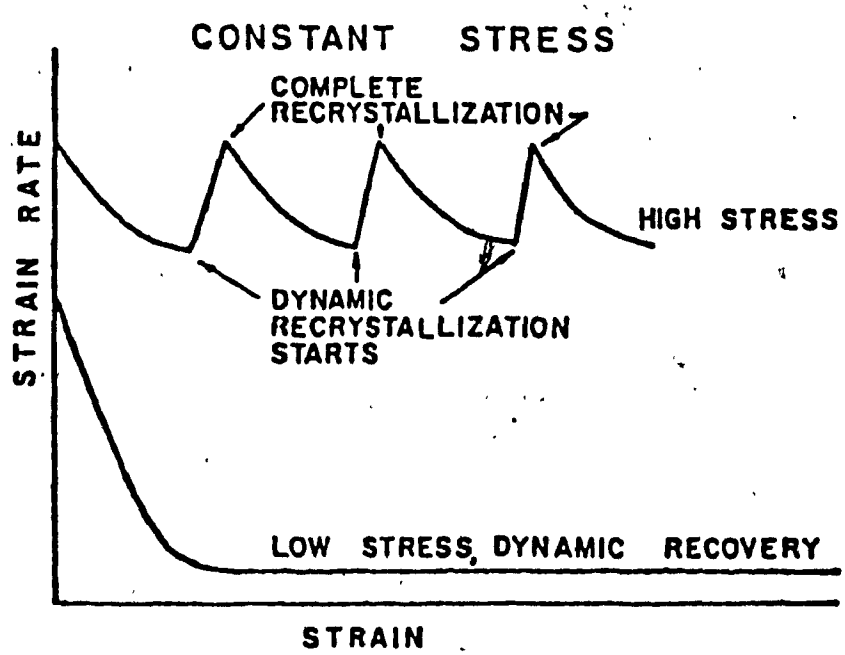

Fig. 2.4b Dynamic recrystallization during creep at high stress and temperature (upper curve) and dynamic recovery during creep at low stresses (lower curve). (McQueen and Jonas (37))

2.2.2.4 Stress Relaxation Phenomenon at High Temperature

Figure 2.1 shows a typical stress relaxation curve. It consists of two stages: The first is characterized by a rapid fall in stress, while the second by a slower fall. The stress asymptotically approaches either zero or some limiting value. The precise shape of the relaxation curve depends on the metallurgical structure, the level of pre-stress and the temperature.

Stress relaxation has been considered as a process of creep at a stress decreasing with time, in proportion to the increase in plastic strain, at the expense of the elastic strain (Eqn. 2.1) (21, 62, 63). However, there is no correspondence between the stages of the flow and creep curves with those of the stress relaxation one. Because of the small amount of plastic strain produced, multiple steps of stress relaxation are necessary to reproduce in the material a state of internal structure and stress similar to that generated by a creep or a constant strain rate test. It has been shown that creep curves (62, 64) can be plotted from a multi-step relaxation test. Because flow curves can be derived from creep curves (25, 34, 64), they can thus be obtained from stress relaxation data. Moreover, under suitable conditions of stress relaxation, there may occur the same mechanisms which take place in the course of the other deformation modes, namely, strain hardening, dynamic recovery and dynamic recrystallization.

2.2.2.5 Stress, Strain Rate and Temperature Relations

2.2.2.5.1 Empirical Relationships

It has been shown experimentally that deformation processes above $0.4T_m$ are thermally activated (65). Therefore, the strain rate is given by an Arrhenius-type of relation (40, 66, 67)

$$\dot{\varepsilon} = \Sigma\, A_i(\nu, S, T, \xi, \sigma_i(T,\xi)) \exp\,(-Q_i(T,\xi)/RT) \qquad (2.2)$$

where the function A_i includes the frequency of vibration ν, of the flow unit, the entropy S, the temperature T and the structure term ξ. σ_i is the stress function dependent on T and ξ, and Q_i, which may change with temperature and microstructure, is the activation energy for the ith mechanism controlling deformation.

Several mechanisms may be operating simultaneously. Fortunately, in most cases, one of the deformation mechanisms prevails relative to the others over a broad temperature range and the determination of Q_i is a simple task. If the different mechanisms operating depend on each other, the one that is slowest and requiring the largest activation energy will be controlling. If the mechanisms are independent of each other, the one that is fastest and requiring the lowest activation energy will control (40). When a single process is dominant and controls the flow, Equation 2.2 becomes

$$\dot{\varepsilon} = A(\sigma)\exp(-Q/RT) \tag{2.3}$$

A relationship which has been applied successfully to steady-state in both creep (68) and hot working (66) is

$$\dot{\varepsilon} = A'(\sinh \alpha'\sigma)^n \exp(-Q/RT) \tag{2.4}$$

where A' and α' are constant at constant temperature. For low values of stress, such that $\alpha'\sigma < 0.8$, Equation 2.4 becomes the power law which is very common in creep analysis

$$\dot{\varepsilon} = A''\sigma^n \exp(-Q/RT) \tag{2.5}$$

For high values of stress which lead to $\alpha'\sigma > 1.2$, Equation 2.4 turns into the exponential law

$$\dot{\varepsilon} = A'''\exp(\beta\sigma)\exp(-Q/RT) \tag{2.6}$$

One useful derivative of Equation 2.3 is the so-called Zener-Hollomon parameter (69)

$$Z = \dot{\varepsilon}\exp(+Q/RT) \tag{2.7}$$

In hot working of annealed samples of any stable metal similar flow curves are obtained for different conditions of temperature and strain rate when Z remains constant. It is equally true that the substructure and microstructure are also the same.

2.2.2.5.2 Flow Stress Relationships

The above similarity of structure and mechanical properties for different temperatures (at constant Z) can be employed in certain studies in which it is desired to study the effects of only one variable. Some examples are determination of strain-hardening exponents, of strain-rate sensitivities, of thermal activation energies, kinetics of recovery and recrystallization during stress relaxation or annealing after deformation. Mathematical relations which link the externally measurable parameters are known as mechanical equations of state. If such a constitutive relationship exists, the value of a variable, say stress, would be given uniquely for the instantaneous values of strain, strain rate, and temperature independent of the path, i.e. previous values of those variables. The Zener-Hollomon (69) relationship was suggested by Hollomon (70) to be such an equation. Further experiments showed that it did not apply to all the materials or test conditions (71).

Hart (72) suggested an alternative equation. He defined the dislocation structure generated during plastic deformation of a metal as its "hardness state". According to this approach, two specimens of a material are in the same mechanical state if they display the same hardness y when they are deformed at constant temperature. Thus there exists a state equation

$$\sigma = \sigma(y,\dot{\varepsilon}) \tag{2.8}$$

where σ is the applied (or developed) stress and $\dot{\varepsilon}$ is the developed (or applied) strain rate. The theory applies only to a restricted class of materials, namely, single and polycrystal specimens of relatively pure FCC metals which are metallurgically stable under the test conditions (73, 74). Despite the efforts expended to date, an acceptable and simple relationship among the mechanical variables has not yet been found.

2.2.2.6 Flow Stresses at High Temperatures

During plastic deformation the applied stress τ is opposed by internal stresses τ_i of two categories: i) athermal stress τ_u, derived from long-range obstacles which are too high and too long to be overcome by thermal activation; ii) the thermal or effective stress τ^*, resulting from short-range obstacles which can be surmounted with thermal assistance. The level of τ_u is determined by the dislocation structure of the material, incoherent particles, etc. On the other hand, τ^* is given by the Peierls-Nabarro force, fields of coherent precipitates and solute atoms among others (2, 75, 76).

The total internal stress is the sum of its components

$$\tau_i = \tau^* + \tau_u \tag{2.9}$$

therefore the applied stress is equivalent to

$$\tau = \tau^* + \tau_u \tag{2.10a}$$

so plastic deformation occurs by the concurrence of the applied stress and thermal activation.

For polycrystals Luton and Jonas (44) postulated the relationship

$$\sigma = \sigma^* + \sigma_u \tag{2.10b}$$

where the normal stresses are related to the shear stresses by the expression

$$\sigma = M\tau \tag{2.11}$$

where M is the average Taylor factor (77, 78).

2.2.2.7 Yield and Steady-State Stresses at High Temperatures

The athermal stress is related to the dislocation density (ρ) by the classical equation

$$\sigma_u = \alpha\mu b(\rho)^{\frac{1}{2}} \tag{2.12}$$

where α is a proportionality factor, the shear modulus and b the Burgers vector (79).

The dislocation density at yielding is roughly three orders of magnitude below that during steady-state flow. Thus the athermal stress at yielding is negligible when

compared with that under steady-state flow and Eqn. (2.10b) becomes (37)

$$\sigma_y = \sigma^* \tag{2.13}$$

where σ_y is the yield stress.

Luton and Jonas (80) in α-Zr and Petkovic (81) in FCC materials reported that the yield stress (and therefore σ^*) is strongly dependent on temperature and strain rate. The first authors also found a similar dependence for the steady-state flow stress σ_s.

From the similarity in temperature and strain rate dependences of σ_y and σ_s in many materials, for example α-Zr and a series of Zr-Sn alloys (80), the glide processes associated with σ_y and the recovery ones related to σ_s are thought to involve the same controlling mechanisms (37). It was hypothesized that unpinning of dislocation nodes or the break-up of attractive junctions may be such mechanisms (82).

2.3 Restoration After High Temperature Deformation

2.3.1 Microstructure After Deformation

Single crystals (oriented for multiple glide) (84-91) and polycrystals of moderate and high SFE (39, 92-94) distort during deformation into regions of uniform orientation (cells) bounded by walls of dislocations. The

cells are relatively free from dislocations but are separated by walls of high dislocation density (95). A small cell size is associated with more ragged cell walls (95). Frequently the cells are equiaxed, but in certain conditions are narrow and elongated and lie parallel to low index planes (39, 85). The size and perfection of cells decrease as the SFE of the metal is lower (39, 87). With increasing strain the cell wall misorientation increases and the cell size decreases, both parameters approaching constant values (39, 92, 96). The minimum cell size depends on the deformation mode, e.g. for Al this value is larger in tension (39, 97) than in rolling (39, 98).

As the deformation temperature increases and/or the strain rate decreases, the cell size increases and the cell walls sharpen as the constituting dislocations become more orderly arranged (99, 102). Such changes transform cells into subgrains at high temperatures and low strain rates as dynamic recovery takes place. At large strains (and therefore large internal stresses) new dislocation rearrangements may take place leading to cell growth through cell wall loss (103).

Single and polycrystal metals deformed in rolling or compression may form microbands. These are arrangements of parallel narrow cells elongated in the direction of rolling or perpendicular to the compression axis as applicable. The microbands separate wider deformation bands called matrix

bands. The misorientation from a matrix band to a neighbouring one may range from 30 to 50 degrees (104-106).

2.3.2 Static Recovery

In many industrial hot working operations deformation is carried out in several steps. Between these, the material continues to be exposed to high temperatures so that it softens. The restoration mechanisms of recovery and recrystallization are called static when they take place in the absence of strain, otherwise they are called dynamic. From the observations of many workers, McQueen and Jonas (37) concluded that two kinds of structural changes take place during recovery. The annihilation and rearrangement of dislocations in the cells and cell walls turn them into sub-boundaries in a process of polygonization. At longer times subgrain coarsening or coalescence through wall disintegration takes place.

Hasegawa and Kocks (84) found that the structural changes described above correspond to well defined patterns in the evolution of the strain hardening rate θ. Compared to the basic θ-σ curve of as-recrystallized material, recovered specimens show higher θ and lower σ on reloading. If only Type I polygonization has occurred the curve decreases rapidly to coincide with the unrecovered one. When Type II coalescence has occurred the θ-σ plot falls below the original curve and only rejoins it after high

strains.

Hasegawa et.al. (107) reported that the backward (opposite to applied) internal stresses produce reverse flow of dislocations in the interior of the cells during the early part of annealing. Forward internal stresses cause forward flow with narrowing of, and dislocation ordering within the cell walls or sub-boundaries at later stages of annealing. In addition a small backward external stress slows down recovery whereas a forward one promotes it, causing more rapid ordering of the sub-boundaries.

Metals of high SFE, such as Al single crystals oriented for multiple glide, undergo both Type I recovery (at low temperatures and/or short annealing time) and Type II recovery (at high temperatures and/or long annealing times) (84). Metals of low SFE undergo Type I recovery only; this is the case for multiple glide monocrystals of Cu and Ni (85). Although Type II recovery has been clearly observed only in a high SFE metal such as Al, Cook et.al. (85) pointed out that subgrain coarsening occurs in low SFE metals but is unstable. Hu (105) working with silicon-iron (001)[110] and (001)[100] single crystals observed that, after annealing in the temperature range $0.24-0.34T_m$, there is a general reduction in dislocation density. When annealing was carried out at $0.44T_m$ cells transformed into subgrains (Type I). Subgrain growth corresponding to Type II took place only at $0.54T_m$.

The rate of recovery (under fixed annealing conditions) is increased by whatever has raised the internal stress, that is, by decrease in deformation temperature and increase in strain rate and strain. However, in hot working the last is effective only until steady-state flow is attained (37). The rate of recovery also increases with the temperature of annealing or holding. The addition of solutes in general tends to decrease the rate of static recovery (108). It has been suggested by several authors (57, 108) that this is due to a decrease in the stacking fault energy. Second phase particles may reduce the rate of recovery depending on their strength, spacing and size (109-113).

2.3.2.1 Static Recovery Mechanisms

Recovery arises from the reaction between dislocations which have moved to meet each other. An individual dislocation is activated to overcome short range barriers by heat and stress arising from the long range stress fields of the other dislocations possibly aided by an external source. It has been suggested that the thermally activated mechanisms important at high temperatures are climb, cross-slip and the unpinning of attractive junctions (37, 85, 114).

For the subgrain growth stage of recovery Hu (105) proposed the mechanism of subgrain coalescence. It is

explained as the gradual unraveling of the common boundary by the moving away of dislocations into the adjacent sub-boundaries around the subgrains.

2.3.2.2 Static Recovery Kinetics

The several kinetic laws which have been found to govern recovery will be discussed in turn. If one assumes that static recovery follows m^{th} order kinetics, it proceeds according to

$$dY/dt = - K\ Y^m \tag{2.14}$$

where Y is a property which changes with the progress of recovery, and K, known as the specific reaction rate constant (115), is a temperature dependent rate constant given by

$$K = K' \exp\ (-Q_R/RT) \tag{2.15}$$

where Q_R is an activation energy and K' is a further constant. According to the present method, the parameters used to describe the recovery kinetics of a deformed material are the following: i) the flow stress of the fully annealed material (σ_o); ii) the flow stress of the strain-hardened material at a predetermined constant strain (σ_m); and iii) the initial flow stress after a recovery anneal (σ_r). These three parameters define the fractional softening X, according to the relation (116)

$$X = (\sigma_m - \sigma_r)/(\sigma_m - \sigma_o) \tag{2.16}$$

as well as the fractional retained work hardening

$$1 - X = (\sigma_r - \sigma_o)/(\sigma_m - \sigma_o) = Y \tag{2.17}$$

Rearranging Eqn. (2.14)

$$Y^{-m}\, dY = -K\, dt$$

The integration limits arise from the conditions: for $t=0$, $\sigma_r=\sigma_m$ and from Eqn. (2.17) $Y= 1$; and for $t=t$, $\sigma_r=\sigma_r$ and $Y=Y$. Integration leads to

$$Y^{(1-m)} = 1 + K(m-1)t \tag{2.18}$$

Li (117) found that recovery of LiF crystals obey a second order kinetics, i.e. $m = 2$. Betteridge (118) and Perryman (119) observed that recovery of Al at high temperature follows a third order kinetics.

If recovery obeys first order kinetics, the integration of Eqn. (2.14) leads instead to

$$\ln Y = -Kt \tag{2.19}$$

Eqn. (2.19) can also be expressed in terms of X by substituting Y by (1 - X), thus,

$$X = 1 - \exp(-Kt) \tag{2.20}$$

Luton et.al. (120) found that in ETP copper recovery after

hot working approximately follows linear kinetics (m=1.33).

In a third alternative, the rate of recovery obeys an exponential law. For simplicity $(\sigma_r - \sigma_o)$ instead of Y will be considered the property which changes with recovery, so

$$d(\sigma_r-\sigma_o)/dt=-K''\exp[(-\Delta G_o - \int(\sigma_r-\sigma_o)dv)(1/k'T)] \qquad (2.21)$$

where ΔG_o is the activation free energy for recovery, v is the activation volume, K'' is a proportionality constant incorporating the dislocation density, the attempt frequency, and a geometric factor, and k' is the Boltzmann constant. Assuming that the stress dependency on the activation volume is negligible, Eqn. (2.21) becomes

$$d(\sigma_r-\sigma_o)/dt=-K''\exp(-\Delta G_o/k'T)\ \exp((\sigma_r-\sigma_o)\ \bar{v}(1/k'T)) \qquad (2.22)$$

Relation (2.22) can be inverted to give

$$\exp(k'T/\ \bar{v}d(\sigma_r-\sigma_o)/\exp(\sigma_r-\ \sigma_o) = -K'''dt \qquad (2.23)$$

where $K''' = K''\exp(-\Delta G_o/k'T)$. On integration, taking into account that $\sigma_r = \sigma_m$ at t=0, the latter leads to

$$\sigma_r = \sigma_m - s \log\ (1+t/t_o) \qquad (2.24)$$

where $t_o = k'T/\ \bar{v}K'''\exp(-(\sigma_m-\sigma_o)\ \bar{v}/k'T)$ and $s = k'T/2.303\ \bar{v}$. An alternative equation to (2.24) is obtained in terms of Y, the fractional retained work hardening defined by Eqn. (2.17)

$$Y = 1 - (s \log(1+t/t_o))/(\sigma_m - \sigma_o)$$

or

$$Y = 1 - \nu \log (1 + t/t_o) \qquad (2.24a)$$

with $\nu = s/(\sigma_m - \sigma_o)$.

Equations similar to (2.24) have been proposed by several workers in the literature for the description of static recovery. For example, in 1949 Kuhlman et.al. (121) reported that their results were well represented by such an expression. The relation (2.24) has been applied to static recovery (116, 121, 122, 123) and to stress relaxation at low temperatures as well (124). Kocks and Mecking (123) showed that Eqn. (2.24) applies to static recovery at low and medium temperatures.

The activation energy for recovery can be determined from the well known expression

$$1/t = K \exp(-Q_r/RT) \qquad (2.25)$$

Q_r, the activation energy for recovery is determined from the slope of a ln(t) against (1/T) curve.

2.3.3 Static Recrystallization

Static recrystallization involves the growth of small, nearly dislocation free crystals from hot (or cold) worked metal, thereby consuming the deformed structure,

replacing it with low strength equiaxed grains (125).

The deformation conditions influence the recrystallization rate. Petkovic et.al. (57) observed that, in carbon steels, the rate of recrystallization increased as the prior strain rate and strain increased. Rise in the temperature of deformation decreases the rate of static recrystallization (57, 126) and raises the incubation time for recrystallization (57). Once the high temperature pre-strain exceeds the critical strain for static recrystallization, the recrystallized grain size decreases with further strain as it does for cold work (127) but only up to the attainment of steady state deformation.

The chemical composition affects the recrystallization kinetics. Elements in solution usually retard the rate of recrystallization, for example Fe in Ni (60) and Nb in low carbon steels (57). Second phase particles may have opposite effects on the rate of recrystallization according to their dispersion parameters - particle shape, size, spacing (128) - and their strength as well (129). When larger than 0.6 μm, second phase particles enhance nucleation and thus accelerate recrystallization as a result of locally increasing the dislocation density produced by deformation (129, 93, 130, 131). If the particles are smaller than 0.6 μm, they may produce a dragging force on the moving grain boundaries and thus slow down recrystallization (129, 132).

2.3.3.1 Static Recrystallization Mechanisms

Recrystallization is a process which usually takes place in two stages, nucleation and growth. The nuclei are regions of nearly perfect crystals capable of continued growth into the surrounding deformed matrix. Several mechanisms have been proposed for the nucleation process, the most important of which are grain boundary bulging, subgrain coalescence and high angle boundary formation from high density cell walls.

The grain boundary bulging mechanism applies to polycrystalline metals of both high (58, 133) and low (134) SFE after low or moderate deformation. During the process, segments of an existing high angle boundary bulge out and act as nuclei which are free to grow.

The coalescence mechanism described in Section 2.3.2.1 may lead to the formation of a nucleus with high angle boundaries. Once the nucleus is larger than a critical size it grows by migration of the boundaries into the polygonized matrix (105). This mechanism is observed in high SFE metals after large strains (37).

In low SFE metals after large deformations, cell walls may reach such large misorientations that they are capable of migrating directly upon annealing.

2.3.3.2 Static Recrystallization Kinetics

Johnson and Mehl (136) and Avrami (137, 138) developed separate kinetic laws to describe metallurgical reactions which proceed by nucleation and growth. These include processes such as solidification and eutectic reactions, as well as recrystallization processes. Avrami's theory can be considered the general kinetic law from which the Johnson and Mehl laws are derived as special cases.

2.3.3.2.1 Johnson and Mehl Theory

Johnson and Mehl (136) define general nucleation as a process that occurs uniformly and at random. For such a type of nucleation the authors make the following assumptions: a) the rates of nucleation and growth remain constant throughout the reaction, b) the cold worked matrix is composed of spherical grains, and c) the rate of growth is retarded by the impingement of growing nodules on one another. Under these restrictions the equation which governs recrystallization is

$$F(t) = 1 - \exp(-\pi/3 N (G')^3 t^4) \qquad (2.26)$$

where F(t) is the fraction recrystallized at the time t, N is the rate of nucleation and G' is the rate of linear growth. These authors suggested that Eqn. (2.26) applies to the recrystallization of heavily deformed metals, where the potential nucleation sites are distributed uniformly

within the matrix.

2.3.3.2.2 Avrami's Theory

For the derivation of Avrami's equation, it is assumed that a) $\bar{N}$ is the density of germ nuclei before the grains of the new phase start to grow; it is a function of time and temperature, and b) the rate of linear growth G' is considered constant for macroscopic crystals but is a variable for extremely small crystals. The Avrami equation adapted to recrystallization is

$$X_R = 1 - \exp(-kt^p) \qquad (2.27)$$

where X_R is the volume fraction recrystallized; p is an exponent which depends on the geometrical shape of the new grains (lineal, plate-like or polyhedral), $\bar{N}$ and G', it defines the flatness of the curve; k is a parameter which depends on $\bar{N}$, G' and a shape factor.

The Mehl-Avrami law has been applied successfully to recrystallization of both cold-worked (139) and hot-worked (58, 120) materials. However, it has been shown that when recovery and recrystallization occur simultaneously the slope of the log (ln(1/1-x)) vs log t curve slightly decreases. Vandermeer and Gordon (139) confirmed this in Al-0.0086%Cu where the driving force for recrystallization decreases continuously and so also the rate.

The activation energy for recrystallization (Q_R) is calculated by substituting in Eqn. (2.25) the time to obtain a given value of X_R, say 0.5. The slope of a ln(t) vs 1/T curve yields Q_R.

2.4 Restoration During Hot Working

2.4.1 Dynamic Recovery

The characteristics and evolution with temperature and strain rate of the hot worked structure were described in Section 2.3.1. The effect of alloying elements on the dynamic recovery rate is similar to that described for the static process in Section 2.3.2 (37).

2.4.1.1 Dynamic Recovery Mechanisms

From deformation activation energy values, Jonas et.al. (142) concluded that the controlling mechanisms for dynamic recovery are very likely the climb of edge dislocations and the cross-slip of jogged screw dislocations. McQueen and Jonas (37) included node unpinning as an alternate mechanism. McQueen and Conrod (110) recently presented an explanation for the presence of equiaxed subgrains during steady state deformation: Dislocations are generated by the bowing out of segments from the sub-boundaries and from the network within the subgrains. These segments migrate until they accomodate near a sub-boundary and remain there until they are able to

knit into it (143). Recovery occurs by annihilation of dislocations of opposite sign which have knit themselves into the sub-boundary from opposite sides and by unravelling of the sub-boundary as dislocations are pushed out of it. Hardening arises from new dislocations knitting themselves into sub-boundaries. Thus, the continuous unravelling and knitting of subgrain boundaries at an equilibrium spacing defined by the internal stress fields produce "repolygonization" of equiaxed subgrains (37).

It has been recognized that a narrow band along a cell wall or sub-boundary is characterized by a high dislocation density (hard region) where there are large internal stresses in the forward direction (same as the applied stress), whereas in the cell interior there is a low dislocation density (soft region) and a small internal stress in the backward direction (107, 150). Recent measurements of forward and backward stresses by transient creep tests yielded values of $5\sigma_s$ and $0.5\sigma_s$ (σ_s is the steady state stress), respectively (151-153). The high ratio between these stresses favors the bowing out of segments in the sub-boundaries over those in the subgrain interior as described in the McQueen and Conrod explanation (110).

2.4.1.2 Dynamic Recovery Kinetics

Kocks and Mecking (123) have shown that equation (2.24) applies to dynamic recovery which takes place during stress relaxation at low and intermediate temperatures. The parameters s and t_o depend on the stress relaxation temperature and t_o also depends on the stress σ_m after deformation but before stress relaxation.

The activation energy for dynamic recovery (Q_{DRV}) can be estimated by applying equations (2.4, 2.5, 2.6) to the results of hot working experiments at a fixed value of steady state stress.

2.4.2 Dynamic Recrystallization

It has been established that the onset of dynamic recrystallization (DRX) in single crystals is governed by a critical value of the resolved shear stress τ_{CDRX} (140), whereas in polycrystals it is by the attainment of a critical strain ε_{CDRX} (55). Moreover, the peak stress σ_p decreases as the initial grain size D_o increases when the latter is larger than 100 μm but is independent in the case of finer grains (144, 145). By contrast, ε_p increases with grain size up to about 100 μm and subsequently only a small dependence is observed (145). Both σ_p and ε_p rise with decrease in temperature and increase in strain rate and Z (55). Throughout the steady state regime, the grain size remains constant and is inversely related to both Z and the

steady state stress σ_s (102).

Jonas and Sakai (144) reported that a single peak flow curve is associated with grain refinement, while a multiple peak flow curve is coupled with grain coarsening. When a material is tested under conditions of Z higher than a critical value Z_c which increases as the initial grain becomes larger, grain refinement arises, otherwise coarsening takes place. They determined that the conditions $D_o > 2D_s$ or $D_o < 2D_s$ lead to single peak or multiple peak behaviors, respectively. The model described above has been supported by results of other workers (56, 102, 146, 147).

The effect of solute additions is not simple. It has been found that elements in solution retard both the onset and subsequent progress of DRX (148). Augmentation of Cr and Ni in austenitic stainless steels greatly increase ε_p (112). By contrast, it has been reported that dynamic recrystallization may be induced in Al alloys by reducing the SFE with Zn additions (149).

Dispersed second phase particles may also have opposing effects. It has been pointed out that carbonitride precipitation retarded DRX in HSLA steels (148, 154). There has been observed dynamic recrystallization in an Al-5Mg-0.8Mn even though 0.2 μm $MnAl_6$ stabilized the substructure in the alloy. Nucleation of the dynamic recrystallized grains was apparently enhanced by large (>0.6

μm) (Fe, Mn)Al_6 particles (155,156).

2.4.2.1 Dynamic Recrystallization Mechanisms

The dynamic recrystallization mechanisms for nucleation are the same as for static recrystallization, namely, grain boundary bulging, subgrain coalescence and high angle boundary creation by deformation. Grain boundary bulging is the mechanism which has been observed more frequently especially at low and moderate strains and strain rates (55, 56, 102).

It has been proposed that DRX in single crystals is nucleated by migration of a boundary generated either by coalescence of subgrains or by aggregation of dislocations into a high angle boundary (85, 140). The latter mechanism was observed in the initiation of DRX in polycrystalline Cu heavily deformed in torsion at high strain rates (102). Nucleation at deformation bands was observed in Cu of large grain size (>100 μm) by Blaz et.al. (145) after moderate compression at low and medium strain rates. Nucleation at deformation bands may be related to the subgrain coalescence mechanism (105).

2.4.2.2 Dynamic Recrystallization Kinetics

Luton and Sellars (55) suggested that DRX obeys the same kinetic law as static recrystallization, ie. The Mehl-Avrami law, Eqn. (2.27)

$$X = 1 - \exp(-kt^p)$$

where the symbols have the same meanings as before. ε_p and ε_s define the strains (and therefore the times) at which recrystallization starts ($X = 0$ and $t = 0$) and finishes ($X \sim 0.98$), respectively. X may be calculated at any intermediate strain (time) between ε_p and ε_s. When DRX is periodic, the plotting of the X vs $\varepsilon(t)$ curve is straightforward. When DRX is continuous the curve has to be corrected to take into account the balance between the rates of work hardening and recrystallization.

The activation energy for dynamic recrystallization (Q_{DRX}) is calculated by the same procedure followed for dynamic recovery. It is usually different from the values for SRX since it shows the temperature dependence of deformation in combination with that for boundary migration.

2.4.3 Metadynamic Recrystallization

Glover and Sellars (58) and McQueen and Bergerson (102) observed that recrystallization after deformation in which there had been dynamic recrystallization was remarkably rapid, they proposed that it occurred by continued growth of nuclei formed dynamically. Such continued migration of high angle boundaries required no incubation period and produced regions completely free of substructure (since they were not further deformed as during true dynamic recrystallization). Because no new dynamic

nuclei were formed after deformation ceased, the grain size is larger than the dynamic size. In so far as the continued growth does not consume all the deformed regions classical static recrystallization may take place. Subsequently, Petkovic et.al. (54) examined this mechanism in greater detail and coined the name "metadynamic", i.e. post-dynamic recrystallization.

It has been observed in zone refined iron that metadynamic recrystallization obeys the Mehl-Avrami equation, however, the time exponent is smaller (~ 1) than that for static recrystallization of the same material tested under the same conditions to a strain less than the peak strain (58).

CHAPTER THREE

EXPERIMENTAL EQUIPMENT, MATERIALS, AND METHODS WITH PROCEDURES FOR ANALYSIS OF DATA

3.1 Experimental Equipment

3.1.1 Compression Testing

3.1.1.1 Testing Assembly

The tests were carried out on a 10 000 kg Instron testing frame, Model TT-D, modified for constant true strain rate compression. The crossheads speeds available in this machine lie between 50 and .005 cm/min. The loads were measured by a 25 kN load cell. The crosshead displacements were measured by a Hewlett-Packard Model DCDT-500 displacement transducer. The compression train consists of two loading members, the upper ram and lower anvil, and their supports (Fig. 3.1). The anvil is designed to allow samples to be quenched in 1 to 5 seconds after the completion of the test. The loading members are enclosed in an Inconel chamber which permits experiments to be carried out in a controlled atmosphere. The required high temperatures were supplied by a SATEC three-zone platinum split furnace controlled by a current proportioning Leeds

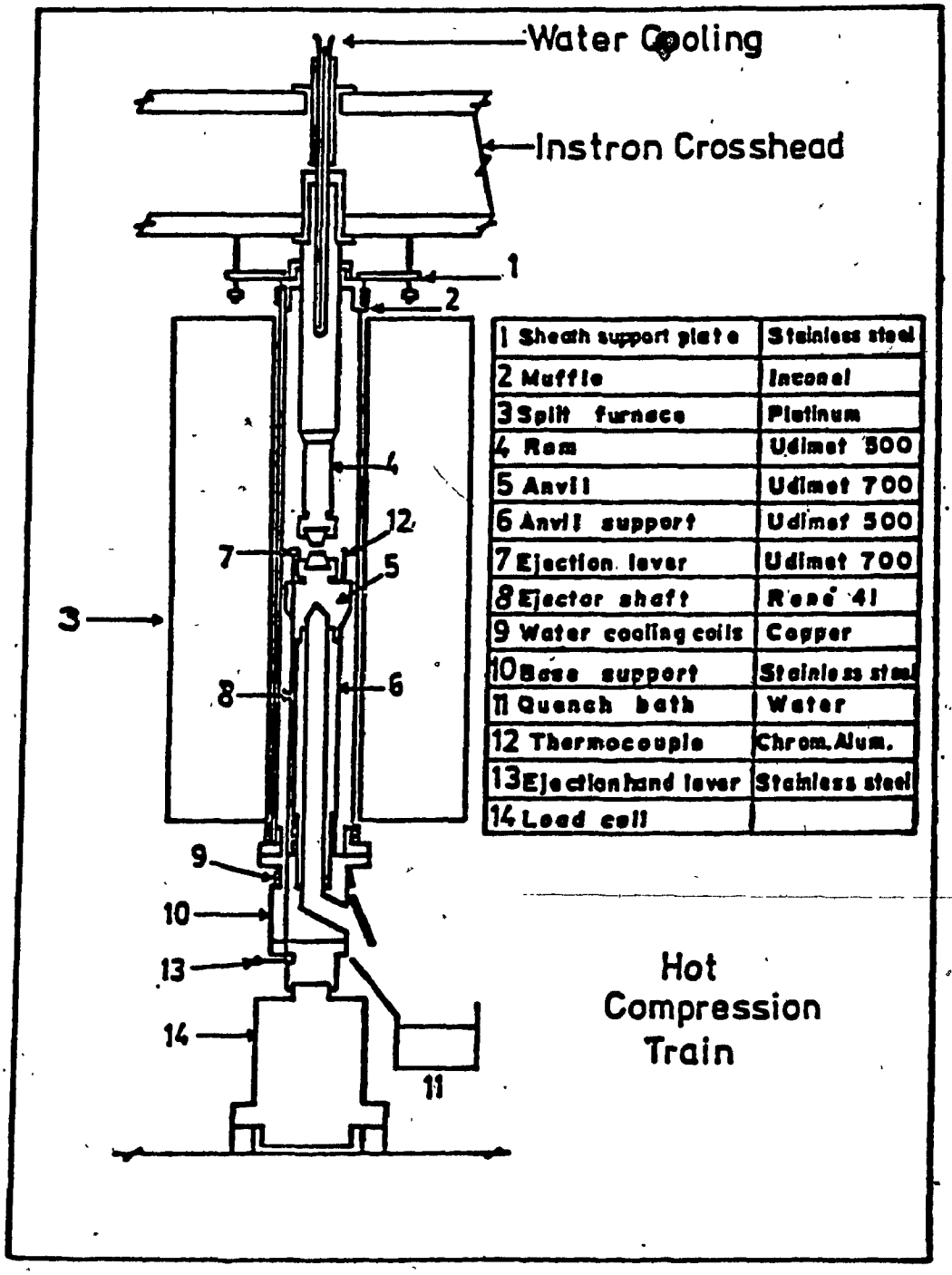

1 Sheath support plate	Stainless steel
2 Muffle	Inconel
3 Split furnace	Platinum
4 Ram	Udimet 500
5 Anvil	Udimet 700
6 Anvil support	Udimet 500
7 Ejection lever	Udimet 700
8 Ejector shaft	René 41
9 Water cooling coils	Copper
10 Base support	Stainless steel
11 Quench bath	Water
12 Thermocouple	Chrom.Alum.
13 Ejection hand lever	Stainless steel
14 Load cell	

Fig. 3.1 The hot compression train. (after Weiss (154))

and Northrup Electromax III controller. The furnace is supported by a lift mechanism designed by Petkovic (81), which (a) permits the furnace to be removed from the test chamber and (b) ensures that the furnace rides up and down with the crosshead.

3.1.1.2 Compression Tools for High Temperature

The compression tools consist of the upper and lower anvils and their supports (Fig. 3.2). Excellent results were obtained with alumina inserts; earlier experience (81) with superalloy inserts showed that the faces of these became indented after relatively short periods of use.

3.1.1.3 Control of Test Variables

3.1.1.3.1 Temperature Control

The temperature of each zone of the furnace was monitored by three Pt/Pt-13% Rh thermocouples. The specimen temperature was measured by a chromel-alumel thermocouple which was attached to the lower anvil close to the sample. The thermocouple output was monitored by means of a digital thermometer.

3.1.1.3.2 Atmosphere Control

The samples were tested under a flowing atmosphere of argon of high purity supplied by the Canadian Liquid Air Co., and additionally purified by being passed through a

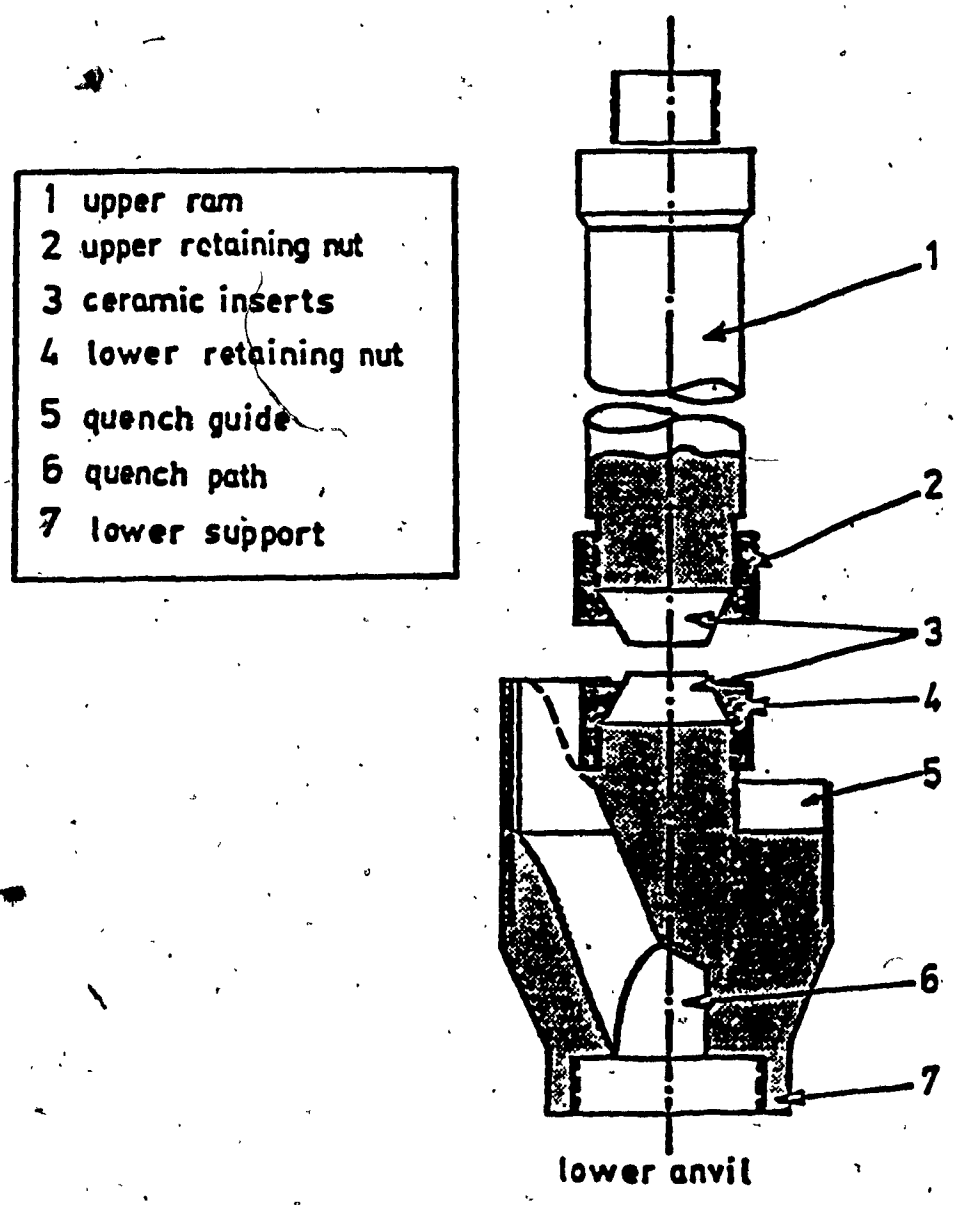

Fig. 3.2. The hot compression tools. (after Weiss (154))

deoxidizing train. Before the argon was introduced, the air was evacuated from the furnace chamber down to $5X10^{-2}$ Torr by a mechanical vacuum pump.

3.1.1.3.3 Strain Rate Control

In a uniaxial compression test carried out at constant crosshead speed, the true strain rate continuously increases. To produce a constant true strain rate, it is necesary to vary the crosshead velocity proportionally to the instantaneous height of the specimen, as shown below.

The true strain in compression is given by

$$\varepsilon = - \ln (h_o/h) \tag{3.1}$$

where h_o is the initial height of the sample and h its instantaneous height. From (3.1), the true strain rate is given by

$$\dot{\varepsilon} = 1/h \ (dh/dt) \tag{3.2}$$

In equation (3.2), dh/dt is the crosshead velocity V, and $\dot{\varepsilon}$ the strain rate of the test, is constant under the present conditions, i.e. $\dot{\varepsilon} = \dot{\varepsilon}_c$. By rearrangement, Eqn. (3.2) becomes

$$V = \dot{\varepsilon}_c h \tag{3.3}$$

Equation (3.3) implies that the crosshead speed must

decrease linearly with the sample height during a true strain rate compression test. Luton et al. (157) designed a device which varies the crosshead speed according to Eqn (3.3) in conjunction with the Instron Variable Speed Unit.

3.1.1.4 Instron Monitoring, Data Acquisition and Handling

The Instron controller is interfaced to a General Electric GE/PAC 4020 process control computer. The interface was designed to select the following modes of Instron operation at the will of the program: DOWN, STOP, and UP. In addition, the Instron could be returned to manual operation by selecting "NORMAL". The computer is also linked to the outputs of the load and displacement measuring devices.

The displacement transducer and the load cell are excited by two Hewlett-Packard series 6200 DC power supplies. The low level output of the load cell, 15 mV/1000 kg, is amplified by a factor of one hundred. Since the output of the displacement transducer is 2.7 V/cm, it is connected directly to the computer via a communication cable specially designed to minimize noise pickup.

The data obtained using the aquisition programs consist of the test parameters, i.e. the voltage outputs from the displacement transducer and load cell, and the time at which each reading is taken. These data are converted

into stress-strain form by means of a plotting program and plotted by means of a digital plotter. In a separate operation, the true stress/true strain curve can be expanded to 0.1 strain full scale for accurate determination of the yield stress.

Curves of relaxation stress vs time were obtained during the relaxation period by using a HEATHKIT Multispeed Servo Chart Recorder, which received the amplified output of the load cell.

3.1.2 Torsion Testing

3.1.2.1 Testing Assembly

The hot torsion machine was described in detail by Fulop et al. (158) (Fig. 3.3). One end of the sample is twisted a measured amount by a hydraulic motor (Fig. 3.4), while the other end is held fixed by a torque cell (Fig. 3.5). The load transmitted by the test specimen is measured by means of a torque cell of 100 N.m capacity. The rotary displacement of the motor is controlled by a closed loop MTS control system (Fig. 3.6) and measured with the aid of a dual gauge potentiometer which provides the feedback to the controller. The test pieces are heated by means of a water-cooled radiant furnace which is supported by the frame of the machine.

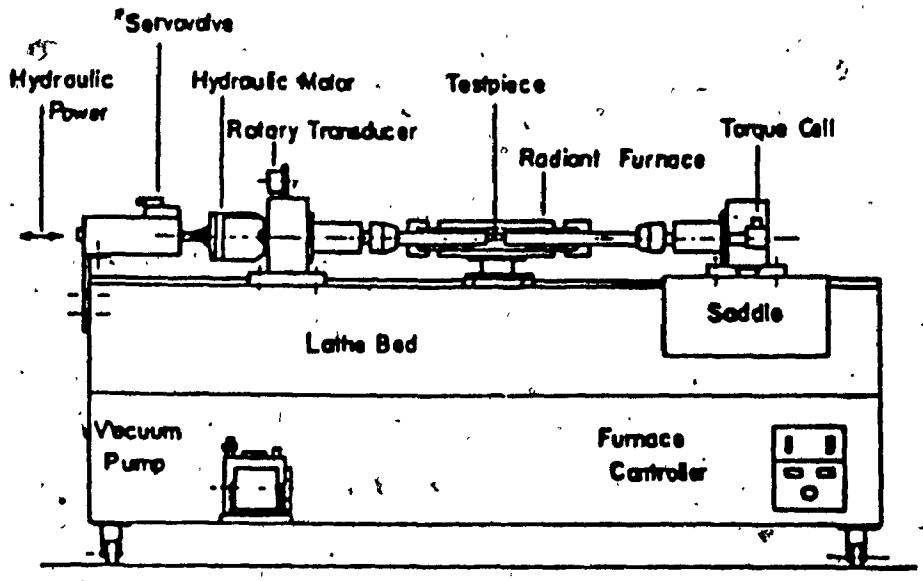

Fig. 3.3 The hot torsion machine. (after Fulop et.al. (158))

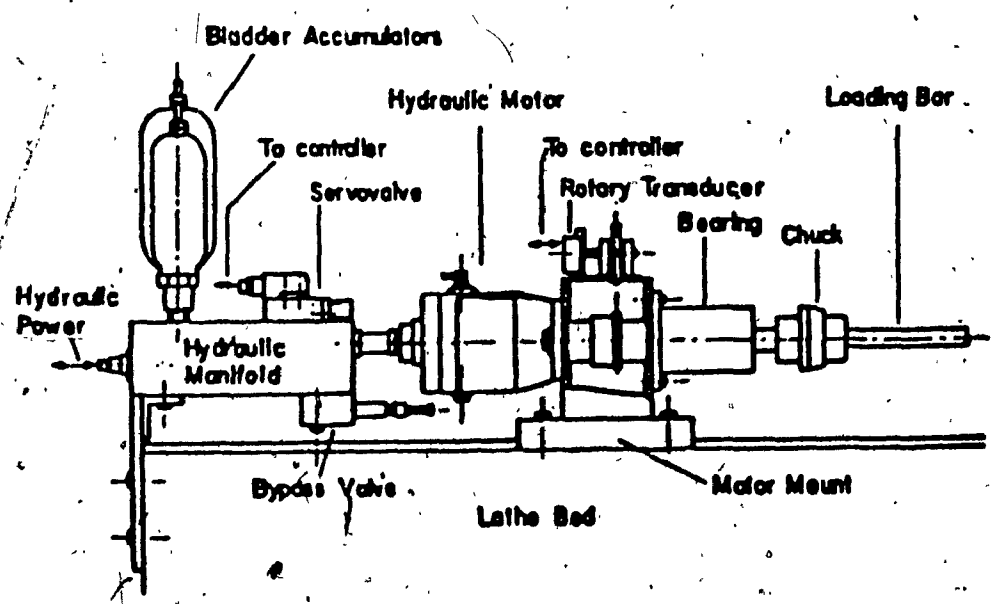

Fig. 3.4 Strain control and measurement subsystem. (after Fulop et.al. (158))

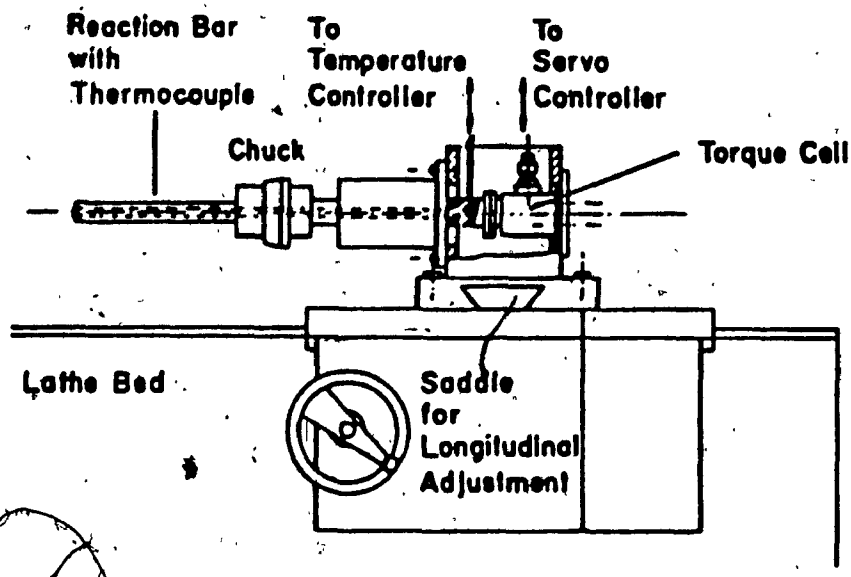

Fig. 3.5 Torque cell assembly. (after Fulop et.al. (158))

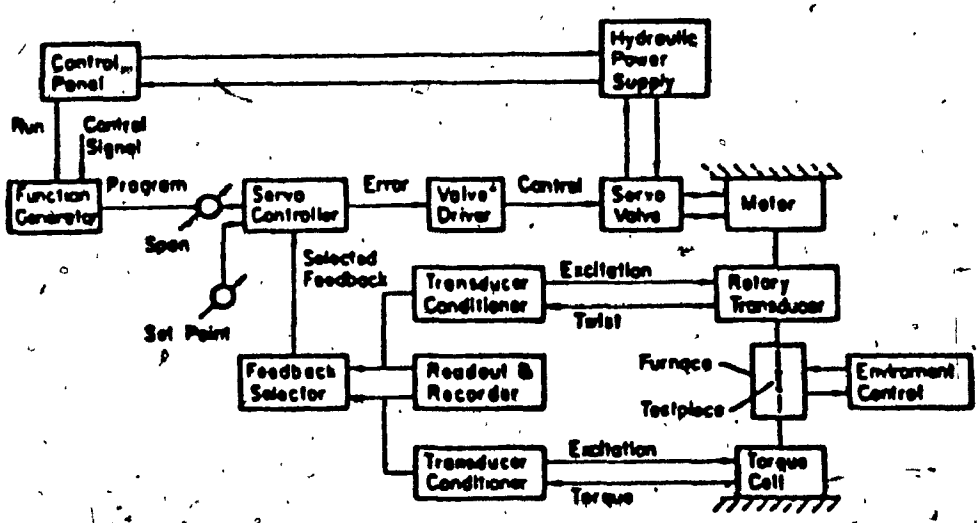

Fig. 3.6 Schematic diagram of the control and data acquisition systems. (after Fulop et.al. (158))

3.1.2.2 Torsion Tools for High Temperature

The test pieces are supported by means of nickel-based superalloy loading bars which are in turn connected to the motor and the torque cell by self-aligning collet chucks (Fig. 3.5). Both ends of the chuck assemblies are supported in thrust bearings. The reaction bar, bearing assembly and torque cell are mounted on the lathe saddle, which can be moved axially on the lathe bed to facilitate specimen insertion and removal.

3.1.2.3 Control of Test Variables

3.1.2.3.1 Temperature Control

The temperature is controlled and programmed by an external programming device. The thermocouple which supplies the feedback signal to the programmer is of chromel-alumel. It makes contact with the test piece at the center of its gauge length. The temperature of the test piece, which is displayed on the screen of the programming device, can be controlled with an accuracy of $\pm 1.5°C$.

3.1.2.3.2 Atmosphere Control

An inert atmosphere is produced during testing by the flow of argon through small holes uniformly distributed along the surface of the furnace walls.

3.1.2.3.3 Strain, Strain Rate and Stress Control

The twist rate, the twist direction and amount of twist are controlled by the appropriate opening of the servo valve. The electrical command signal for the servo valve is produced by a minicomputer through a suitable program.

In the solid torsion bars, which were used in this work, the strain, strain rate, and stress vary from zero at the axis to a maximum at the surface. The equivalent surface strain and strain rate were calculated by using von Mises criterion, i.e.

$$\varepsilon = \gamma / \sqrt{3} \tag{3.4a}$$

where ε and γ are the equivalent normal and shear strains, respectively. An equivalent form of Eqn.(3.4a) is

$$\varepsilon = 2 \pi N R' / L' \sqrt{3} \tag{3.4b}$$

where N is the number of turns, and R and L are the radius and gage length of the sample, respectively. The strain rate is given by

$$\dot{\varepsilon} = 2 \pi \dot{N} R' / L' \sqrt{3} \tag{3.5}$$

where $\dot{N}$ is the twist rate.

The equivalent normal stress was calculated applying von Mises Criterion to the Fields Backoffen relationship

(159), i.e.

$$\sigma = \sqrt{3}(M_T/2\pi R^3)(3 + m' + n') \quad (3.6)$$

where M_T is the torque, m' the strain rate sensitivity and n' is the strain-hardening exponent. m' and n' are defined by the expressions

$$m' = \log(\sigma_2/\sigma_1) / \log(\dot{\varepsilon}_2/\dot{\varepsilon}_1) \quad (3.7)$$

and

$$n' = \log(\sigma_2/\sigma_1) / \log(\varepsilon_2/\varepsilon_1) \quad (3.8)$$

The values of m' and n' for the present test conditions are m' = 0.047 and n' = 0.785.

3.1.2.4 Machine Monitoring, Data Acquisition and Handling

Control of the test is accomplished in the following manner. The servo controller (Fig. 3.6) receives the command signal from a PDP 11/04 minicomputer through the span control. This signal is summed with the static command, or off-set, determined by the set point control. The composite command is compared with the feedback signal from the rotary displacement transducer and an error signal is generated that is proportional to the difference between the programmed value and the current value of the controlled variable. The error signal is amplified by the valve driver module and sent to the servo valve. In this way the servo

valve is positioned so as to cause the motor to turn in such a way that it cancels the position error.

The minicomputer is also used to record the twist and the torque with the aid of the Data Acquisition (DACQ) statement, which picks up the values of these variables at predefined time intervals. The programming language employed for this purpose is MTS-BASIC which is loaded from a disk by means of a Tektronix 4010 terminal with a cathode ray display. The curves plotted from the data are displayed on a videoscreen. A Tektronix 4631 hard copy unit connected to the terminal provides permanent copies of the curves.

3.2 Experimental Material

The electrolytic tough pitch (ETP) copper used in the present study was received as a 6m long, 9mm diameter rod, cold drawn and annealed. Its chemical analysis showed a purity of 99.98% with an oxygen content of 0.02%.

3.2.1 Machining

3.2.1.1 Compression Samples

Cylindrical specimens were machined from the rod in the as-received condition. Their dimensions, indicated in Figure 3.7, provide a length to diameter ratio of 1.5 which has been shown adequate to promote homogeneous deformation (45, 51, 81). The ends of the samples were grooved to

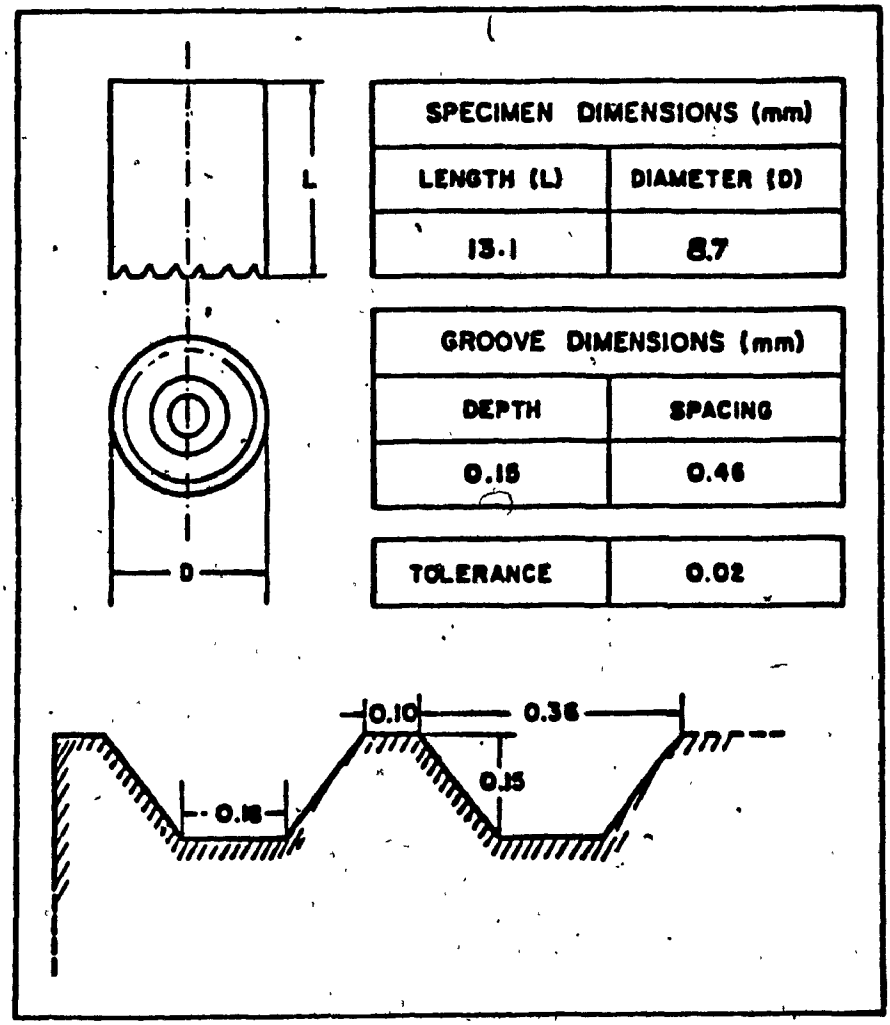

Fig. 3.7 Compression specimen dimensions and groove geometry.

retain the graphite lubricant (Dry Graphite Spray, supplied by ACHESON COLLOIDS (CANADA) LTD.). The choice of groove geometry was based on the work by several authors (49, 82, 160). The grooves are flat-bottomed and wider than the ridges between them.

3.2.1.2 Torsion Samples

Both ends of the torsion specimens were machined with rectangular sections. The advantage of this geometry is that the ends can be slipped into slots in the grips without being accidentally strained (158), (Fig. 3.8). McQueen and Jonas (164) reported that when a solid bar specimen is twisted with free ends, at high temperature, the test piece may change length, giving rise to changes in torsional strain and strain rate. However, Canova (161) determined in ETP copper using specimens with ends of rectangular section (free ends) that the changes in gage length were very small. Therefore, rectangular section ends were adopted for this work. Shoulders of intermediate diameter are provided between the gage length and the grip section to reduce the heat flow and the temperature gradient in the gage length. The dimensions of the test piece are displayed in Figure 3.8.

SPECIMEN DIMENSIONS (mm)	
A	54.0
B	12.7
C	6.35
D	6.35
E	9.5
F	3.2
G	1.6
H	7.6
J	9.5
K	7.2
L	25.4
M	85.7
R	1.6
W	11.2
TOLERANCE	0.05

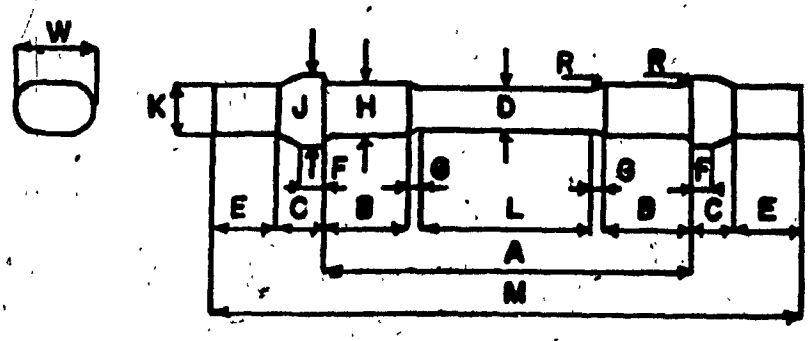

Fig. 3.8 Torsion specimen dimensions.

3.2.2 Heat Treatment

The samples were subjected to heat treatment with the purpose of producing a full annealed material of large grain size. There is a general agreement that grain boundary sliding during hot deformation is minimized by reducing the grain boundary surface (162, 163). The strain anneal procedure chosen is shown in Table 3.1. The samples after compression at room temperature were degreased using ultrasonic scrubbing in acetone and then rinsed in ethanol and dried. A moveable Lindberg Hevi-Duty high temperature furnace set at 900°C was used for the annealing treatment. The samples were placed in Sen-Pak stainless steel envelopes and put into a fused quartz furnace tube. The envelopes were tied to a stainless steel sheath which contains the chromel-alumel thermocouple. The temperature was controlled to ±1.0 degree. Once the vacuum in the quartz tube reached 10^{-5} Torr, the furnace was placed over the quartz tube to begin the heating process. At the end of the required 16 hours, the furnace was turned off, and room temperature was reached in about eight hours. By means of this procedure, a mean grain size of 300 μm was produced, as well as copper oxide particles of 2 μm average diameter.

Table 3.1. Strain-Annealing Treatments

Initial Treatment for Compression and Torsion Samples

1. Prestrain at room temperature

   0.5%

2. Annealing

   16 h at 900°C (in vacuum)

3. Cooling

   within the furnace

4. Material after annealing

   mean grain size: 300 μm

Treatment between Torsion Steps

A. Tests at 450°C, 1.8×10^{-1} s^{-1} (IIA).

1. Straining to 15%
2. with load-free annealing: 200 s

   with stress relaxation: 100 s

B. Tests at 450°C, or 500°C, 1.8 s^{-1} (III,IV)

1. straining to 50%
2. load-free annealing: 100 s

3.3 Experimental Methods

3.3.1 Compression Tests

The interrupted compression technique developed by Petkovic (81) was used to carry out the load-free annealing experiments after hot deformation (UL tests). The samples were deformed in compression at constant temperature and strain rate to about 0.15 strain (point A) fully unloaded and then annealed for increasing times at the deformation temperature (point B). Finally, they were reloaded at the same strain rate and temperature as before to produce the second portion of the curve. Figure 3.9 is a schematic representation of the procedure.

The technique developed to carry out the stress relaxation experiments (SR tests) in this work is now described in association with Figure 3.9. The temperature is kept constant throughout the test. Once point A is reached, the samples are held at constant total strain, and the stress relaxes by conversion of the elastic strain into plastic strain. After increasing periods of relaxation, the samples are unloaded (point B) for 1 second and then reloaded at the initial strain rate. From these two kinds of experiments the fractional softening occurring during different annealing times was determined by Eqn. 2.16.

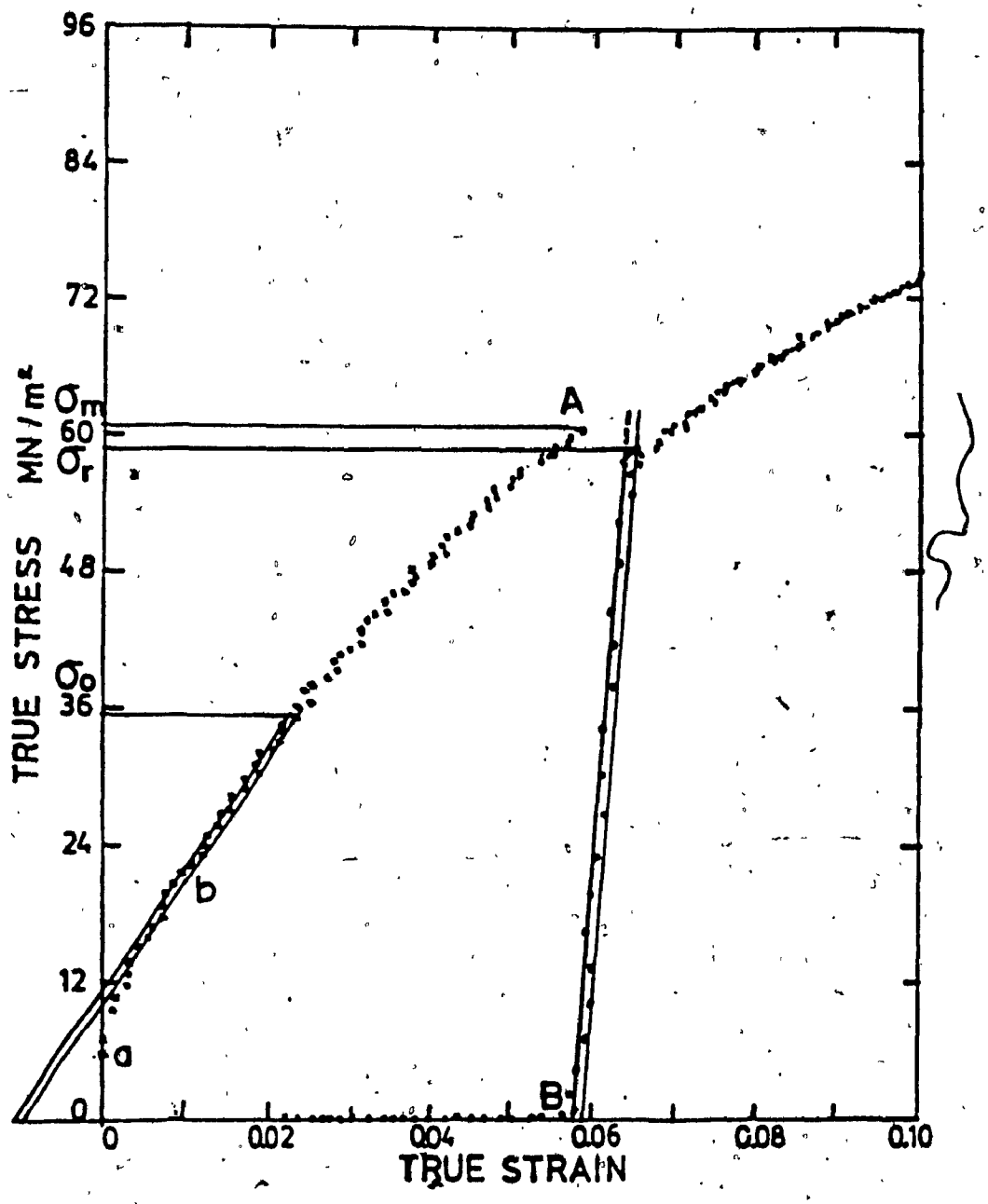

Fig. 3.9 Initial and reloading flow curves; 0.001 offset yield stress method.*

*The initial high slope (a) is due to the elastic deformation of the ridges between the lubricant grooves. The subsequent low slope (b) is due to the plastic deformation of the ridges as the main portion of the specimen deforms elastically. The slope falls again upon yielding of the specimen. The low slope (b) following (a) gives rise to the negative strain intercept upon extrapolation.

3.3.2 Torsion Tests

The cycle of deforming, load-free annealing (or relaxing), and reloading in torsion is similar to that in compression. However, since in torsion a single sample was subjected to multiple cycles, the reloading was extended to either 0.15 (IIA) or 0.5 (III and IV, Table 3.1) and a load-free annealing of 100-200s was inserted between cycles to cause the sample to recrystallize completely. By this means it was possible to restore the sample to the same grain size and yield stress at the beginning of every cycle of the test sequence. In the torsion tests the fractional softening was calculated as in compression. Each cycle renders a set of σ_o, σ_m and σ_r values and therefore a particular fractional softening (X).

3.3.3 Advantages of Compression and Torsion Tests

The compression test was used for several reasons: (1) The stress system is similar to those found in industrial deformation processes (164); (2) serious instabilities, such as necking, do not arise (165); (3) the occurrence of barreling (due to friction between platens and sample) can be reduced to a reasonable level by suitable lubrication and by proper geometrical design of the sample. Concentric grooves on the end faces of the specimen retain the lubricant improving its efficiency (51, 81). The

constraints due to friction decrease as the ratio height/diameter increases, but when the specimen height exceeds twice the diameter the sample may buckle. The ratio of 1.5 that has proved successful for zirconium (51), copper (81) and HSLA steels (166), was used in this work.

The torsion test is also extensively used for hot working studies because of several features. It is capable of producing high strains ($\sim$50) without instability and at high constant strain rates ($\sim$100 s^{-1}) so that industrial processes such as extrusion can be simulated (164). Torsion tests give flow curves which, up to moderate strains, are equivalent to those obtained by tension or compression when von Mises criterion is used (159). An important disadvantage of the torsion test is that there is a strain and strain rate gradient from zero at the axis to a maximum at the surface (161, 165). Thus, it is more difficult to correlate a specific structure with a particular flow stress.

The behavior of metals and alloys under different deformation modes has been studied by different authors who found the flow stresses developed at equivalent strain rates in torsion, tension and compression are comparable in the high temperature regime (161). The microstructures generated do not appear to be sensitive to the mode of straining(36). At high strains the flow stresses for different modes of

deformation often become quite different because of the development of different textures (161).

3.3.4 Test Conditions

The test conditions used in this work can be grouped as shown in Table 3.2. The temperature-corrected strain rates are related to a value Z_1 of $1.413 \times 10^{13}\ s^{-1}$ ($Z = \dot{\varepsilon} \exp((220 \times 10^3) / 8.32T)$, where 220 kJ/mole is the activation energy of deformation and 8.32 J/mole K is the universal gas constant).

The temperatures were chosen in the high temperature range, i.e. $T > 0.5T_m$. The strain rates were adjusted to yield the same temperature-corrected strain rate and thus obtain the same level of stress and of stored energy at a given strain. Thus, the rate of restoration should depend only on the temperature during the annealing interval. In other cases, the temperature was held constant but the value of Z increased to provide a much larger stress and consequently strain energy. The temperature and strain rate combinations were also selected to facilitate comparison with results obtained in previous research by this author (32).

The value of interruption strain ε_m varied slightly in compression because of variations in the initial gap between the surfaces of the sample and ram. In torsion, variations in strain arose because of adjustments between

Table 3.2. Testing Conditions

Set	Temperature °C (T/T_m)	Strain Rate s^{-1}	Z value s^{-1}	Interruption Strain ε_m	Peak strain ε_p	$\varepsilon_m/\varepsilon_p$
Compression						
1A	450 (0.53)	1.8×10^{-3}	Z_1^*	0.15±0.01	0.21	0.71
1B	540 (0.6)	9.3×10^{-2}	Z_1	0.15±0.01	0.27	0.56
IIA	450	1.8×10^{-1}	$100Z_1$	0.15±0.01	0.52	0.29
Torsion						
IIB	450	1.8×10^{-1}	$100Z_1$	0.15±0.01	0.49	0.33
III	500 (0.57)	1.8	$100Z_1$	0.15±0.01	0.51	0.29
IV	450	1.8	$1000Z_1$	0.15±0.01	0.63	0.24

$^*Z_1 = \dot{\varepsilon}_1 \exp(220{,}000/8.32\ T_1) = 1.413\times10^{13}\ s^{-1}$

sample and grips. The value of 0.15 includes both elastic and plastic strain. The values of ε_p and $\varepsilon/\varepsilon_p$ are also given in Table 3.2. The ratios $\varepsilon/\varepsilon_p$ are considerably below the critical ratio of 0.83 for initiation of dynamic recrystallization established by Rossard (50).

3.3.5 Preparation of Metallographic Samples

For every compression specimen reloaded, another compression sample was quenched immediately after 0.15 strain and the given load-free annealing or relaxation time. Longitudinal slices of about 1 mm were cut, for both metallography and electronmicroscopy, with a diamond disk. During the cutting operation, the sample was refrigerated with water. The metallographic samples were mounted in bakelite, ground on abrasive paper and polished, first with alumina and then chemically with an acid mixture developed by Lovel and Wernick (170). The reagent is composed of concentrated acids as follows: 10 ml H_3PO_4, 20 ml HNO_3, 4 to 40 mg $NaNO_3$, 4 to 40 mg NH_4Cl and 10 ml $HC_2H_3O_2$. The solution was held at a temperature of 80° C during polishing. The samples were polished by immersion for intervals of 3 s. A fresh solution was used for each sample.

The specimens for grain size measurement and for monitoring the progress of recrystallizaton were etched with the following solution: 4 g $K_2Cr_2O_7$, 16 ml H_2SO_4, 200 ml H_2O

and a few drops of HCl.

The torsion samples were prepared following the same procedure as for the compression ones. However, since the torsion samples were deformed several times in one set of tests they were quenched and observed only after the last one when full recrystallization had taken place. Because of the radial variation in strain and strain rate, tangential slices were prepared to observe the material close to the surface.

3.3.6 Preparation of Specimens for Electronmicroscopy

Progress of recovery was followed by electronmicroscopy in compression samples. The longitudinal slices were mounted in a jig and ground to a thickness of about 0.5 mm. Chemical thinning to a thickness of about 0.4 mm was carried out with a hot solution (80°C of 80 ml nitric acid and 20 ml of acetic acid. The slices were washed with tap water and with ethanol and dried. Disks of 3 mm diameter were cut from the slices with a tubular punch . The samples were finally thinned by electropolishing with a dual jet Metathin machine made by Materials Science, U.K. The electrolyte consisted of 25 ml of phosphoric acid, 25 ml of ethyl alcohol and 50 ml of water. The polishing conditions were 6 V, 120 mA and the temperature was 10°C. The material around the holes was observed in transmission

at 200 kV in a JEOL Model 200B electron microscope.

3.3.7 Metallographic Measurements

3.3.7.1 Grain Size

The grain size was determined by the Three Circle Intercept Counting Method described in the ASTM Standard E-112. The particular procedure used in this research based on this Standard is as follows:

1) A field of the sample at a magnification of 150X was projected on the ground glass of the microscope.

2) A transparency of the pattern for intercept counting (Fig. 3.10) was applied directly on the glass to 15 randomly selected fields.

3) The count of interceptions per pattern for each of the 15 fields was separately recorded on the worksheet shown in Figure 3.11.

4) The average $\bar{N}'$ of the intercept count was calculated.

5) Using the value of $\bar{N}'$ and the magnification (150X), the mean intercept distance ($\bar{I}$) was determined in Fig. 3.12.

6) The deviations ΔN from the average were calculated by $\Delta N_i = N_i - \bar{N}'$.

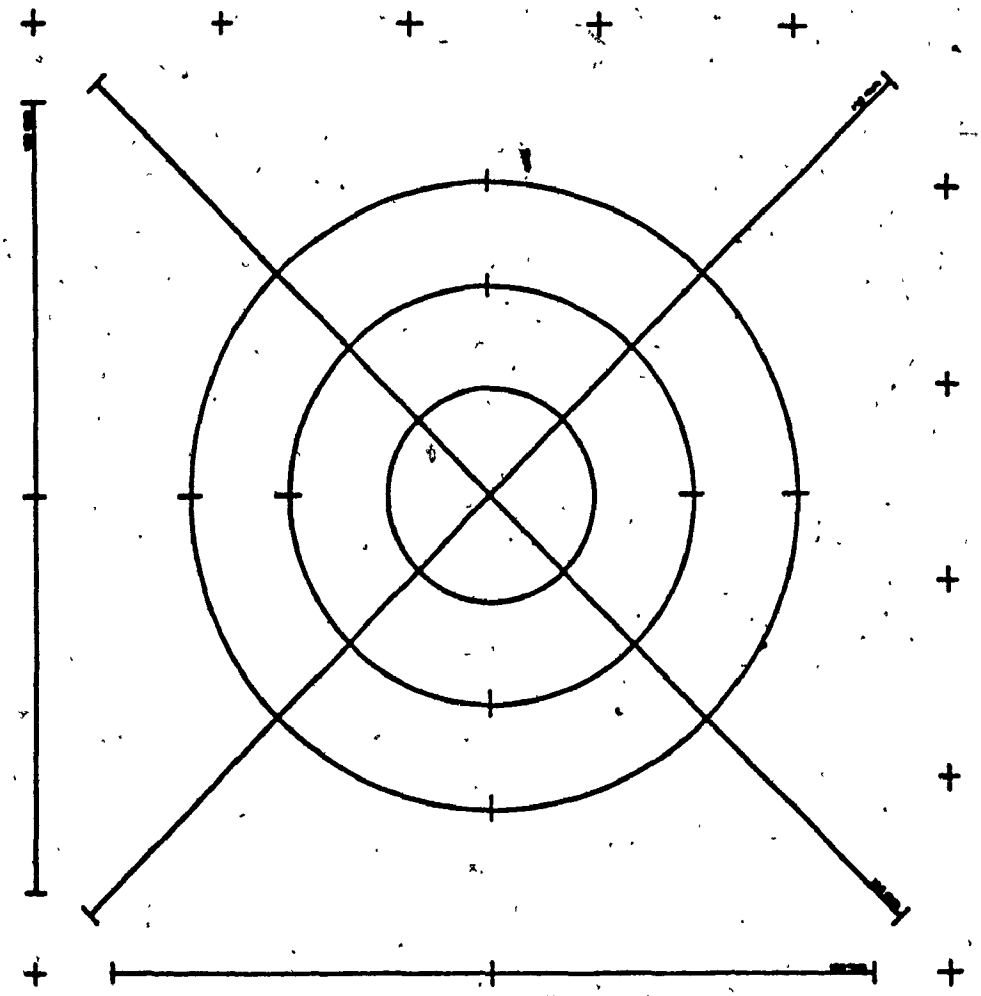

If reproduced to make straight lines marked length:
Straight lines total: 500 mm

Circles are:	Circumference, mm	Diameter, mm
	250.0	79.58
	166.7	53.05
	83.3	26.53
Total	500.0	

Fig. 3.10 Test pattern for intercept counting (ASTM E-112).

Sample number _____ Job number _____ Date _____

Material _____ Estimated grain size number _____

Processing _____ Magnification used for count _____ X

Sectioning direction: L T N Method: Intercept ▭ Planimetric ○

Line Array: ● |X ||||| ≡ Length if NOT 500mm: _____

Observations				Confidence Limits
i Field no.	Ni no of intercepts	$\Delta N = N_i - \bar{N}'$	$(\Delta N)^2$	C.V. = $\frac{S_o}{\bar{N}'}$ = ——— = [ ]
1				Using the C.V. calculated and Figure 8, determine the 95% confidence limit on the ASTM size number. Record below.
2				
3				
4				Using the C.V. calculated and Figure 9, estimate the % Accuracy of the Mean Intercept Distance, $\bar{l}$.
5				
Sum =		Sum$(\Delta N)^2$ =		% Accuracy = [ ]
$\bar{N}'$ (average) = $\frac{Sum}{5}$ =		$V = \frac{Sum}{4}$ =		Multiply the value of $\bar{l}$ by the accuracy of $\bar{l}$ and record the 95% confidence limit on $\bar{l}$.
$n\bar{l}$ =	/mm	$S_o = \sqrt{V}$ =		
ASTM size number = _____ ± _____			(Fig. 6-8)	← Record values for ASTM N and size on the report sheet.
$\bar{l}$ = Mean Intercept Distance = _____ ± _____			(Fig. 7-9)	

Additional Observations; (when necessary for required precision)

i	Ni	ΔN	$(\Delta N)^2$	i	Ni	ΔN	$(\Delta N)^2$
6				18			
7				19			
8				20			
9				21			
10				22			
11				23			
12				24			
13				25			
14				26			
15				Sum =		SUM$(\Delta N)^2$ =	
16				$\bar{N}$ =		$V = \frac{SUM}{n-1}$ =	
17				ASTM N =		$S_o = \sqrt{V}$ =	

Fig. 3.11 Grain size worksheet (ASTM E-112).

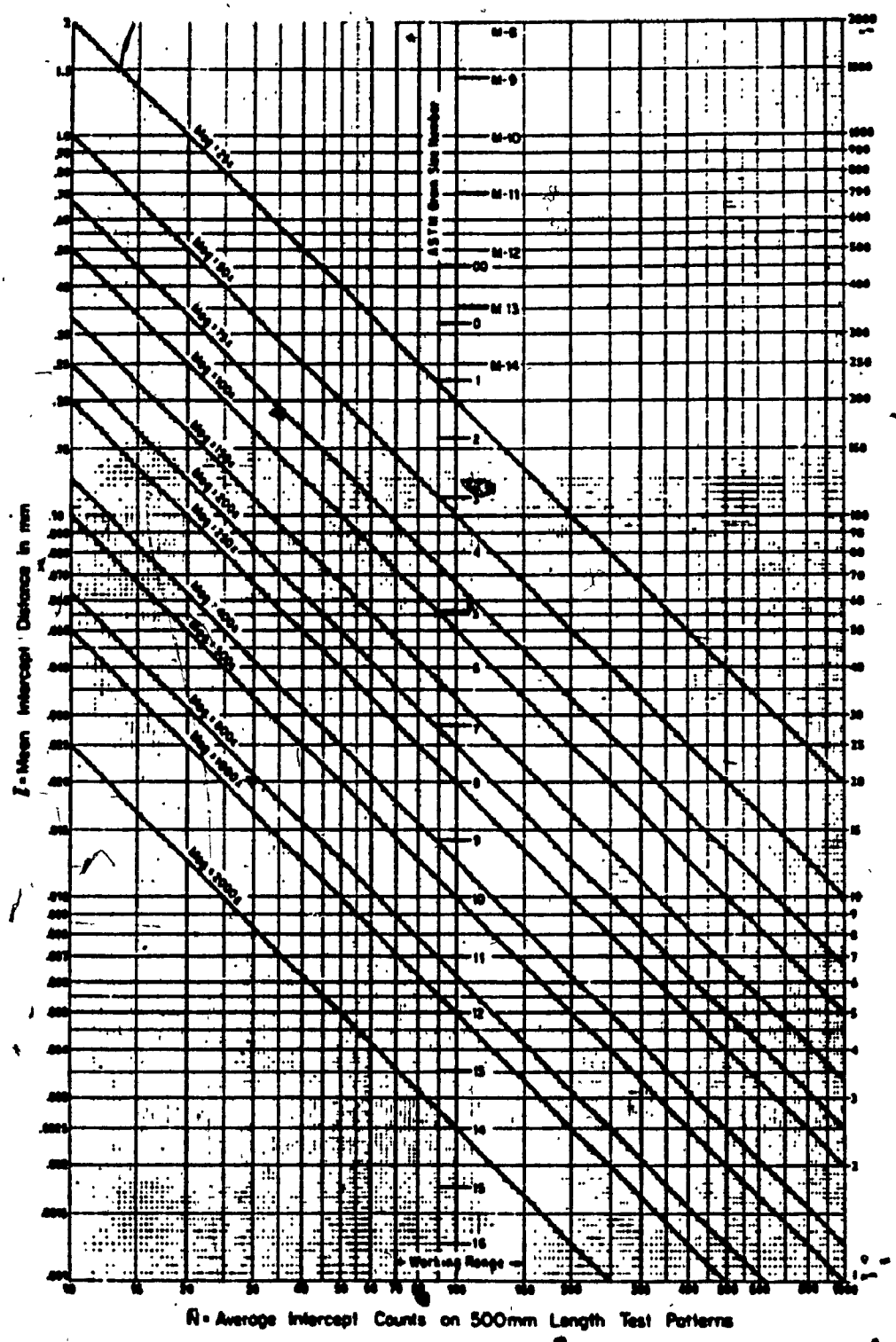

Fig. 3.12 Chart for direct determination of mean intercept distance from intercept count on 500 mm test pattern (ASTM E-112).

7) Each ΔN value was squared and recorded.

8) The variance of the observed counts relative to $\bar{N}'$ was calculated as follows:

$$V_o = ((\Delta N_1)^2 + (\Delta N_2)^2 + \ldots + (\Delta N_i)^2)/(i-1) \qquad (3.9)$$

9) The apparent ~~standard~~ deviation of the counts was calculated by

$$S_o = \sqrt{V_o} \qquad (3.10)$$

10) The coefficient of variation of ~~N was~~ estimated from

$$C.V. = S_o / \bar{N}' \qquad (3.11)$$

11) The 95% confidence limit (C.L.) to be applied to the mean intercept distance ($\bar{I}$) was read from Figure 3.13 by locating the C.V. value and the number of tests (fields). The C.L. is shown in this figure as a fraction of $\bar{I}$. Therefore the value of $\bar{I}$ was multiplied by that of C.L. and the result was attached to the value of $\bar{I}$ already determined.

An average of 250 intercepts were measured in the 15 fields. The use of lower magnification (< 150X) would have improved the precision since a higher population of counts would have been obtained. However, at lower magnification the distinction between grain boundaries and twins became a

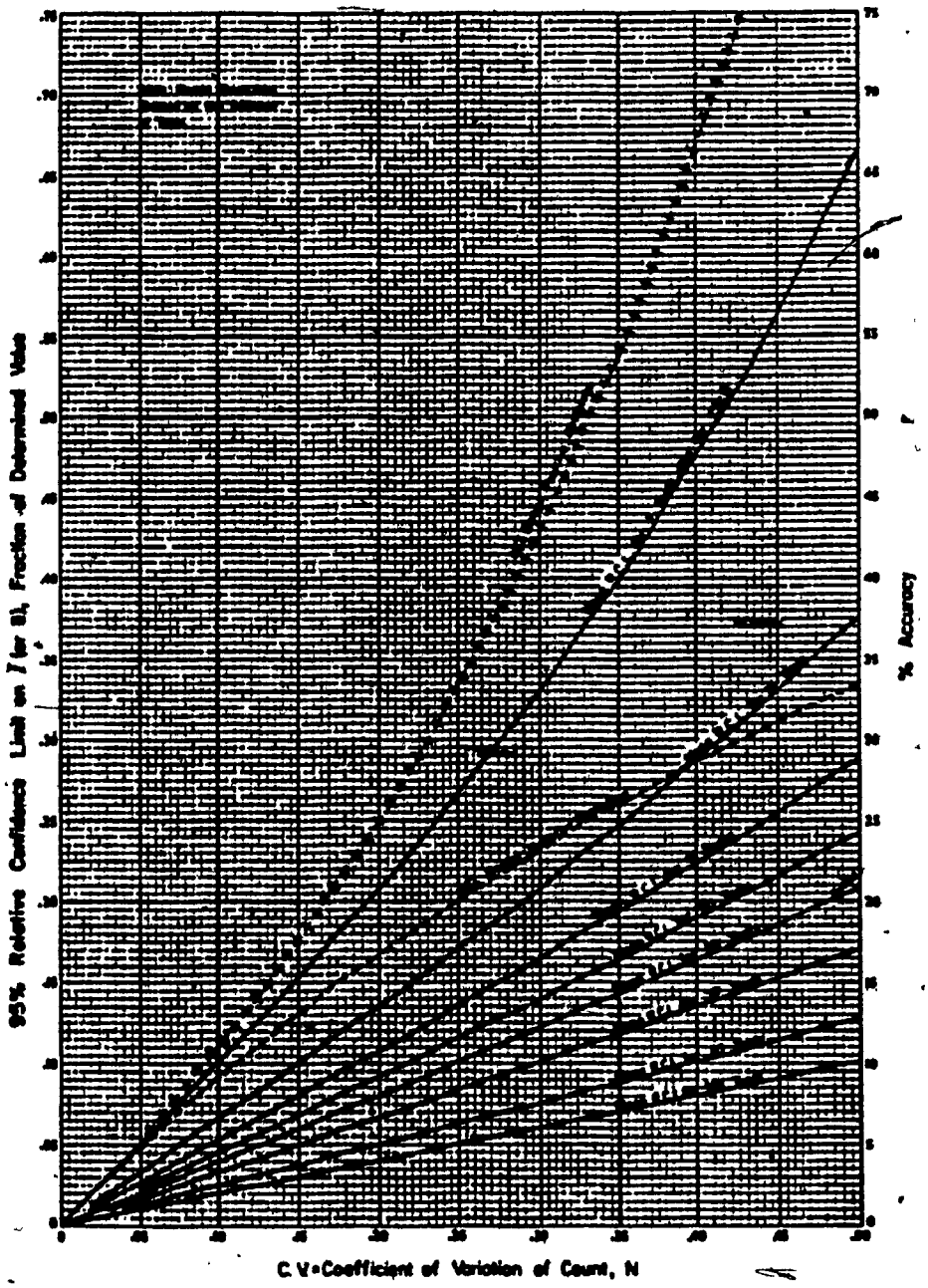

Fig. 3.13 Chart for determination of confidence limit on estimation of mean intercept distance (ASTM E-112).

difficult task.

3.3.7.2 Volume Fraction Recrystallized

The point-counting method is the one most used for volume fraction measurements. Hilliard and Cahn (171) showed that a systematic point count is markedly superior to other methods in terms of efficiency, in that it requires the least amount of effort to obtain an estimate with a given sampling (172).

The procedure used in this work is as follows:

1) A transparency of a 121 point-grid (with a separation of 7 mm between neighbouring parallel lines) was placed over a projected image on the ground glass of the microscope. Two magnifications were used: 50X for low values of volume fraction recrystallized and 150X for high.

2) The volume fraction recrystallized (X_R) in a field was determined by dividing the number of intersections which fell in a new grain by the total number of intersections. X_R was measured in 6 fields (n=6).

3) The apparent standard deviations of the intersections was calculated as in the case of grain size determinations (steps 4 to 9).

4) The standard deviation of a sample mean was estimated by

$$S_{xv} = S_o/\sqrt{n} \tag{3.12}$$

The 95% confidence limits (C.L.) were calculated from

$$C.L. = t \cdot S_{xv} \tag{3.13}$$

where t is a statistical factor for n-1 = 5, t = 2.571. Finally, X_R is given by

$$X_R = X_R \pm C.L. \tag{3.14}$$

Old grains have serrated boundaries and their surfaces appear intensively etched. These are characteristics which make it possible to distinguish them from the new more perfect grains which present a bright surface in the microscope.

3.3.8 Electronmicroscopic Measurements and Observations

The progress of recovery can be followed by measuring the properties which change with the annealing time such as dislocation density, subgrain size, sub-boundary thickness and misorientation between neighbouring subgrains. It should also be expected that qualitative differences arise between substructures of hot worked and annealed samples.

Subgrain size was determined by counting the number of subgrains in each of a series of electronmicrographs of fixed size and magnification. The subgrain size, however, did not show any trend of variation with annealing time. An explanation for this observation is that the measurements were insufficient to reach a statistically valid conclusion. A qualitative analysis of micrographs taken after different annealing times with respect to dislocation density and sub-boundary thickness as well as some misorientation determinations will be reported.

3.3.8.1 Subgrain Misorientation Measurement

Precise measurements of subgrain misorientation were made by the Kikuchi method. Kikuchi lines are produced by diffraction of the inelastic electrons which are incident on the crystal planes at the Bragg angle. These are pairs of bright and dark lines associated with a diffraction spot (173). Figure 3.14 shows a diagram of two Kikuchi patterns corresponding to two neighbouring subgrains. The displacement x of the intersection points of the pattern allows one to determine the subgrain misorientation by the equation

$$\theta' = x/L \qquad (3.15)$$

where θ' is given in radians and L is the camera length of the electronmicroscope (L=77.2 cm).

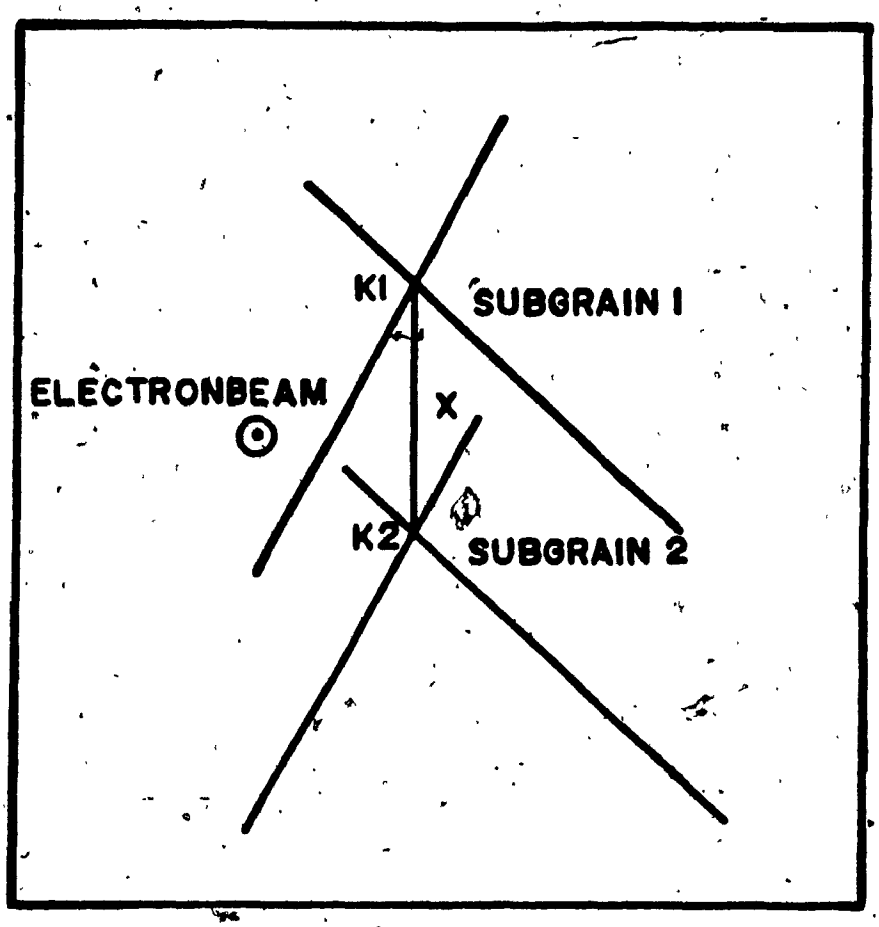

Fig. 3.14 Kikuchi patterns of two neighboring subgrains.

Misorientation between two subgrains in the microscope is equivalent to a fully-annealed monocrystal observed before and after rotation around an arbitrary axis. Equation (3.15) gives the rotation of the lattice around an axis perpendicular to the electron beam axis. When the lattice rotates around the electron beam axis, θ must be corrected for this. However, in many practical cases the latter rotation is small and can be neglected. Such assumption was made in this work.

3.4 Analysis of Data

3.4.1 Yield Stress Determination Methods

Figure 3.9 illustrates the type of initial and reloading stress vs strain curves obtained in the compression tests of this work. Upon loading, the initial curve shows a gradual curvature indicating the transition from elastic to plastic deformation. When the specimen was reloaded after load-free annealing or stress relaxation an initial transition was also observed. After the transients, at larger strains, the material exhibited "true" plastic behavior. The presence of transients represented a problem for getting precise yield stress values.

3.4.1.1 The Back Extrapolation Method

The yield stress in this method is determined by back-extrapolating the stress-strain curve to zero plastic

strain. The method uses a "master" curve that is the locus of the flow stress as a function of prestrain. This curve is obtained by a series of frequent unloadings and reloadings (allowing enough strain to take the material through the transient each time) (2).

Some advantages of this method are that the problem of short transients is avoided, the yield stress so defined is on the continuous flow curve, and thus corresponds to the state of the material at a particular strain. Moreover, the values of yield stress are more realistic, in particular, when they are used to estimate rolling loads in multiple-pass rolling when recovery is the only restoration process between stages. Some disadvantages of this procedure are that it is labourious and that, when the transients are long during recrystallization, its determinations are not accurate since the reloading and master flow curves do not coincide very well.

3.4.1.2 The Offset Yield Stress Method

The 0.1% offset (Fig. 3.9) has several advantages of which important ones are its ease, simplicity and reproducibility, especially at room temperature. It is able to give a precise yield strength for ductile materials which do not display either well defined elastic behaviour or a sharp transition to plastic flow such as a yield drop. Some

disadvantages of this method are that, after prior deformation at high temperatures with a short holding interval, an unrealistically low value of reloading yield stress is obtained because of anelastic effects.

The 0.1% offset method was selected for this work because its principal advantages, pointed out above, and because it was shown in a previous work by this author (32) that no important differences on the kinetics of recovery and recrystallization arise when either of these methods are used.

3.4.2. Fractional Softening

The mechanical technique to monitor the progress of softening is based on the equation

$$X = FS = (\sigma_r - \sigma_o)/(\sigma_m - \sigma_o) \qquad (3.16)$$

where X is the fractional softening, σ_m is the flow stress for 0.15 strain, σ_o is the yield stress of the initial fully-annealed material and σ_r is the reloading yield stress after the pre-strain of 0.15 and stress relaxation or stress-free annealing.

When recovery and recrystallization occur sequentially and separately, equation (3.16) can be used to monitor the advance of each by defining a lower limit value of σ_r (σ'_r) for recovery alone. X gives the level of

recovery when σ_r is equal or higher than this limit; the volume fraction recrystallized X_R can be estimated by defining $\sigma_m = \sigma'_r$ in Eqn. (3.16):

$$X_R = (\sigma'_r - \sigma_r)/(\sigma'_r - \sigma_o) \tag{3.17}$$

When recovery and recrystallization occur simultaneously

$$\Delta\sigma = \sigma_m - \sigma_r \tag{3.18}$$

is the sum of the drops in reloading stress due to recovery ($\Delta\sigma_{rr}$) and recrystallization ($\Delta\sigma_{rR}$):

$$\Delta\sigma = \Delta\sigma_{rr} + \Delta\sigma_{rR} \tag{3.19}$$

Here the second subscripts (r and R) denote recovery and recrystallization.

If there are procedures to determine the values of $\Delta\sigma_{rr}$ and $\Delta\sigma_{rR}$ (and therefore of σ_{rr} the reloading yield stress if only recovery had occurred), Eqn. (3.16) can be used to determine the fractional softening due to recovery (X_r) and Eqn. (3.17) that due to recrystallization (X_R). On the other hand if X_r and X_R can be determined by other methods σ_{rr} can be calculated by Eqn. (3.16).

For a given material σ_o and σ_m depend on Z, and σ_m additionally on ε_m. σ_r will depend moreover on the annealing time (t). After long times, σ_r will approach σ_o. If the recrystallized grain size is finer than the initial

grain , σ_r is higher than σ_o and becomes equal only if grain growth occurs. It is assumed that during annealing no aging takes place. As Z and ε_m are higher, the value of σ_r corresponding to full recrystallization differs more from σ_o. However, since the moderate strains used here do not result in much grain refinement, the present analysis defines the fully recrystallized state after deformation and annealing as $\sigma_r = \sigma_o$ since there is no better method of specifying it.

3.4.3 Fractional Relaxation

An equation similar to that for fractional softening was used to define fractional relaxation

$$X_{SR} = FR = (\sigma_m - \sigma_{SR}) / (\sigma_m - \sigma_{SRST}) \qquad (3.20)$$

σ_m is the stress at unloading and hence at the beginning of relaxation, σ_{SR} is the stress at the end of the specified period of relaxation and σ_{SRST} is the relaxation stress when the stress vs time curve becomes asymptotic.

3.4.4 Recrystalization Kinetic Curves

Several procedures have been proposed to determine the recrystallization kinetics of a metal. The choice of a particular method depends on the property which is going to be measured and if the measure only belongs to recrystallization or if it represents both recovery and

recrystallization. In this research, the volume fraction recrystallized X_R and the fractional softening X obeyed the Mehl-Avrami law although the X_R vs log time and X vs log time curves followed different paths. This fact suggests that recovery occurs and that it overlaps with recrystallization. A new method was developed to separate the recovery and recrystalization softening components. Because this method is based on the Mehl-Avrami law it will be described in what follows. The modification developed by Petkovic (81) for sequential recovery and recrystallization will be presented as well.

3.4.4.1 The Mehl-Avrami Law

The volume fraction recrystallized in isothermally load-free annealed or stress-relaxed samples after 0.15 hot straining was measured metallographically. A plot of X_R vs log time was used to describe the progress of recrystallization (Fig. 3.15a). After an initial incubation time in which no new crystals were observed, X_R varied sigmoidally with time. The experimental points followed the Mehl-Avrami law

$$X_R = 1 - \exp(-kt^p) \qquad (3.21)$$

X_R is the volume fraction recrystallized and the exponential term represents the non-recrystallized fraction at any time. A log $\ln(1/(1-X_R))$ vs log time plot is a straight line with

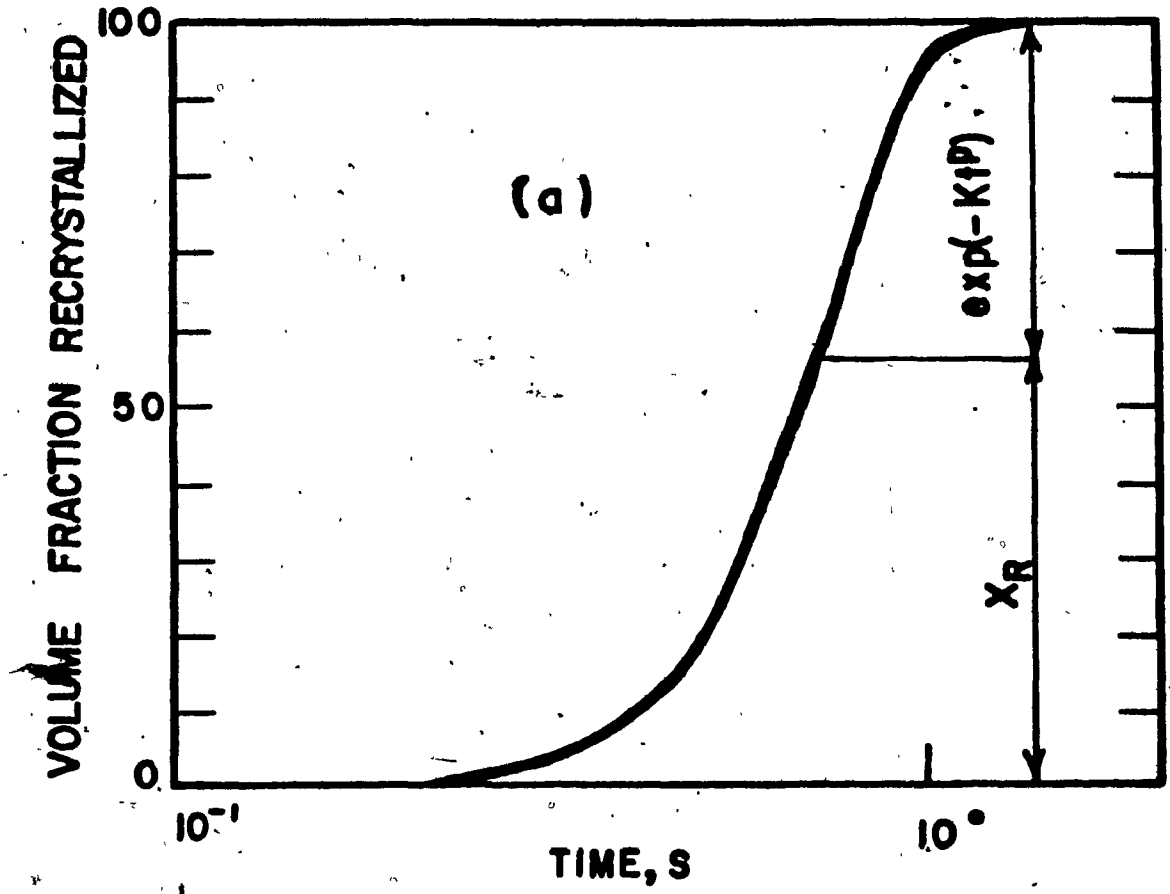

Fig. 3.15a Fraction recrystallized X_R as a function of log time showing incubation time.

slope p. The parameter k was directly estimated from Eqn. (3.21) once p was known.

3.4.4.2 Modified Mehl-Avrami Law, Sequential Mechanisms

Petkovic (81) found that static recovery and recrystallization occur sequentially in samples of ETP copper hot worked for various amounts. A plateau in the fractional softening vs log time curve clearly defined the end of recovery and the beginning of recrystallization (Fig. 3.15b) The fractional softening was defined in terms of flow stress values as given by Eqn. (3.16).

The overall softening produced for both recovery and recrystallization is given by the sum of the respective components, X_r and X'_R (softening of fully recovered material due to recyrstallization):

$$X = X_r + X'_R \tag{3.22}$$

When softening has gone to completion, Eqn. (3.22) becomes

$$X_\infty = X_{r\infty} + X'_{R\infty} \tag{3.23}$$

The volume fraction recrystallized at any time t is given by $X'_R = X'_{R\infty}\ (1-\exp(-kt^p))$ (3.24)

The terms of the equations above are defined in Fig. 3.15b. The slope of a log $\ln((X'_{R\infty}/(X'_{R\infty} - X'_R))$ vs log time plot gives the value of p and k calculated from Eqn. (3.24).

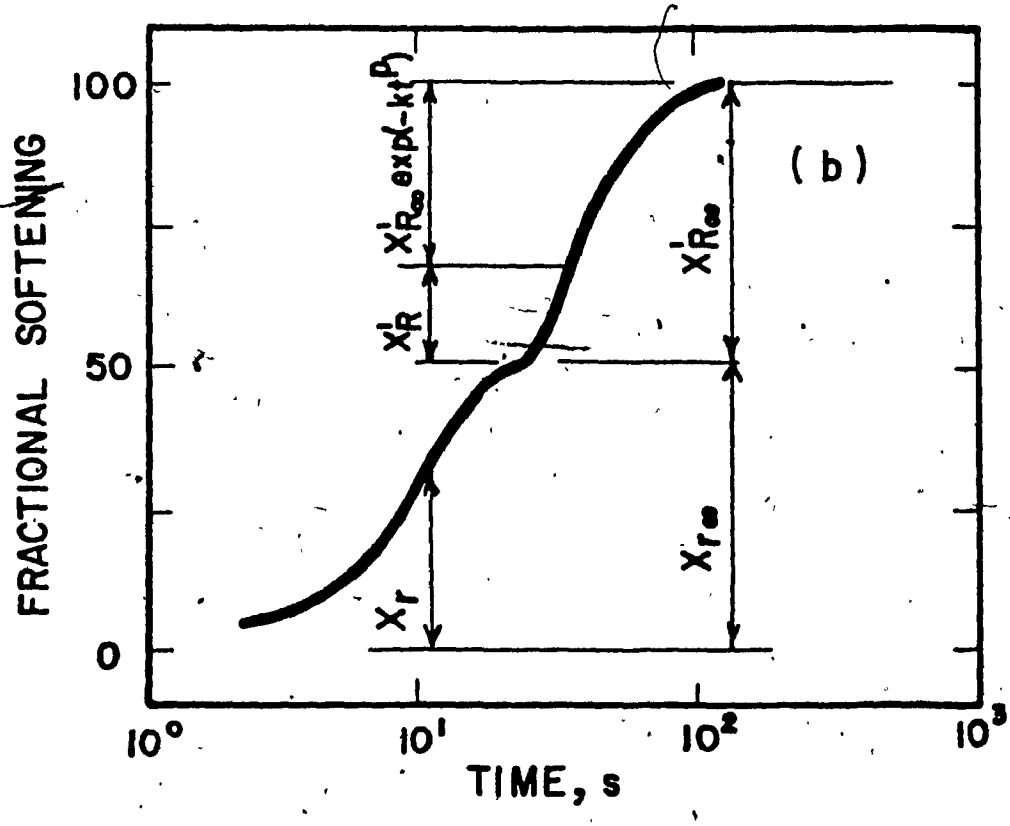

Fig. 3.15b Fractional softening curve (X) for sequential recovery X_r and recrystallization X_R. (after Petkovic (81))

3.4.4.3 Modified Mehl-Avrami Law, Parallel Mechanisms

It is assumed that for short annealing times $X = X_r$ because $X_R = 0$. For intermediate annealing times, X is given by

$$X = X_r + X_R \tag{3.25}$$

where X_R is the recrystallization measured metallographically, which differs from Petkovic's approach. For long annealing times X approaches 1, $X_r \simeq 0$ and $X_R \simeq X$. X, X_r and X_R are determined by the recrystallization and softening curves as shown in Fig. 3.15c.

The X vs log time curve was plotted from the experimental data. The X_R vs log time curve was drawn from the experimental metallographic points and from the point determined by the time at which $X_R = X_{R\infty} = 1$. The parameters p and k of the latter curve were obtained by trial and error such that the plot best fitted the points and obeyed the Mehl-Avrami law (Section 3.4.4.1). These are thus the p and k for the volume fraction recrystallized. A second set of p and k values for each test condition was determined for the fractional softening X. The procedures for getting these parameters were the same as those described in Section 2.

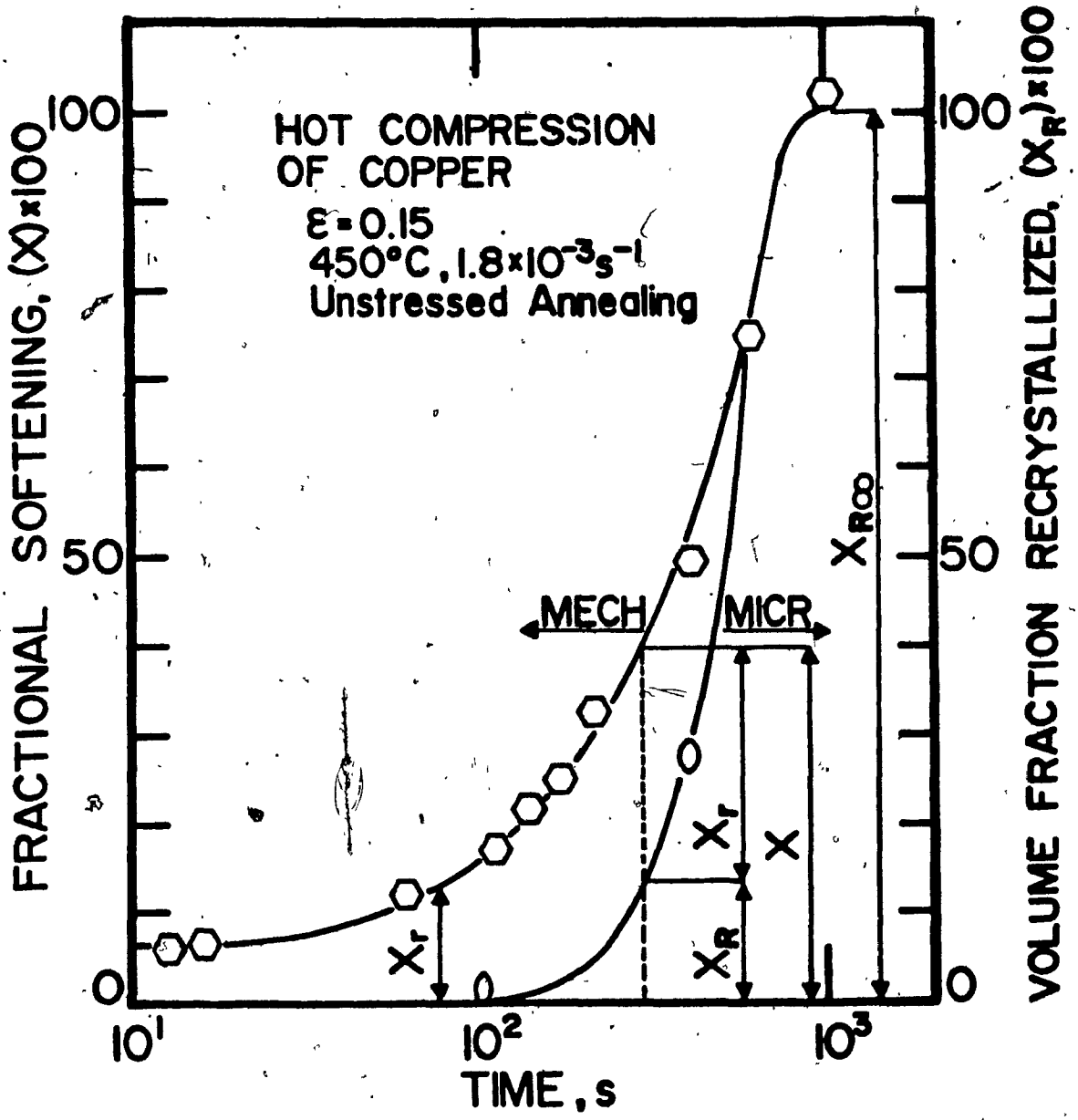

Fig. 3.15c Fractional softening (X MECH) and volume fraction recrystallized (X_R MICR) curves for simultaneous recovery X_r and recrystallization; present work.

3.4.5 Plotting of the Recovery Kinetic Curve

In the real situation as explained in Section 3.4.4.3, the material softens by recovery alone only during the first seconds of annealing but then by both recovery and recrystallization. In this case, the amount of recovery X_r at any time is calculated from Eqn. (3.25). The experimental material followed recovery kinetics (Eqn. 2.24):

$$\sigma_{rr} = \sigma_m - s \log (1+t/t_o) \qquad (3.26)$$

The procedure to plot the kinetic curves is as follows.

1. An average σ_m i.e. σ_{mav}, was calculated for all the tests run at a given test condition (same Z).

2. This value was inserted in the expression

$$X_r = (\sigma_{mav} - \sigma_{rr})/(\sigma_{mav} - \sigma_o) \qquad (3.27)$$

from which σ_{rr} values were determined.

3. A plot of σ_{rr} vs log t was drawn. This curve intersects the vertical axis at a point σ'_{int} which corresponds to the intersection of the X vs log t curve (Fig. 3.10a).

4. For t >> 1, Eqn. (3.26) becomes

$$\sigma_{rr} = \sigma_{mav} - s' \log (t/t'_o) \qquad (3.28)$$

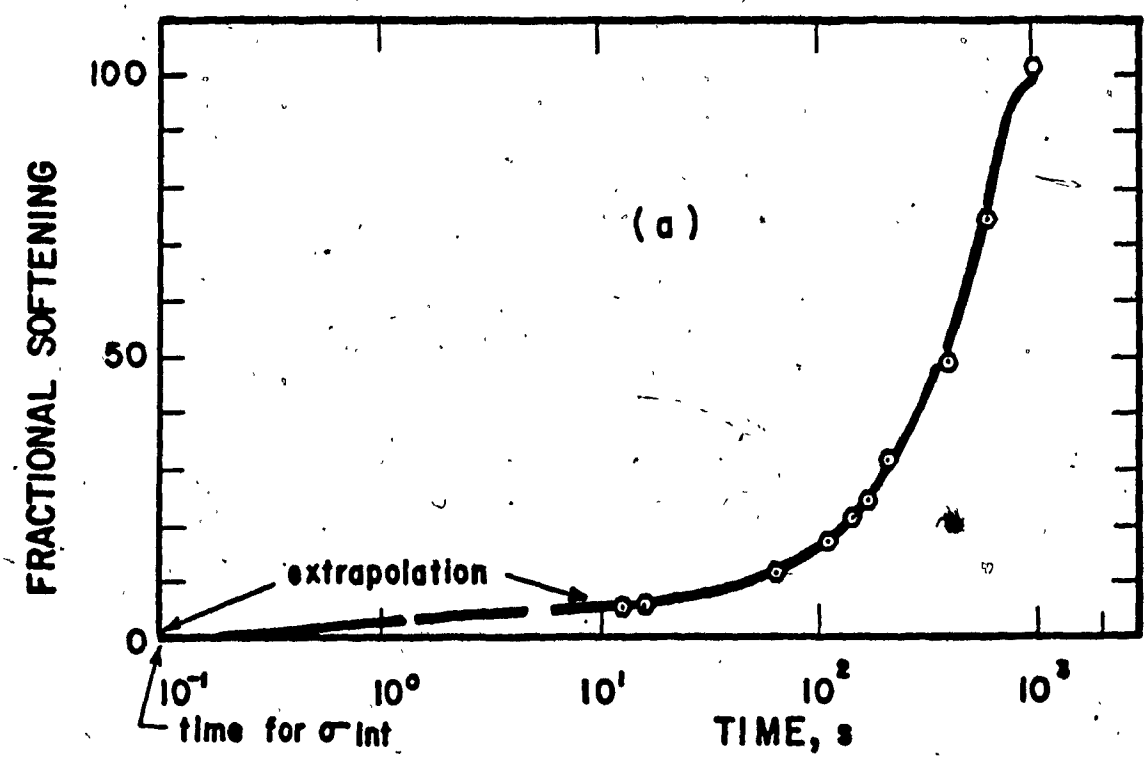

Fig. 3.16a Procedure for the determination of intersection stress to determine t_i.

Rearranging this equation gives

$$\sigma_{rr} = (\sigma_{mav} + s' \log t'_o) - s \log t \qquad (3.29)$$

Figure 3.16b shows that

$$\sigma'_{int} = \sigma_{mav} + s' \log t'_o \qquad (3.30)$$

Since s and σ_{int} are determined from Fig. 3.16b, Eqn. (3.30) allows one to calculate t'_o.

5. The values of $\log(1 + t/t'_o)$ were calculated and a curve σ_{rr} vs $\log(1 + t/t'_o)$ was drawn (Fig. 3.16c).

6. Because of inaccuracies in the extrapolation procedure, the new intersection stress σ_{int} sometimes doesn't coincide with σ_{mav}. When these values do not coincide, the curve and the experimental points were horizontally shifted until $\sigma_{int} = \sigma_{mav}$. By shifting the ordinate values σ_{rr} and s remain constant, but $\log(1+t/t'_o)$ and therefore t'_o change.

7. After shifting, a new value of t_o was calculated based on the new abscissa values $\log(1+t/t_o)$ of the experimental points.

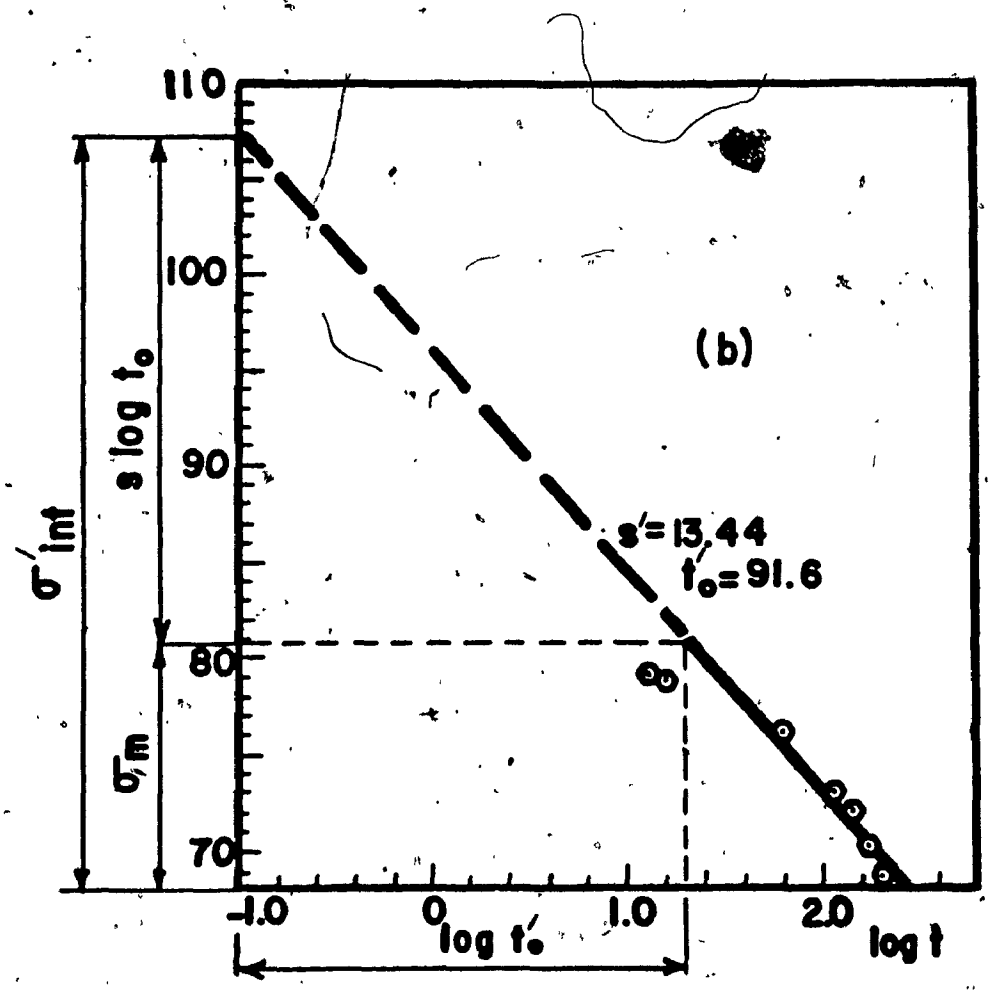

Fig. 3.16b Preliminary recovery kinetic curve of σ_r vs log t to determine t'_o.

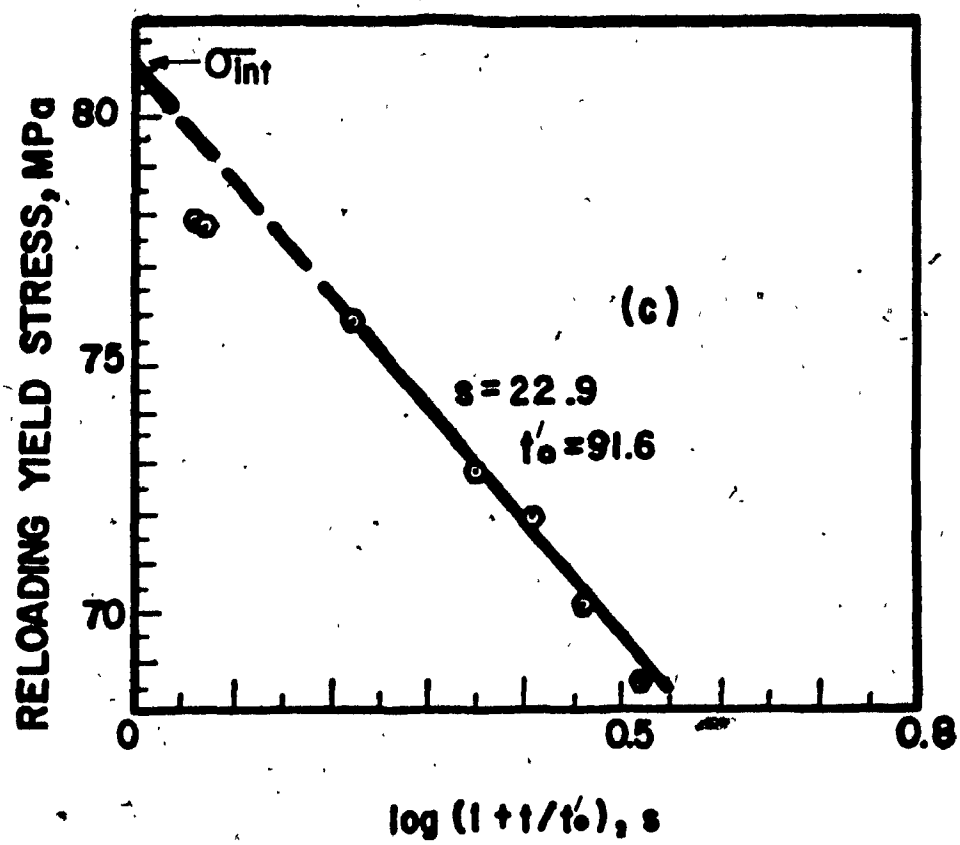

Fig. 3.16c Intermediate recovery kinetic curve to reevaluate t'_o.

CHAPTER 4

EXPERIMENTAL RESULTS

4.1 Flow Curves for Initial Deformation and Reloading

4.1.1 General Description

Figures 4.1 through 4.6 show examples of the flow curves obtained in the hot compression and hot torsion of the ETP copper samples. Each graph displays the initial loading curve of the full annealed material and a set of reloading curves. The continuous flow curves in figures 4.1 to 4.3 represent the continuation of the first deformation pass. The relevant features indicated or represented in these figures are: a) initial yield stress (σ_o); b) the stress reached at a compression or torsion strain of about 0.15 (σ_m); c) the reloading yield stress (σ_r); d) the peak stress (σ_p) and peak strain (ε_p) for the compression tests; e) the final stress relaxation levels, where applicable; f) the unloading or stress relaxation times, and g) the fractional softening percent.

Figures 4.1 and 4.2 show the compression curves belonging to the test conditions 450°C, 1.8×10^{-3}) s^{-1} and 540°C, 9.3×10^{-2} s^{-1} respectively, i.e. to those experiments

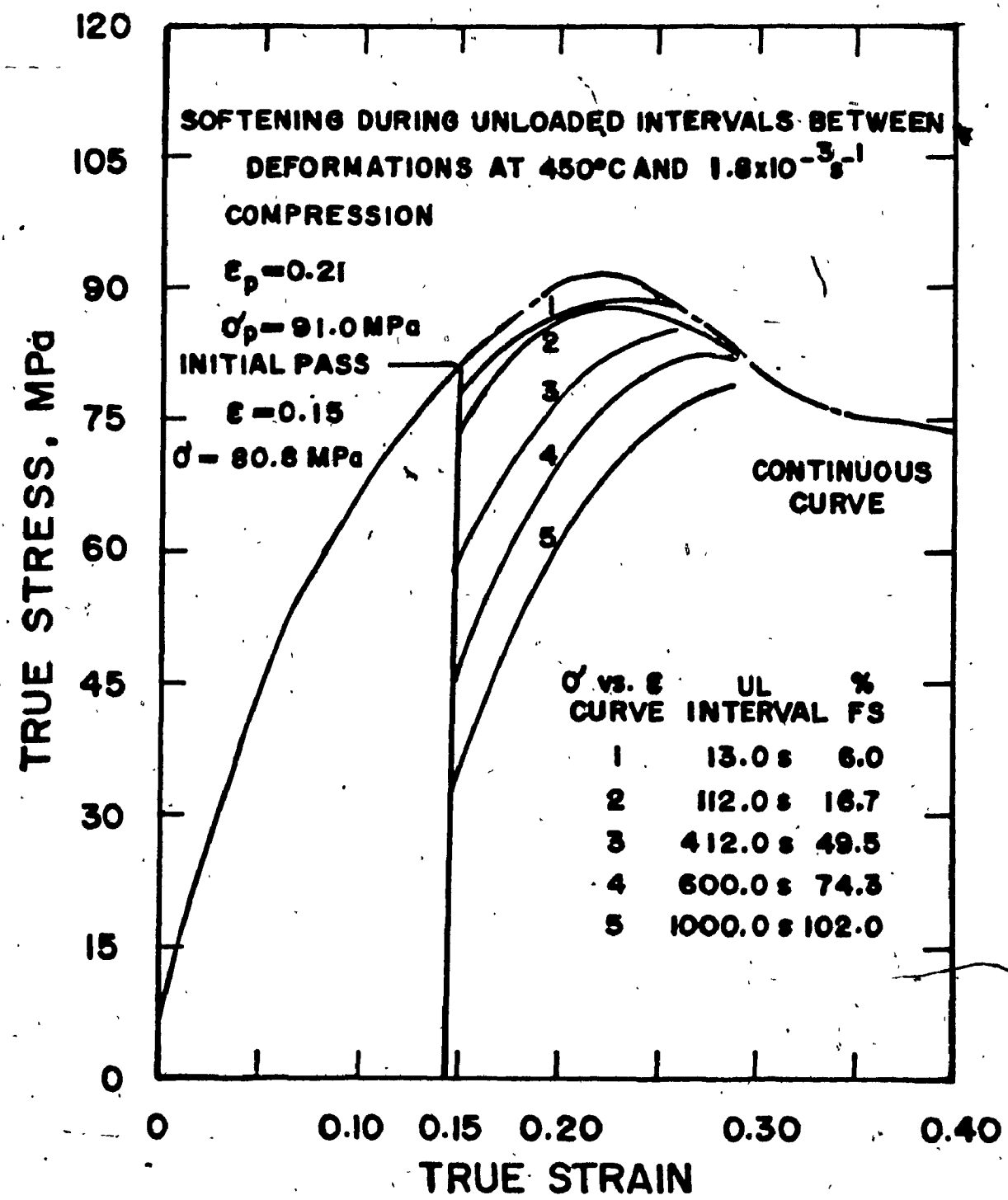

Fig. 4.1a Initial and reloading flow curves for the compression condition 450°C, 1.8×10^{-3} s^{-1} (Z_1). Unloaded (UL) annealing with fractional softenings for various intervals.

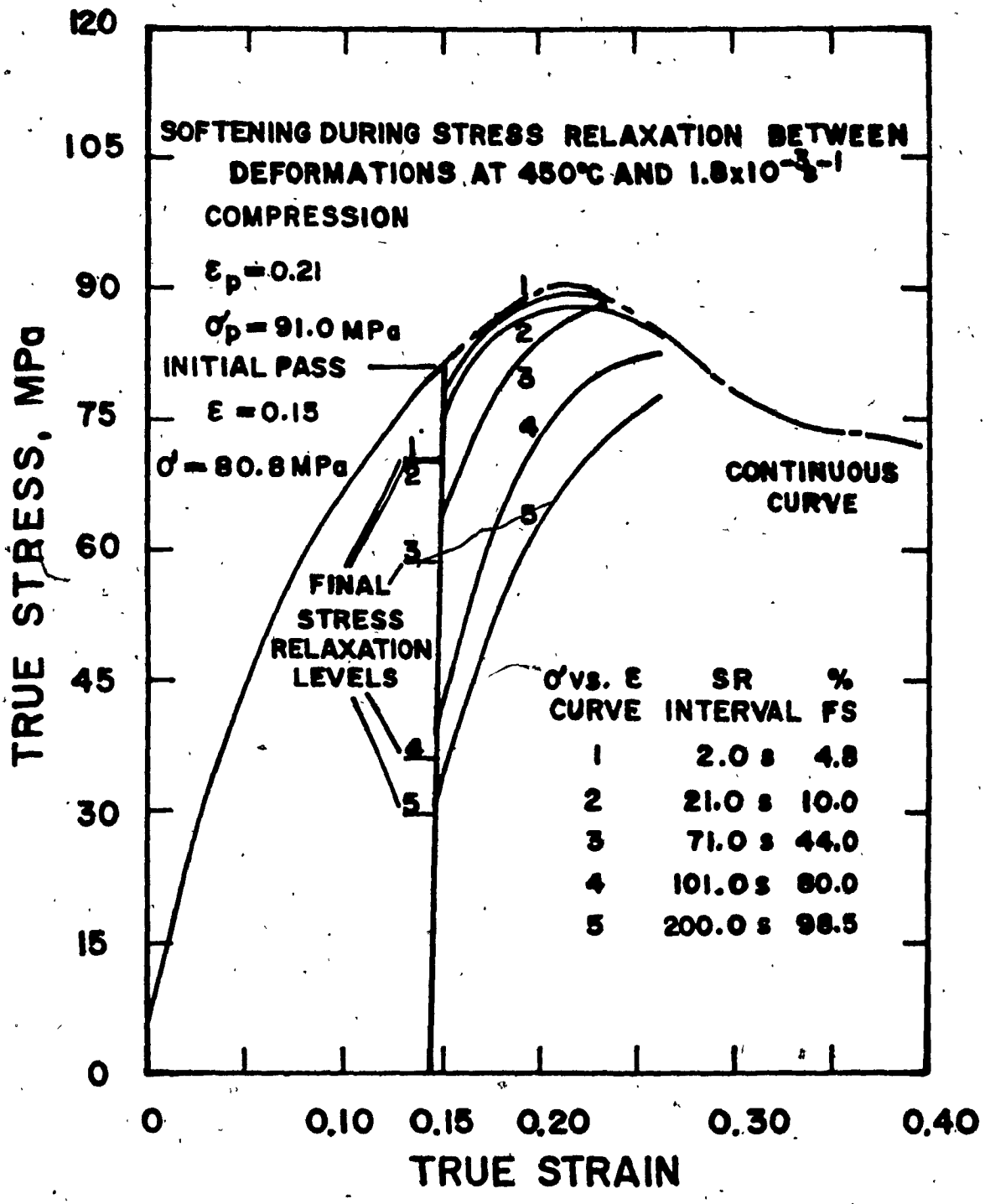

Fig. 4.1b Stress relaxation (SR) with fractional softenings and final relaxed stresses for various intervals.

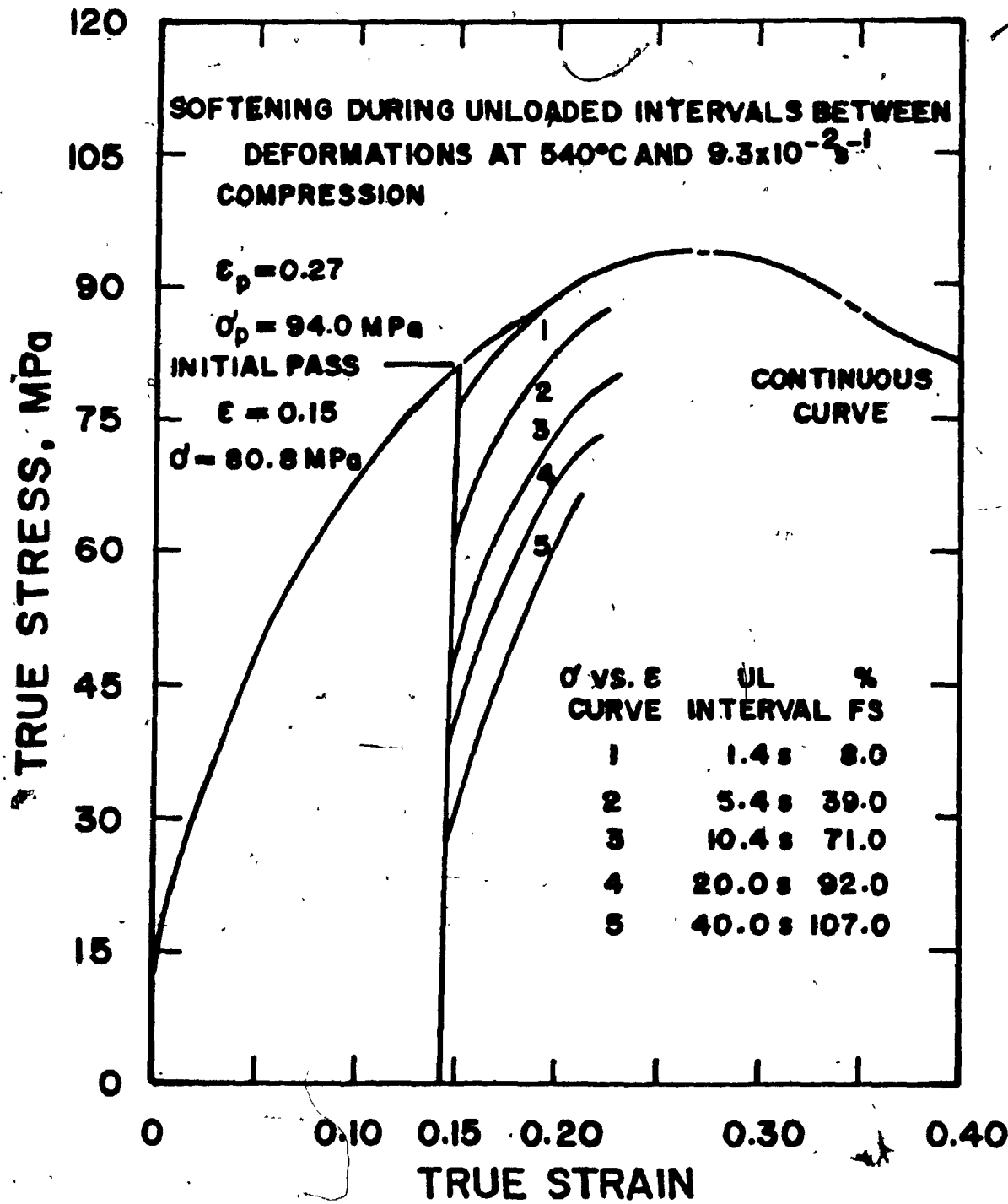

Fig. 4.2a Initial and reloading flow curves for the compression condition 540°C, 9.3×10^{-2} s^{-1} (Z_1). UL annealing with fractional softenings for various intervals.

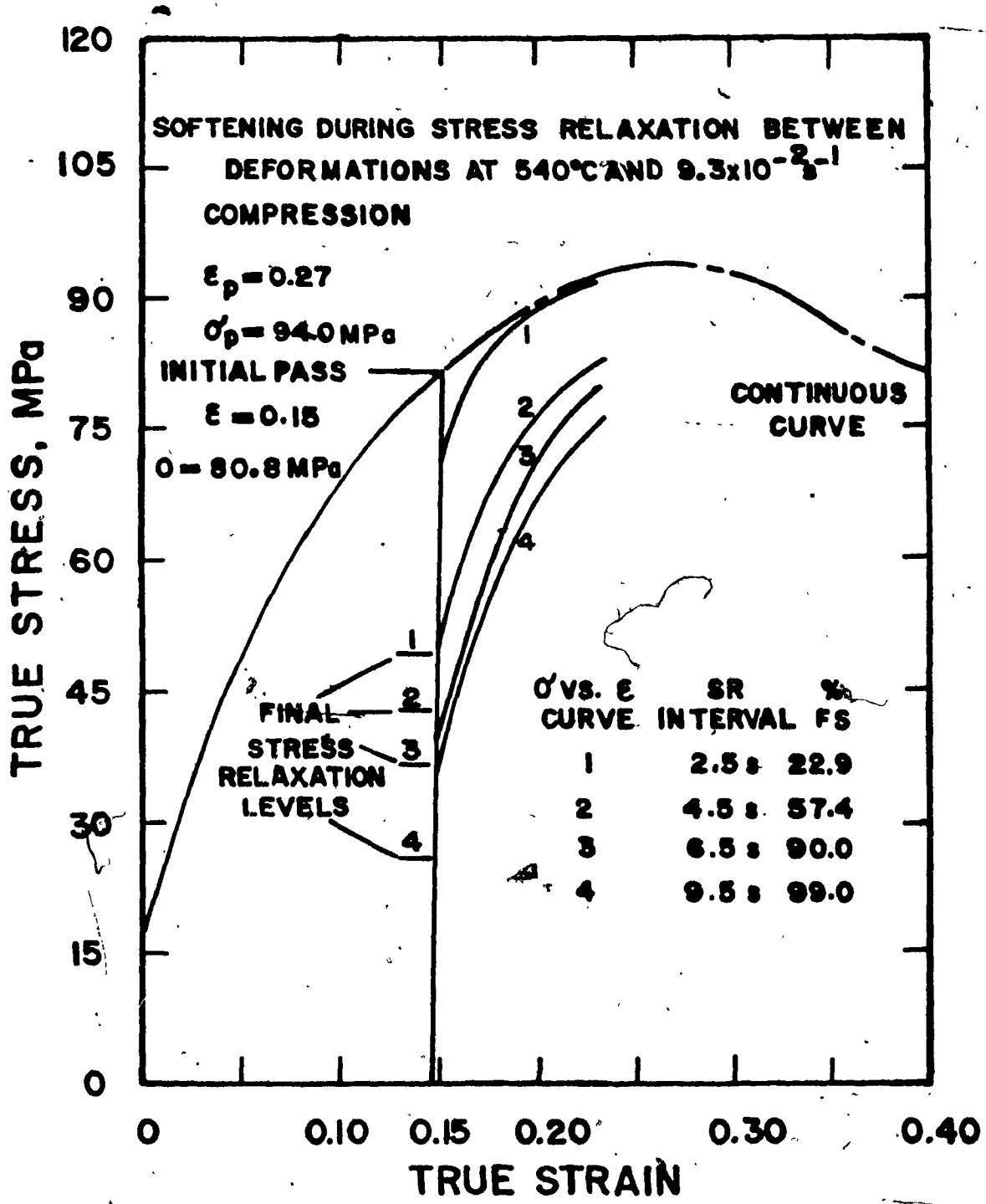

Fig. 4.2b Stress relaxation with fractional softenings and final relaxed stresses for various intervals.

carried out at the same temperature-corrected strain rate Z_1 and to the same σ_m. Figure 4.3 exhibits the compression curves and Fig 4.4 the torsion ones for the test conditions 450°C, 1.8×10^{-1} s^{-1} and thus at $100Z_1$. Figures 4.5 and 4.6 represent the torsion curves for the conditions 450°C, 1.8 s^{-1} ($1000Z_1$) and 500°C, 1.8 s^{-1} ($100Z_1$).

There are some features which are common to all the sets of reloading curves. The reloading yield stress decreases, and therefore the fractional softening increases, as the interruption time increases. After short interruption time of either unloading or stress relaxation, the reloading curve joins the continuous one. In each of the above diagrams, a combination of initial and any reloading curve represents two successive passes of a multi-pass series; moreover, the lowest reloading curve represents a sample which has fully softened after deformation and hence is similar to the primary curve.

4.1.2 Effect of Stress Relaxation

The reloading curves show that, after similar unloading or stress relaxation times, σ_r is higher in the load-free annealing tests. Contrast, for example, curve 2 of Fig. 4.1a with curve 4 of Fig. 4.1b or curves 2 of Fig. 4.2a or 4.2b. Similar observations can be made in Figures 4.3 and 4.4.

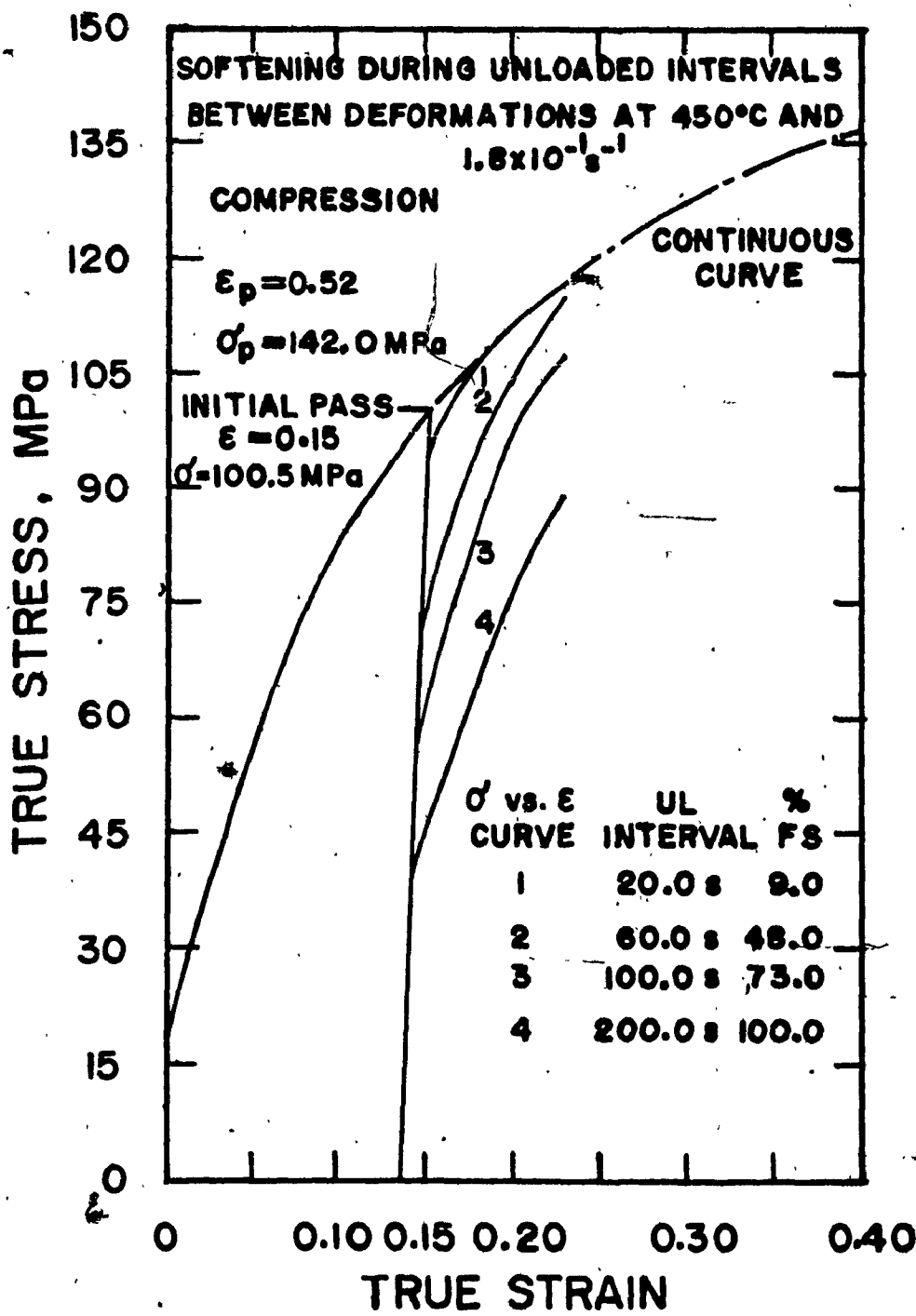

Fig. 4.3a Initial and reloading flow curves for the compression condition 450°C, 1.8×10^{-1} s^{-1} (100 Z_1). UL annealing with fractional softenings for various intervals.

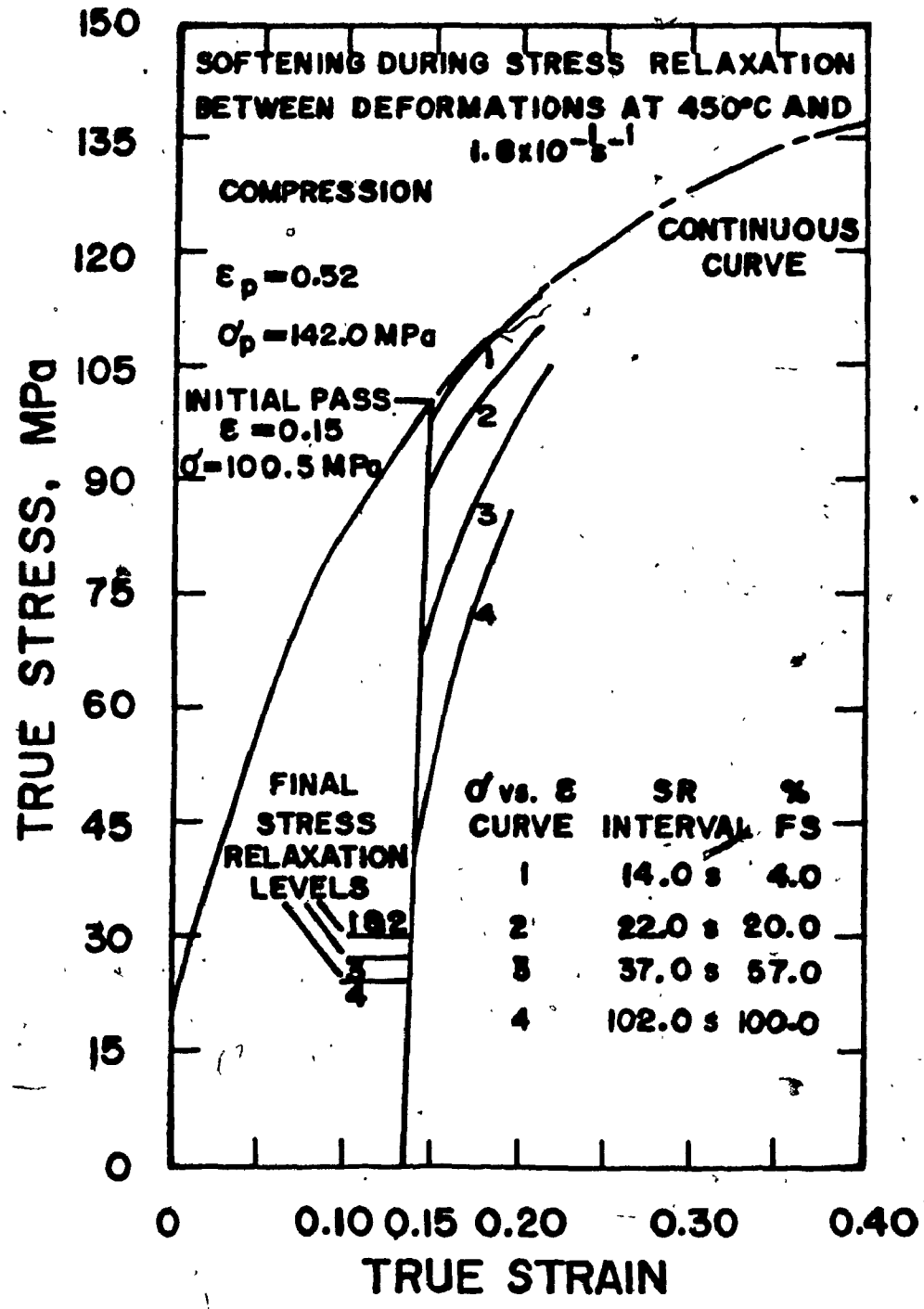

Fig. 4.3b Stress relaxation with fractional softenings and final relaxed stresses for various intervals.

4.1.3 Influence of Temperature

The effect that temperature has on the reloading yield stress after similar pre-stressing, σ_m or Z and interruption times can be observed by comparing curve 1 of Fig. 4.1a with curve 3 of Fig. 4.2a for the unloaded tests or curves 1 of Fig. 4.1b and 4.2b for stress relaxation; the drop from σ_m to σ_r is greater as the temperature is higher.

4.1.4 Effect of Strain Rate

The influence that the strain rate at constant T has on the two stage flow curves is perceived by comparing Fig. 4.1 and 4.3. The 100 fold rise in strain rate raises the initial and maximum stresses in the first pass by 25%. The reloading yield stress corresponding to 100% softening is higher in samples deformed at 1.8×10^{-1} s^{-1} (about 40 MPa) than in those strained at 1.8×10^{-3} s^{-1} (roughly 30 MPa). After similar unloading or stress relaxation times, the drop from σ_m to σ_r is greater in the samples deformed at the higher strain rate, e.g. curve 2 of Fig. 4.1a with curve 3 of Fig. 4.3a, or curves 2 of Fig. 4.1b and 4.3b.

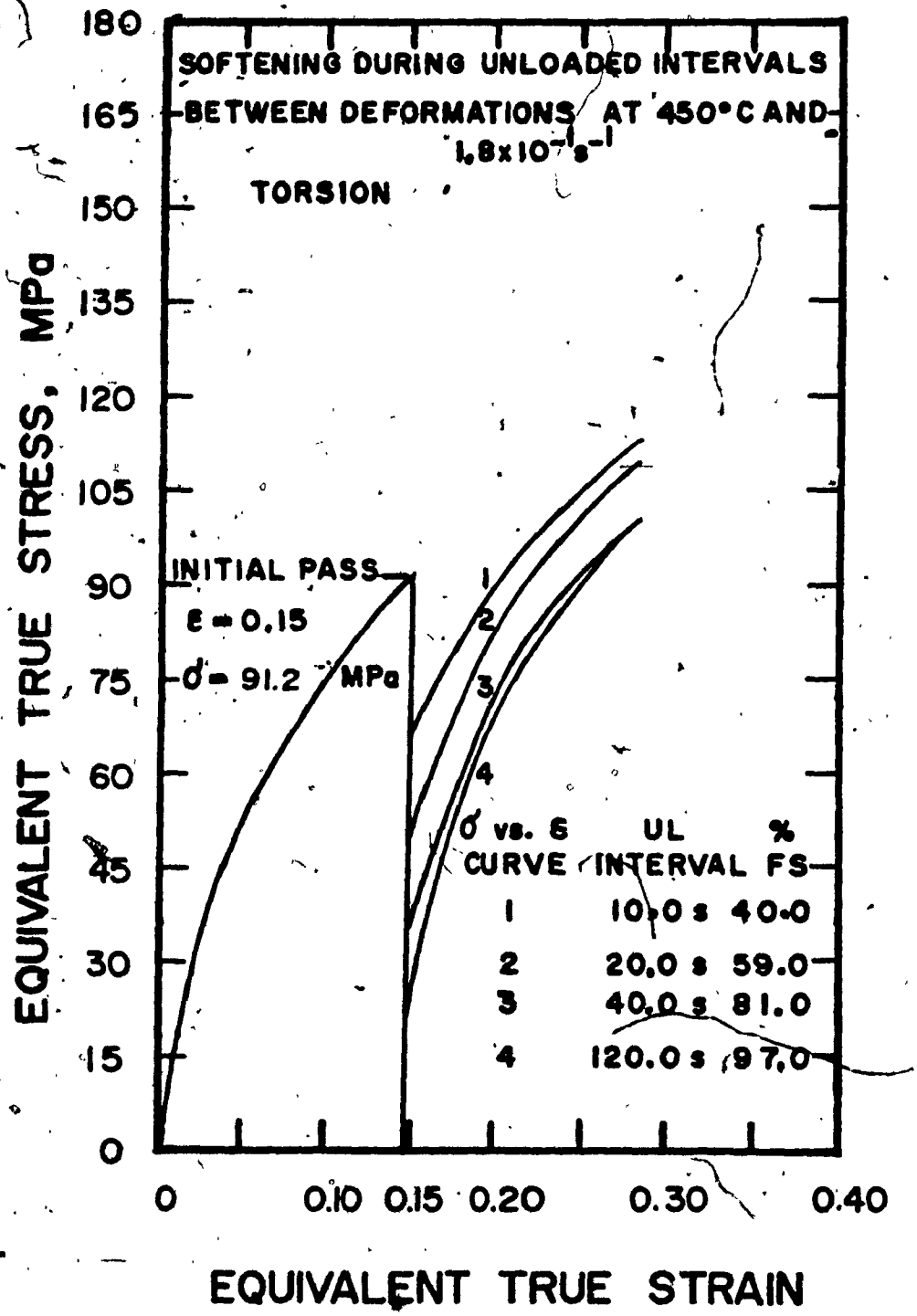

Fig. 4.4a Initial and reloading flow curves for the torsion condition 450°C, 1.8×10^{-1} s^{-1} ($100Z_1$) UL annealing with fractional softenings for various intervals.

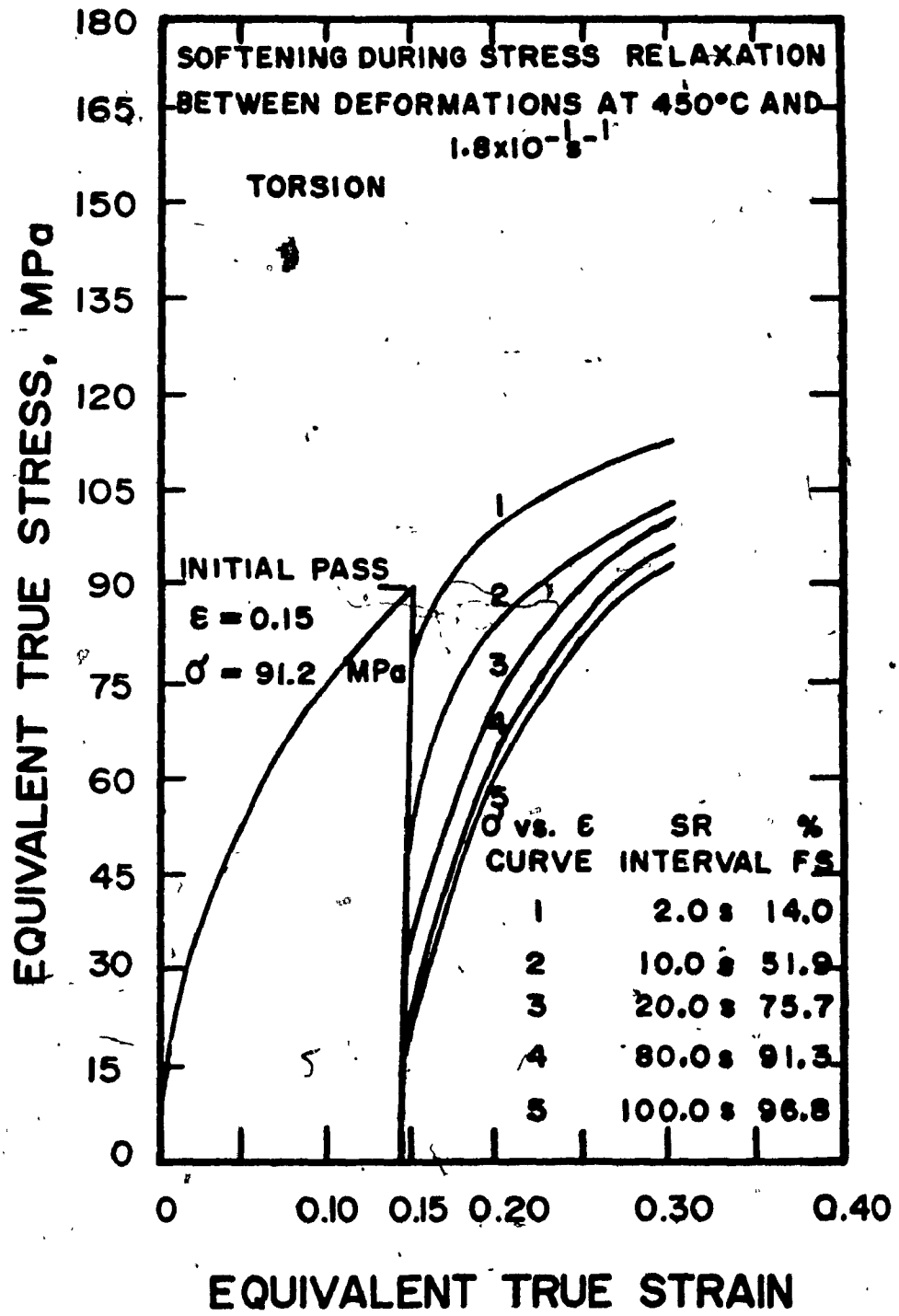

Fig. 4.4b Stress relaxation with fractional softenings and final relaxed stresses for various intervals.

4.1.5 Compression and Torsion Flow Curves

The level of the flow curve in compression is slightly higher than in torsion. For example, for the deformation conditions 450°C and 1.8×10^{-1} s^{-1}, about 100 MPa are necessary to strain the fully-annealed material to 0.15 in compression and a little more than 91 MPa are required in torsion for the same strain (Fig. 4.3 and 4.4). The likely cause of this is difference in grain size.

In the early annealing stages, the reloading yield stress in torsion drops faster than in compression as shown by Fig. 4.3a and 4.4a for the unloaded tests or by Fig. 4.3b and 4.4b for the stress relaxation ones. However, the same figures show that the yield stress on reloading falls to that of the fully annealed material in about the same time in compression and in torsion.

In torsion as in compression, the yield stress on reloading after similar unloading or stress relaxation times is higher in the load-free annealing experiments. Figures 4.4a and 4.4b confirm this statement.

4.1.6 Torsion Flow Curves at High Strain Rates

The initial and reloading flow curves after load-free annealing of samples deformed at 450°C, 1.8 s^{-1} ($1000Z_1$) and 500°C, 1.8 s^{-1} ($100Z_1$) are shown in Fig. 4.5 and

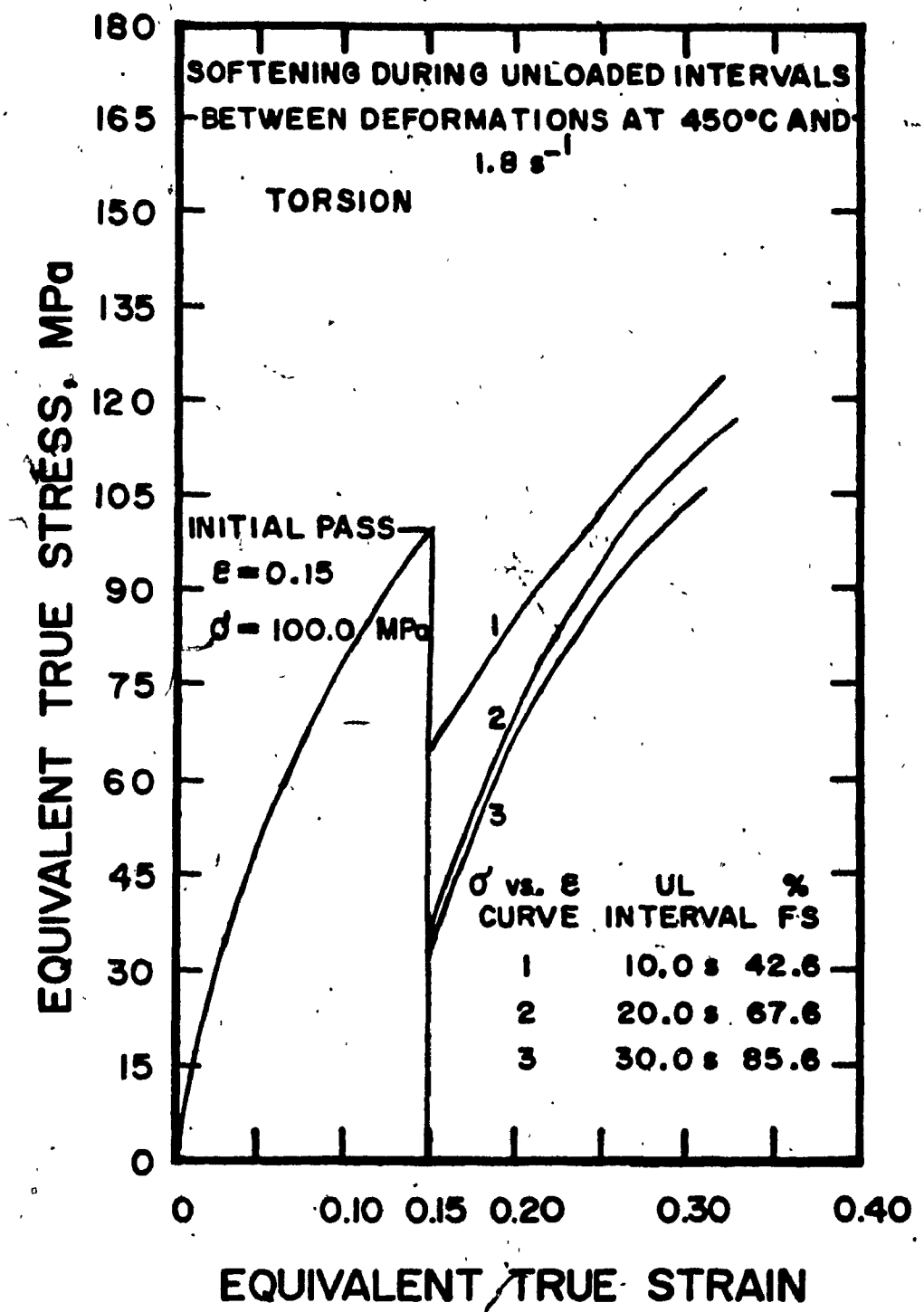

Fig. 4.5 Initial and reloading flow curves for the torsion condition 450°C, 1.8 s^{-1} (1000 Z_1). UL annealing with fractional softenings for various intervals.

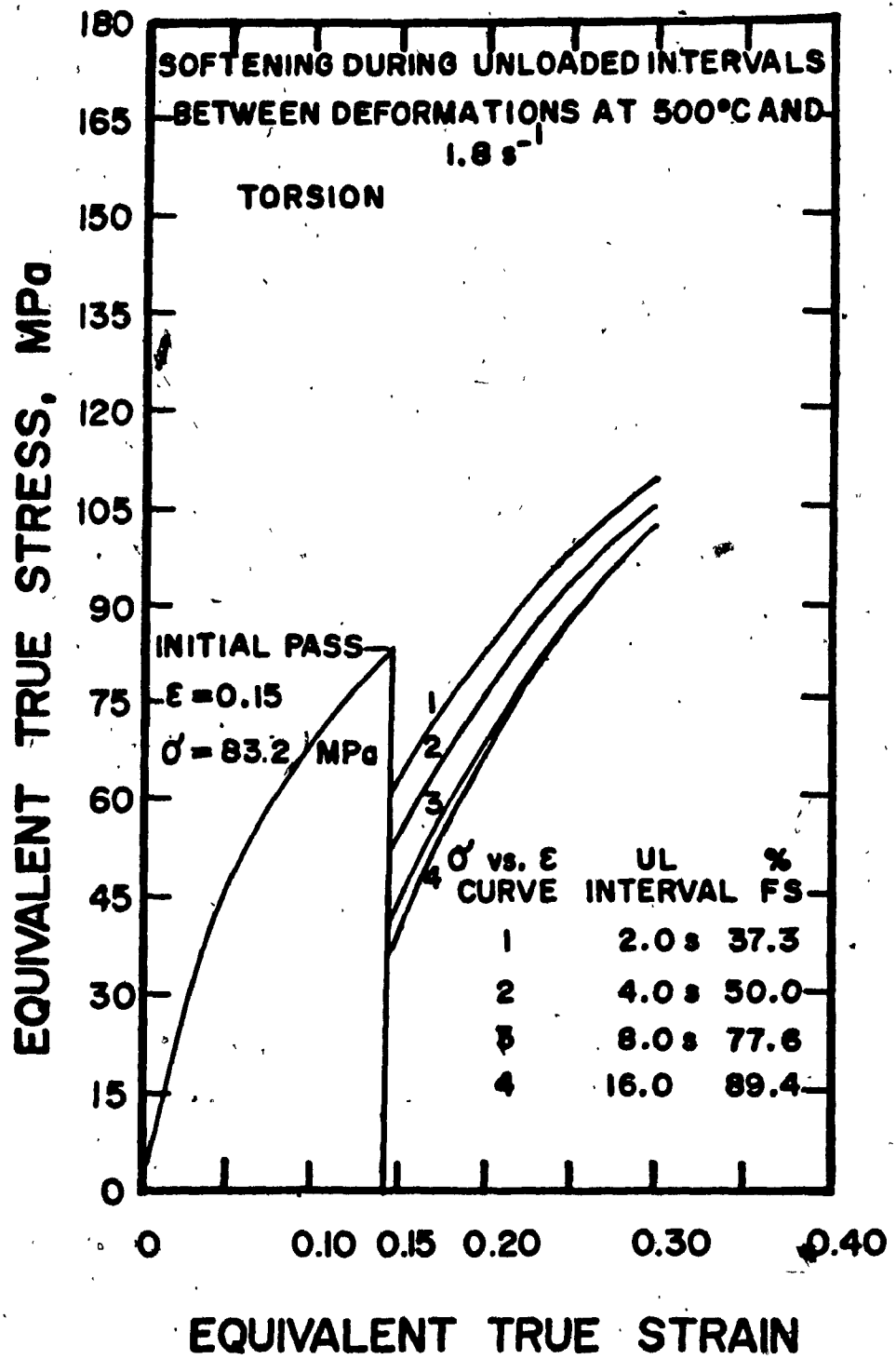

Fig. 4.6 Initial and reloading flow curves for the torsion condition 500°C, 1.8 s^{-1} (100 Z_1). UL annealing with fractional softenings for various intervals.

4.6, respectively.

An increase in the strain rate by a factor of ten raises the height of the curve 10% as shown by comparing the stress at 0.15 strain of Fig. 4.5 with that of Fig. 4.4a. The increase in $\dot{\varepsilon}$ also produces a slight acceleration in the rate of drop of the reloading yield stress: after deformation at 450°C, 1.8×10^{-1} s^{-1}, the stress falls in 40 s to the same level that is reached in 30s after deformation at 450°C, 1.8 s^{-1} as shown by curves 3 of Fig. 4.4a and 4.5.

A decrease in the time for the reloading yield stress to reach the yield stress of the fully-annealed material (Fig. 4.6) by roughly a factor of 6 is observed when the temperature is increased 50°C and the strain rate multiplied by a factor of ten with respect to the deformation and annealing conditions represented in Fig. 4.4a. These two conditions have the same Z but the flow curves differ probably because of grain size differences, which arose from the difference in the treatment between steps (Table 3.1).

4.2 Stress Relaxation Curves

Figure 4.7 shows the stress relaxation curves after a compression to 0.15 at IB 540°C, 9.3×10^{-2} s^{-1}; IA 450°C, 1.8×10^{-3}; and IIA 450 C, 1.8×10^{-1} s^{-1}. The yield stresses

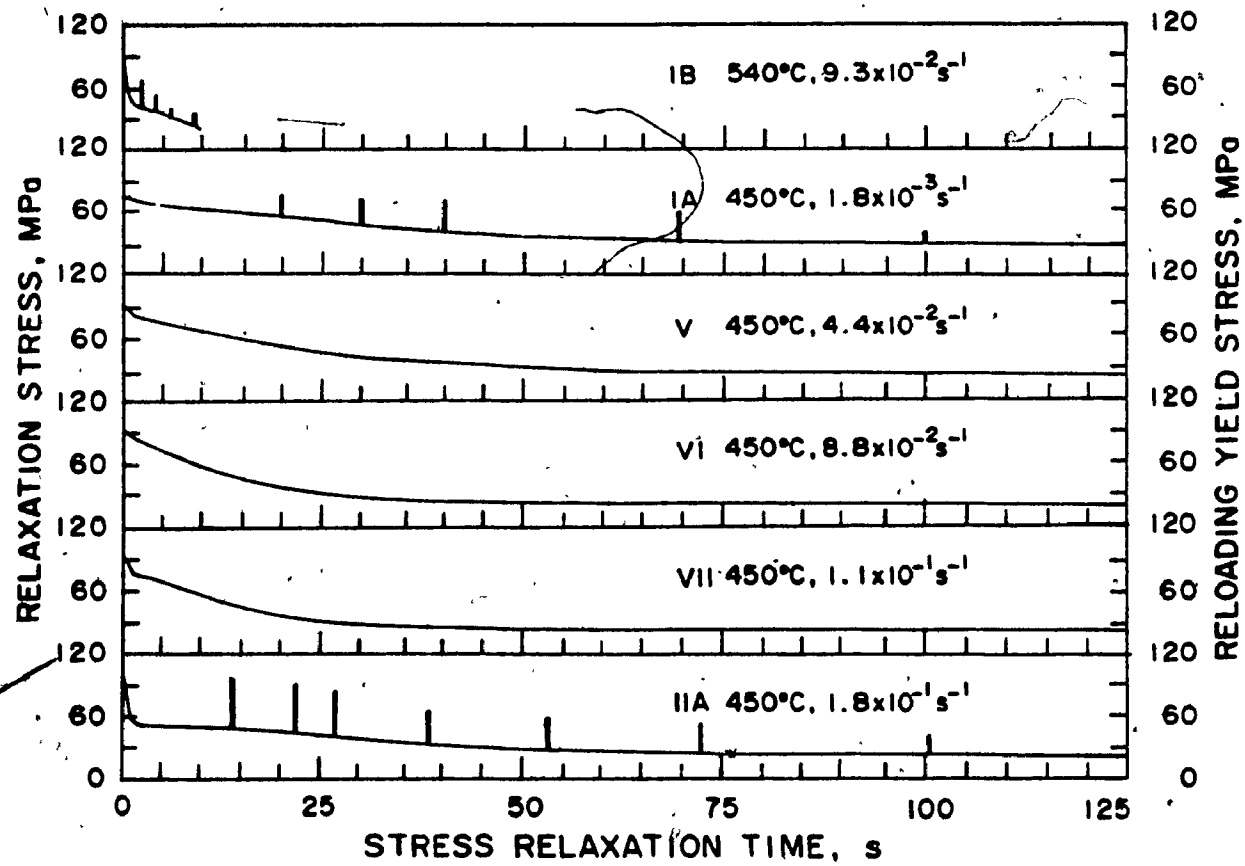

Fig. 4.7 Stress relaxation curves after a compression of 0.15. The reloading yield stress values after different relaxation times are shown on the curves (IA), (IB) and (IIA) as the tips of the vertical bars.

Table 4.1. Reloading and Relaxation Stresses

Test Conditions	t_{SR} s	σ_r MPa	σ_{SR} MPa	FS,X %	FR %
IB	2.5	70.0	41.8	22.9	64.2
$\bar{\sigma}_o$=33.4	4.5	53.6	38.6	57.4	69.5
MPa	6.5	38.1	32.2	90.0	80.0
$\bar{\sigma}_m$=80.8	9.5	33.8	24.1	99.0	93.4
IA	2	78.6	76.5	4.8	4.3
$\bar{\sigma}_o$=35.1	21	76.2	60.2	10.0	36.3
	31	73.7	52.1	15.5	50.6
$\bar{\sigma}_m$=80.8	41	70.9	46.4	21.6	60.7
	71	60.7	36.1	44.0	78.8
	101	44.2	30.1	80.0	89.4
	200	35.8	24.7	98.5	98.9
IIA	14	98.2	49.4	4.0	63.3
	22	89.0	45.4	20.0	68.2
$\bar{\sigma}_o$=43.1	27	83.6	42.4	29.5	72.0
	37	67.8	35.2	57.0	80.9
$\bar{\sigma}_m$=100.5	52	57.3	29.5	75.3	88.0
	72	47.9	24.9	91.6	93.7
	102	41.4	23.3	103.0	95.7

Table 4.2 Stresses and Stress Ratios

Set	Test Conditions °C	s^{-1}	σ_m MPa	σ_{SRST} MPa	σ_o MPa	$\frac{\sigma_m}{\sigma_{SRST}}$	t_{SRST} s	Stage 1
IB	540	9.3×10^{-2}	80.8	20.1	33.4	4.02	-	Yes
IA	450	1.8×10^{-3}	80.8	24.1	35.1	3.35	75	No
V	450	4.4×10^{-2}	86.6	23.8	37.0	3.64	70	No
VI	450	8.8×10^{-2}	90.0	22.6	39.1	3.98	65	No
VII	450	1.1×10^{-1}	92.9	21.5	40.0	4.32	50	Yes
IIA	450	1.8×10^{-1}	100.5	19.8	43.1	5.08	50	Yes

on reloading σ_r corresponding to some stress relaxation times t_{SR} are shown on these curves for comparison. Table 4.1 lists these values together with the relaxation stress σ_{SR} for the test conditions above. In Figure 4.7, V, VI and VII are stress relaxation curves for intermediate deformation rates at 450 C. Table 4.2 presents important parameters for all the relaxation tests. The curves exhibit three stages under the present test conditions: 1) linear, 2) gradually decreasing and 3) saturation relaxation.

The linear part describes a steep fall in the relaxation stress which has a duration of about 3 seconds. This stage is clearly observed only when the ratio σ_m/σ_{SRST} is large. Figure 4.8 shows how σ_m/σ_{SRST} varies with σ_m for 450°C. High ratios are obtained by a high strain rate giving a large value of σ_m or by a high relaxation temperature giving a low value of σ_{SRST}.

The second stage is different depending on whether stage 1 is absent or present. If stage 1 is absent the curve decreases at a decelerating rate to the saturation level. If stage 1 is present it starts with a transition to a plateau before decreasing into the same shape as above. In the third stage the stress remains almost constant at σ_{SRST}; however, the time to reach saturation is shorter as the ratio σ_m/σ_{SRST} increases (Table 4.2).

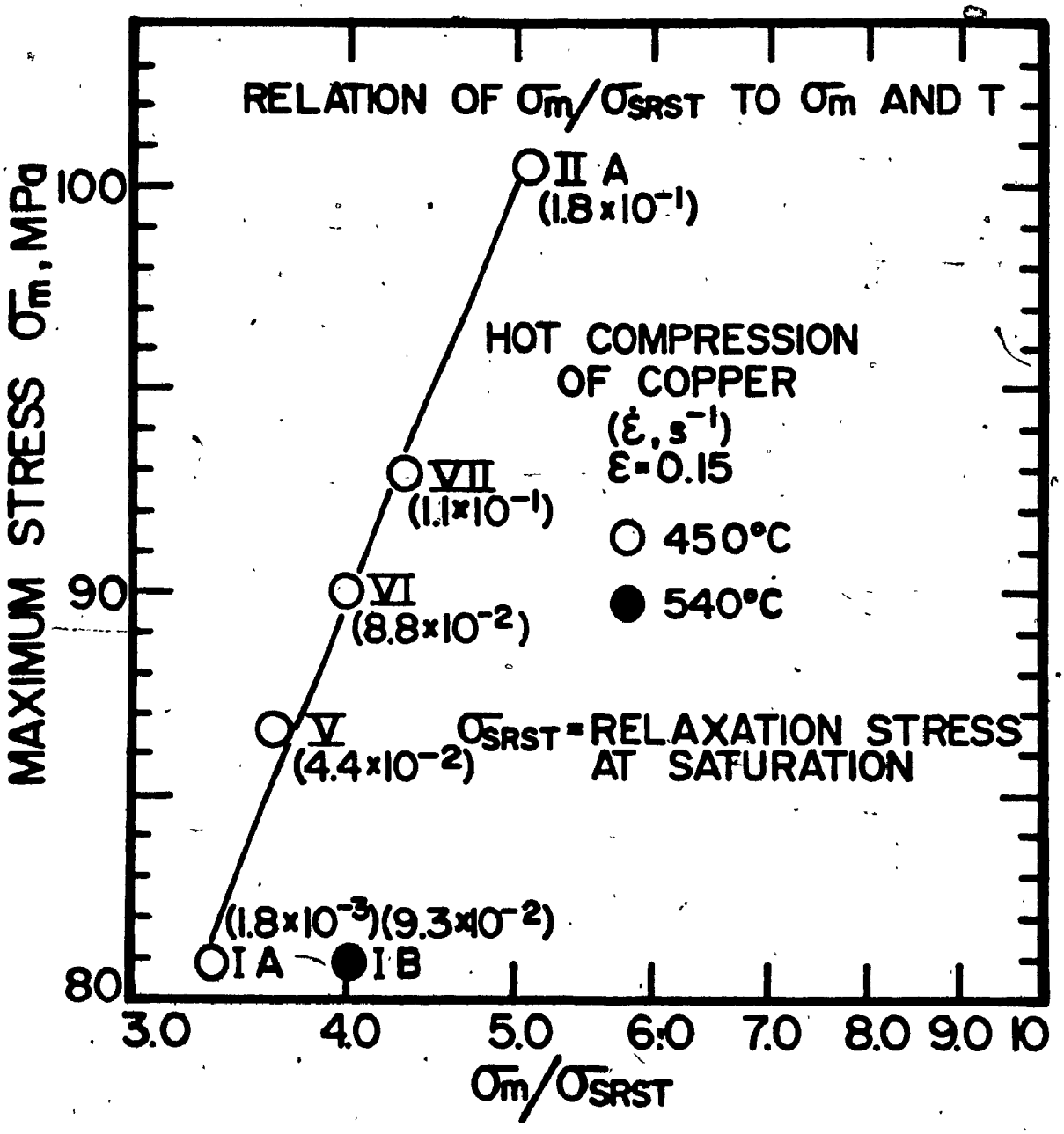

Fig. 4.8 Relationship between σ_m and σ_m / σ_{SRST}.

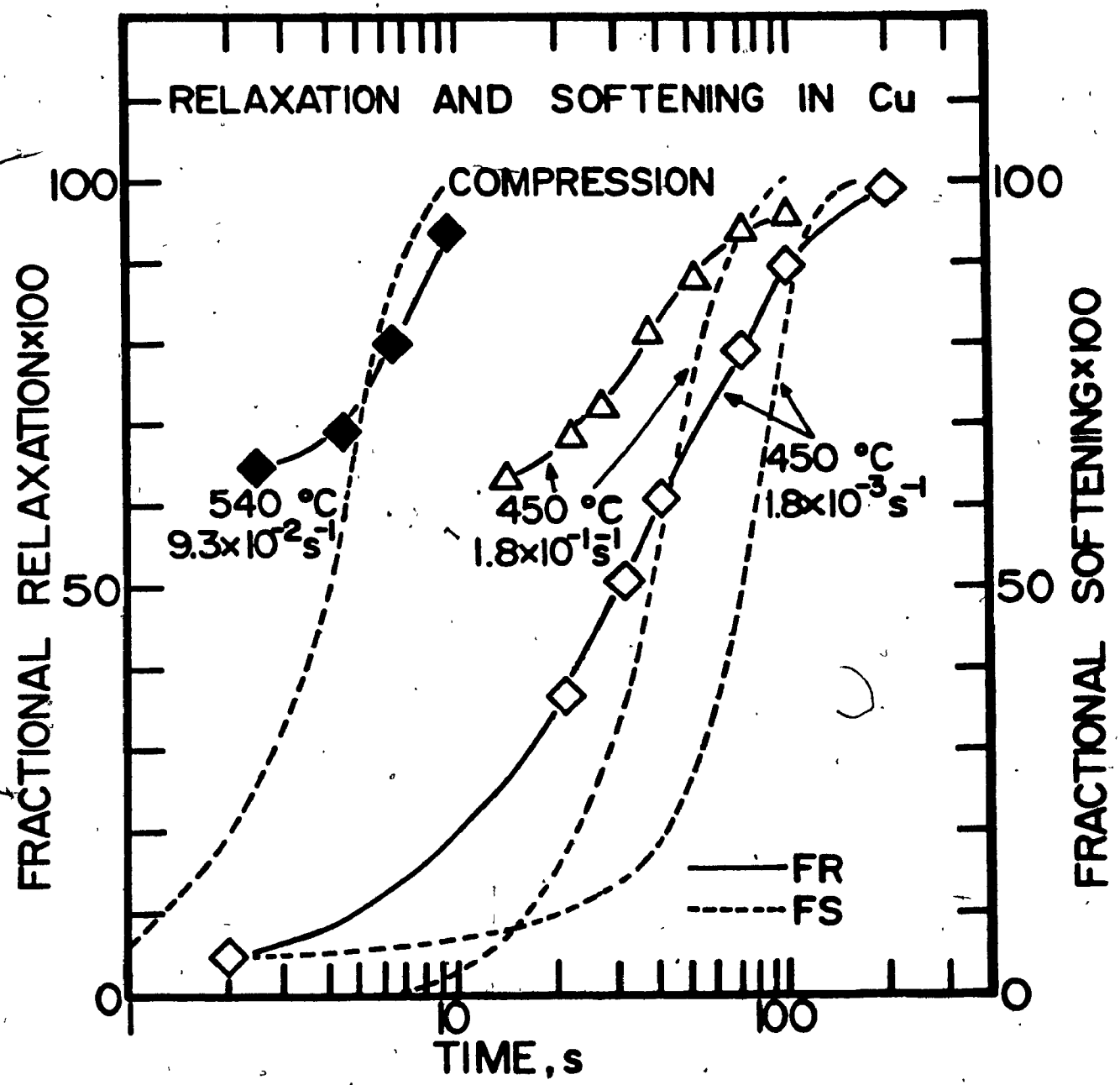

Fig. 4.9 Evolution of fractional relaxation (FR) under conditions IA,IB and IIA. Comparison with the fractional softening (FS) curves.

4.2.1 Fractional Relaxation

Figure 4.9 represents the fractional relaxation percent (as described in Section 3.4.3) vs log time curves derived from the SR curves (Fig. 4.7). The curves (outlined by symbols) show that the relaxation stress saturates at a time somewhat larger than the fractional softening.

4.3 Fractional Softening From Mechanical Testing

4.3.1 General Description

Figures 4.10 and 4.11 show the fractional softening percent (MECH, as defined in Section 3.4.2) against log time curves derived from the mechanical tests. Each graph represents groups of tests carried out at the same temperature-corrected strain rate. In Fig. 4.11, Z is a hundred times that in Fig. 4.10 and the stress is 25% higher (100 MPa vs 80 MPa). Figure 4.10 illustrates the curves constructed from compression tests. Figure 4.11 contrasts the curves obtained by compression and torsion under the same conditions but a higher σ_m in the former (100 MPa vs 91 MPa). Figure 4.12 shows the softening curves of torsion experiments accomplished at 450°C, 1.8 s^{-1} (100 MPa) and 500°C, 1.8 s^{-1} (83.2 MPa), the curve for the torsion condition 450°C, 1.8×10^{-1} s^{-1} (91.2 MPa) is also shown for comparison. The relevant stresses to plot these curves are

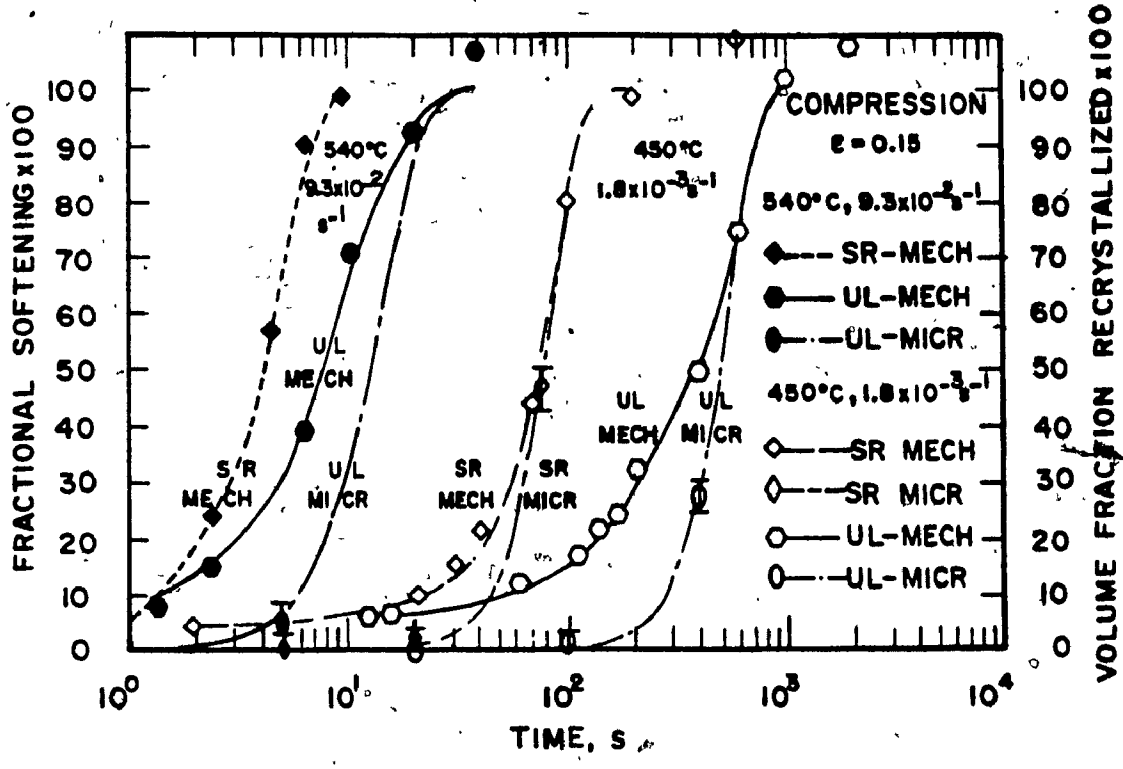

Fig. 4.10 Evolution of softening and recrystallized volume fractions with load-free and stress relaxation annealing times after compression to the same stress level (Z_1 = 1.4X1013 s^{-1}, σ_{III} = 80.8 MPa).*

*The values of FS greater than 100% are due to experimental errors.

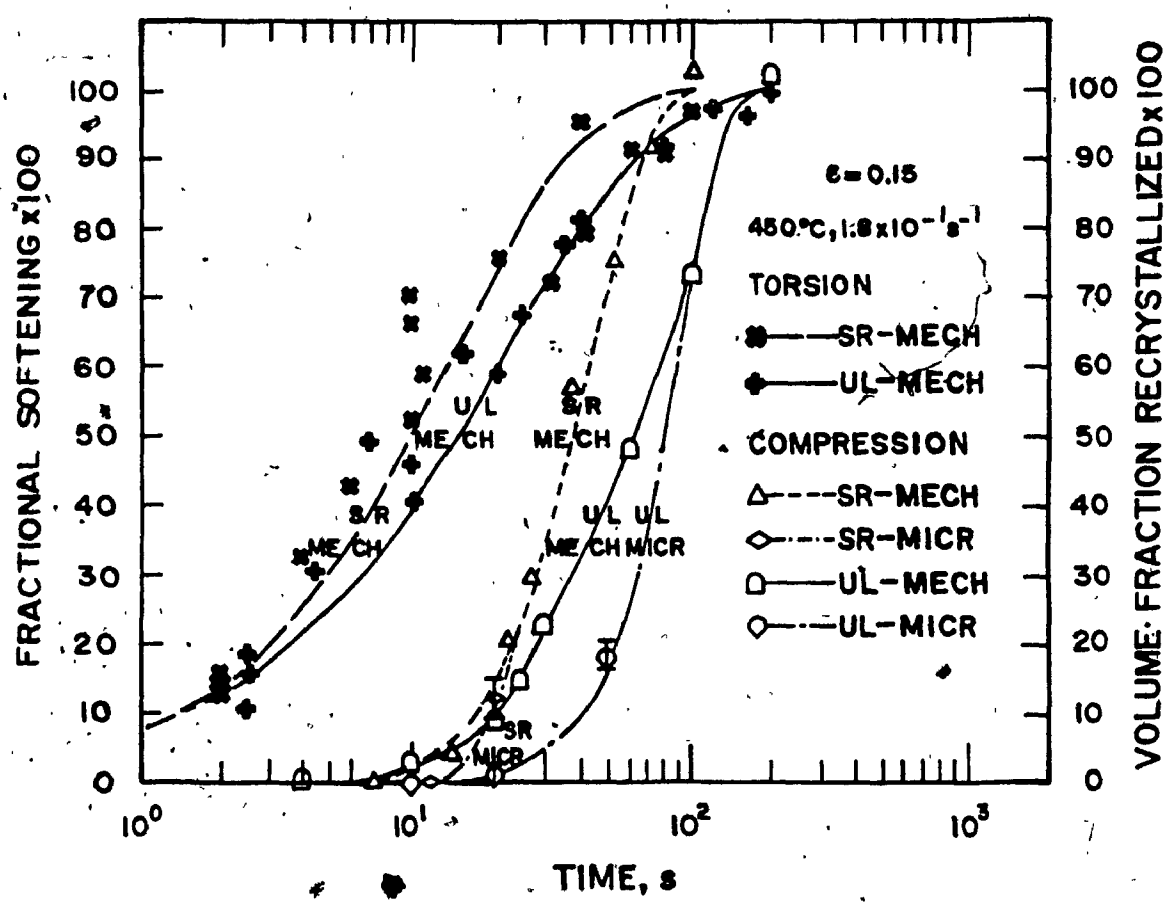

Fig. 4.11 Evolution of softening and recrystallized volume fractions with load-free and stress relaxation annealing times after compression (σ_m = 100.5 MPa), and torsion (σ_m = 91.2 MPa) at about the same stress level ($Z = 1.4 \times 10^{15}\ s^{-1} = 100\ Z_1$).

given in Appendix A.

In general the softening curves of samples compressed or subjected to torsion and annealed under both load-free (UL) and stress relaxation (SR) regimes show different amounts of softening at about 1 second of annealing (beginning of the curve) followed by a segment of gradually increasing softening, characteristic of recovery, and then by an S-shape portion, distinctive of recrystallization (Fig. 4.10). The only exceptions were the softening curves of the compression experiments at 450°C, $1.8X10^{-1}$ s^{-1} (Fig. 4.11). In these tests, σ_r was higher than σ_m after the first 6-7 seconds of annealing in the σ vs ϵ curve. It was assumed that $\sigma_r = \sigma_m$, so these points were plotted at zero fractional softening. None of the curves exhibits an intermediate plateau, indicative of recovery saturation before the recrystallization part. All the curves saturate at 100 percent of softening.

4.3.2 Stress Relaxation and Time for Full Softening

Examination of the softening curves of the compression experiments at 450°C, $1.8X10^{-3}$ s^{-1} (IA) show that the ratio of the times to reach full softening in unloaded and stress relaxation tests t_{UL}/t_{SR} is about 5 (Fig.4.10). This ratio in similar tests at 540°C, $9.3X10^{-2}$ s^{-1} (IB) is around 4 (Fig. 4.10). Compression and torsion

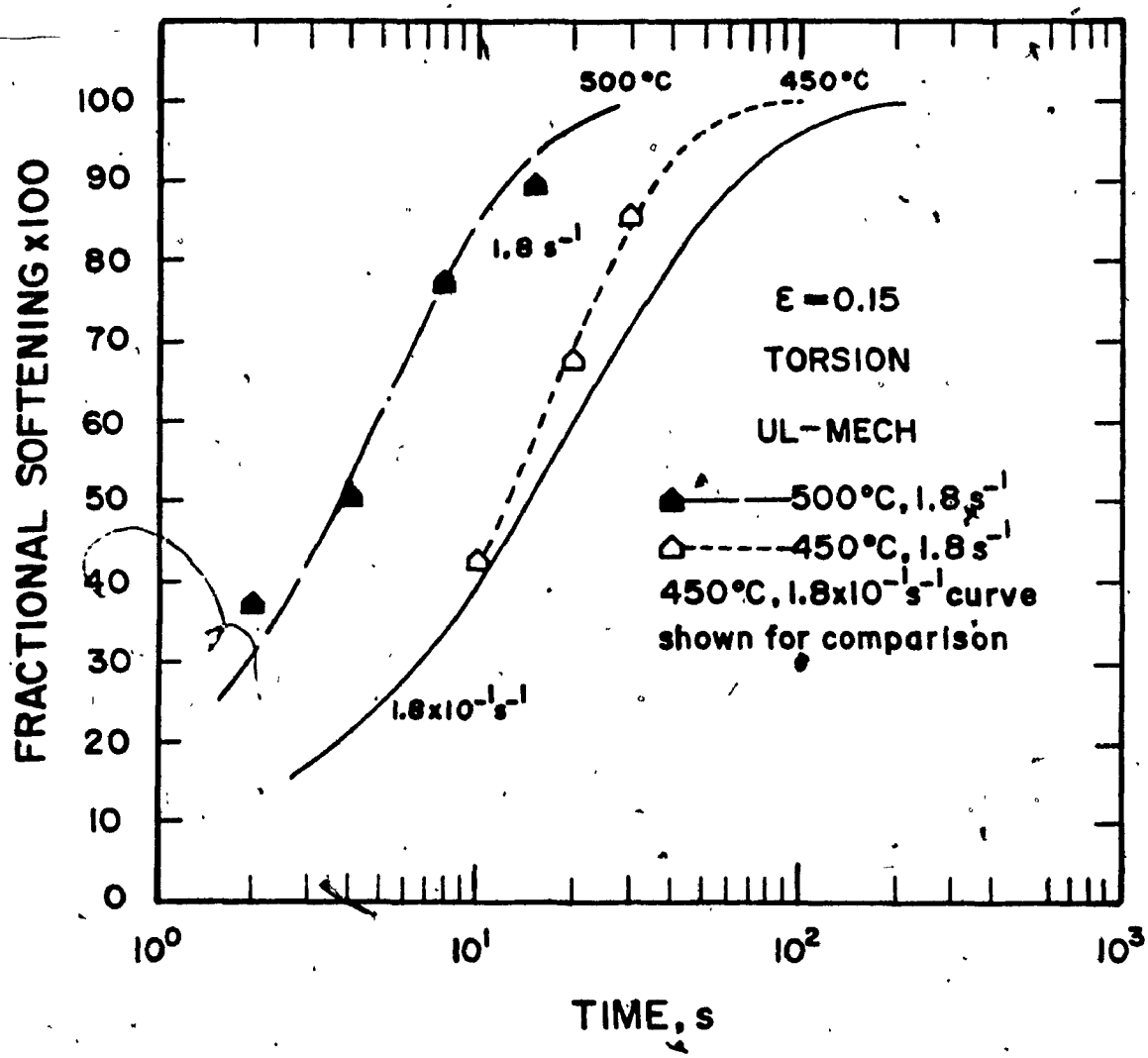

Fig. 4.12 Evolution of softening with UL annealing time after torsion at the conditions: IV 1000 Z_1, σ_m = 100.5 MPa, for 450°C, 1.8 s^{-1} and III 100 Z_1, σ_m = 83.2 MPa, for 500°C, 1.8 s^{-1}.

tests at 450°C, $1.8X10^{-1}$ s^{-1} (IIA) show a ratio of 2 (Fig. 4.11). Thus, stress relaxation increases the rate of softening under all the experimental conditions used in this work. Table 4.3 lists the times for different levels of softening.

4.3.3 Effect of Temperature on the Time for Full Softening

The effect that temperature has on the time to reach full softening can be assessed for compression from curves which correspond to samples deformed to the same stress level (same σ_m and Z) as in the case of the curves compressed at 450°C, $1.8X10^{-3}$ s^{-1} and 540°C, $9.3X10^{-2}$ s^{-1} (Fig. 4.10). Unloaded samples annealed at 540°C fully soften 25 times faster than those at 450°C. When stress relaxation specimens are compared, those annealed at 540°C require a time only 1/20 that of their analogues at 450°C (Fig. 4.10). Both unloaded and stress relaxation experiments at 450°C render a softening curve with a well defined recovery stage. Such evolution is not observed in the curves of the UL and SR tests at 540°C, because static recrystallization proceeded very quickly (Fig. 4.10). At 540°C, the time to 10% softening is the same for both the UL and SR holding conditions; at shorter times the SR softens more slowly. This behavior at 540°C is linked to the presence of noticeable first and second stages in the stress relaxation curves (Fig. 4.7).

Table 4.3. Times and Time Ratios for Different Fractional Softenings (X)

t_X	UL t (s)	SR t (s)	$\frac{t_{UL}}{t_{SR}}$	UL t_1/t	SR t_1/t
IA = 1, T_1 = 450°C_1 $\dot{\varepsilon}$ = 1.8×10^{-3} s^{-1}					
t_{10}	54	21	2.57		
t_{20}	135	43	2.93		
t_{50}	390	72	5.42		
t_{100}	1000	180	5.55		
IB=2, T_2=540°C, $\dot{\varepsilon}_2$=$9.3 \times 10^{-2} s^{-1}$, T_1-T_2=90, $\dot{\varepsilon}_2/\dot{\varepsilon}_1$=50, Z_2/Z_1=1				t_1/t_2	t_1/t_2
t_{20}	3.0	2.15	1.4	45	20
t_{50}	7.8	4.2	1.6	50	17.1
t_{100}	35.0	10.0	3.5	28.5	18.0
IIA=3, T_3=450°C, $\dot{\varepsilon}_3$=1.8×10^{-1} s^{-1}, T_1-T_3=0, $\dot{\varepsilon}_3/\dot{\varepsilon}_1$=$Z_3/Z_1$=100				t_1/t_3	t_1/t_3
t_{10}	20	17	1.2	2.7	1.2
t_{20}	29	23	1.3	4.7	1.9
t_{50}	63	38	1.7	6.2	1.9
t_{100}	180	105	1.7	5.6	1.7

Observations IA and IB (Section 4.3.2) that the ratio t_{UL}/t_{SR} decreases from 5 to 4 show that in samples compressed to the same level of stress (same Z), the stress relaxation accelerating effect on the rate of softening decreases as the annealing temperature increases.

4.3.4 Effect of Strain Rate on the Time for Full Softening

The effect that strain rate has on the time to complete softening is shown in compression by the experiments at 450°C, $1.8X10^{-3}$ s^{-1} (Fig. 4.10) and by those at 450°C, $1.8X10^{-1}$ s^{-1} (Fig. 4.11). The stress level σ_m was 100.5 MPa at the higher strain rate as compared to 80.8 MPa at the lower one. UL samples tested at $1.8X10^{-1}$ s^{-1} full soften 5 times faster than the equivalent ones compressed at $1.8X10^{-3}$ s^{-1}. On the other hand, the time for full softening of SR specimens was shortened one half when $1.8X10^{-1}$ s^{-1} instead of $1.8X10^{-3}$ s^{-1} was used. Samples compressed at $1.8X10^{-1}$ s^{-1} did not show evidence of softening after the first 6 to 7 seconds of UL or SR annealing (Fig. 4.11), but those compressed at $1.8X10^{-3}$ s^{-1} did after only 1 second of UL or SR annealing (Fig. 4.10). The change in behavior in stress relaxation upon increasing $\dot{\varepsilon}$ and hence the stress (σ_m/σ_{SRST} rises from 3.35 to 5.08) is similar to what happens on raising temperature which agrees with the change in shape of the SR curve.

From cases IA and IIA (Section 4.3.2), the changes in the ratio t_{UL}/t_{SR} from 5 to 2 illustrates that in compression a strain rate increase diminishes the effect of stress relaxation.

4.3.5 Compression and Torsion Softening Curves

The fractional softening vs log time curves of samples deformed at 450°C, 1.8×10^{-1} s^{-1} in torsion and compression (Fig. 4.11) reveal two facts: i) after a rapid beginning, the rate of softening in the former mode of test slows down so that the overall restoration process is completed at about the same time as in the latter mode (observation IIA, Section 4.3.2); ii) the unloaded and stress relaxation softening curves are similar for a given mode of deformation but are of different form after compression and torsion. This displacement of the torsion softening curve to shorter times takes place even though the maximum stress is lower (σ_m = 91.2 compared to 100.5 MPa).

4.3.6 Torsion Softening Curves at High Strain Rates

An increase in the strain rate by a factor of ten which raised σ_m from 91.2 to 100 MPa accelerates the completion of full softening by a factor of 2 as shown by the softening curves for the deformation conditions 450°C, 1.8×10^{-1} s^{-1} and 450°C, 1.8 s^{-1} (Fig. 4.11 and 4.12). In accordance with this effect a 100 fold increase would speed

Table 4.4. Softening and Recrystallization Parameters

MECH: Softening Measured Mechanically

Set	T °C	$\dot{\varepsilon}$ s^{-1}	Annealing Condition	p	$p_{SR}-p_{UL}$	k	$k_{SR}-k_{UL}$	Fig. no.
	Compression							
IA	450	1.8×10^{-3}	UL	1.2	0.4	6.5×10^{-4}	-3.3×10^{-5}	4.13
Z_1	450	1.8×10^{-3}	SR	1.6		6.2×10^{-4}		
IB	540	9.3×10^{-2}	UL	1.5	0.7	3.9×10^{-2}	-7×10^{-3}	
Z_1	540	9.3×10^{-2}	SR	2.2		3.2×10^{-2}		
	Compression							
IIA	450	1.8×10^{-1}	UL	1.6	0.5	8.1×10^{-4}	-6×10^{-5}	4.14
$100Z_1$	450	1.8×10^{-1}	SR	2.1		7.5×10^{-4}		
IIB	Torsion							
$100Z_1$	450	1.8×10^{-1}	UL	0.8	0.2	8.3×10^{-2}	-6×10^{-3}	4.14
	450	1.8×10^{-1}	SR	1.0		7.7×10^{-2}		
III	Torsion							
$100Z_1$	500	1.8	UL	0.9		2.3×10^{-1}		
IV	Torsion							4.15
$1000Z_1$	450	1.8	UL	1.0		6.0×10^{-1}		

MICR: Recrystallization Measured Microscopically

IA	450	1.8×10^{-3}	UL	3.2	0	1.7×10^{-9}	6.3×10^{-7}	4.13
IA	450	1.8×10^{-3}	SR	3.2		6.3×10^{-7}		
IB	540	9.3×10^{-2}	UL	2.4	-	1.5×10^{-3}		
IB	540	9.3×10^{-2}	SR	-		-		
IIA	450	1.8×10^{-1}	UL	2.8	-0.7	3.2×10^{-6}	7.5×10^{-4}	4.14
IIA	450	1.8×10^{-1}	SR	2.1		7.5×10^{-4}		

up the rate by a factor of 4 similar to that of 5 seen in compression. When the temperature is increased by 50°C, in comparison to the same strain rate the time required to complete full softening is only one third and in comparison to one tenth the strain rate is only one sixth (Fig. 4.4a). This latter result is roughly in agreement with the factor of one twenty fifth for an increase of 90°C in compression. The more rapid softening at 500°C takes place even though σ_m (83.2 MPa) is lower than at 450°C, 1.8 s^{-1} (100MPa) or at 450°C, 1.8×10^{-1} s^{-1} (91.2 MPa).

4.3.7 Softening Kinetics

Table 4.4 and Figures 4.13 to 4.15 show the softening kinetic parameters (MECH) for all the test conditions. The magnitude of p does not vary in any pattern with either temperature or strain rate, however, it is about 2 in compression while only 1 in torsion. Stress relaxation leads to a higher value of p (Eqn 2.27). The difference between the p values for UL and SR is more, the higher is the annealing temperature (IB:0.7 vs IA:0.4 (Z_1)) or the strain rate (IIA:0.5 ($100Z_1$) vs IA:0.4 (Z_1)). In torsion, p difference is smaller than in compression (IIB:0.2 vs IIA:0.5 ($100Z_1$)).

Stress relaxation rendered a slightly lower value of k for low Z values (IA SR vs IA UL; IB SR vs IB UL (Z_1)),

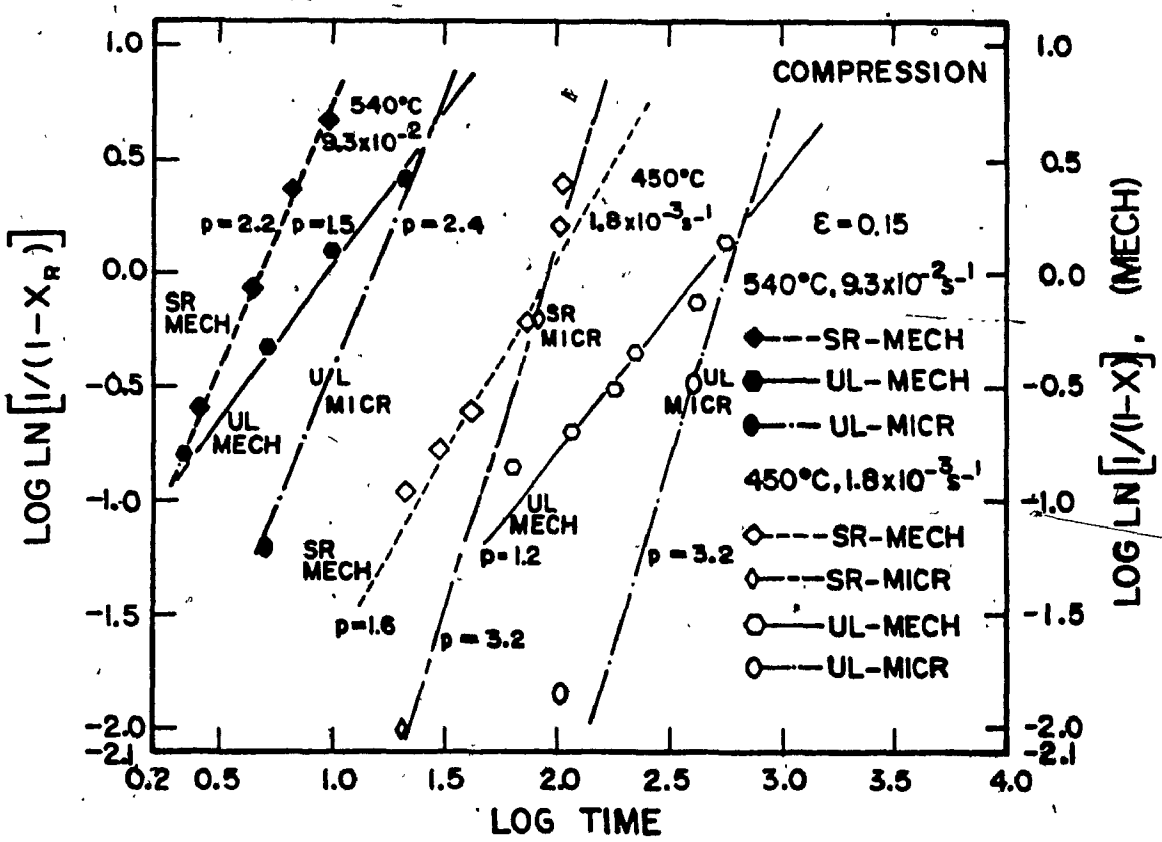

Fig. 4.13 Softening (MECH) and recrystallization (MICR) kinetics according to Avrami relationship (eqn. (2.27)) under conditions IA UL and SR, and IB UL and SR (Z_1) (Table 4.4).

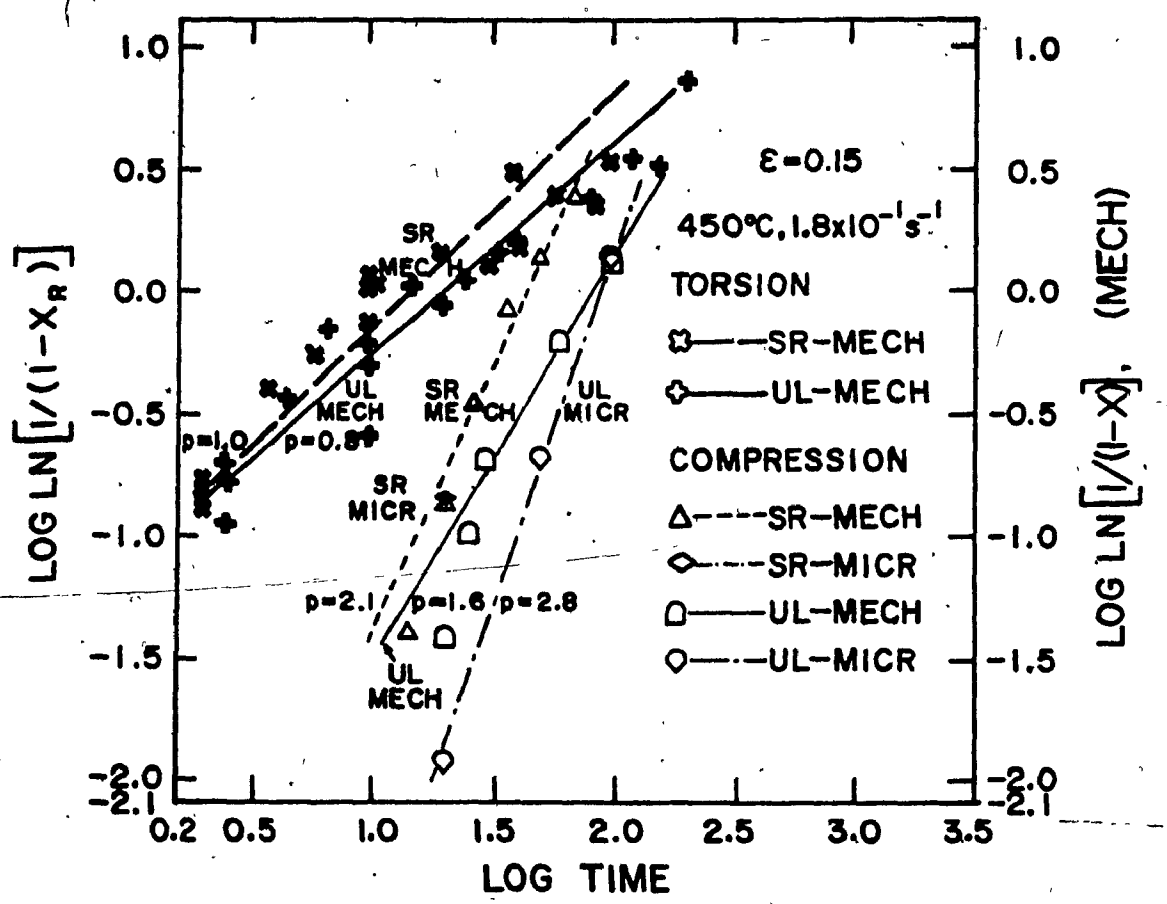

Fig. 4.14 Softening kinetics (MECH) according to Avrami relationship (eqn. (2.27)) under conditions IIA UL and SR, and IIB UL and SR; recrystalization kinetics (MICR) for IIA UL and SR (100 Z_1) (Table 4.4).

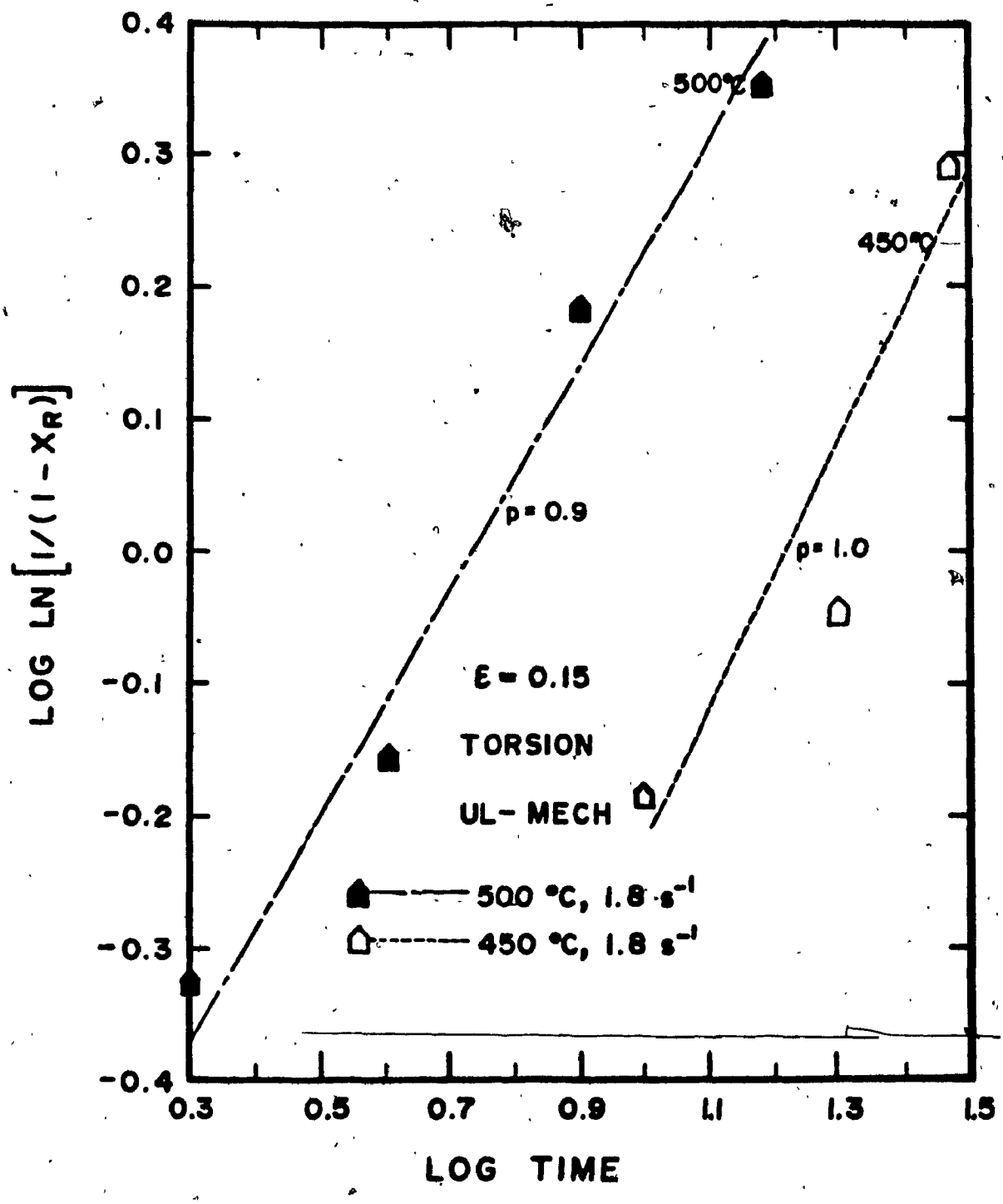

Fig. 4.15 Softening kinetics according to Avrami relationship (eqn. (2.27)) under conditions III (100 Z_1) and IV (1000 Z_1).

and likewise for high Z (IIA SR vs IIA UL; IIB SR vs IIB UL ($100Z_1$)). However, k increased with either temperature (IIA vs IB; IIB vs III ($100Z_1$)), or strain rate (IA (Z_1) vs IIA ($100Z_1$); IIB ($100Z_1$) vs IV ($1000Z_1$)) and was higher in torsion than in compression (IIA vs IIB).

The combined effect of different p and k for SR MECH and UL MECH led to rather separated curves in condition IA (Fig. 4.10). The reduced difference in p with increases in temperature (IB) (Fig. 4.10) or strain rate (IIA) (Fig. 4.11) diminished the separation between the pairs of curves.

4.4 Recrystallization

4.4.1. Volume Fraction Recrystallized

The volume fraction recrystallized data and their 95 confidence limits for various annealing times are given in Table 4.5 and represented in Figures 4.10 and 4.11 (MICR). The volume fraction recrystallized vs log time curves consisted of an incubation time segment followed by an S-shape portion (as in classic static recrystallization after cold working). The incubation time was shorter for both higher strain rate and higher temperature especially for samples deformed in condition SR IB (540°C). The effects of stress relaxation, temperature, strain rate and deformation mode on the recrystallization rate were similar to those pointed out for the fractional softening rate in

Table 4.5. Volume Fraction Recrystallized Values and 95% Confidence Limits

Set	Compression Conditions	Annealing Condition	Time s	$X_R^{+}_{-}$ 95% CL	Magnification
IA	450°C, 1.8×10^{-3} s^{-1}	UL	20	$0.000^{+0.000}_{-0.000}$	---
			100	$0.0145^{+0.007}_{-0.000}$	X50
			400	$0.273^{+0.020}_{-0.020}$	X150
		SR	5	$0.000^{+0.000}_{-0.000}$	X50
			20	$0.009^{+0.005}_{-0.000}$	X50
			80	$0.471^{+0.030}_{-0.030}$	X150
IB	540°C, 9.3×10^{-2} s^{-1}	UL	5	$0.044^{+0.018}_{-0.000}$	X50
IIA	450°C, 1.8×10^{-1} s^{-1}	UL	10	$0.000^{+0.000}_{-0.000}$	---
			20	$0.010^{+0.006}_{-0.000}$	X50
			50	$0.183^{+0.001}_{-0.000}$	X150
		SR	12	$0.000^{+0.000}_{-0.000}$	---
			20	$0.121^{+0.020}_{-0.020}$	X150

X50 and X150 magnifications were used to measure low and high values of X_R respectively.

Section 4.3.

4.4.2 Comparision of Softening and Recrystallization Kinetics

The microscopic reaction curves were always delayed compared to the mechanical ones. This was greater at shorter times and became negligible at longer times. The delay was greatest for 450°C, $1.8X10^{-3}$ s^{-1} (IA) and decreased as temperature (IB, Z constant) and strain rate (IIA, T constant) increased. In addition it was found that the difference between the MICR and MECH curves was much less for SR than for the UL ones. At a higher strain rate (IIA, T constant) the SR curves almost completely coincided (Fig. 4.14). While the very high rate for softening and recrystallization in the condition IB (540°C) prevented such comparison, it is likely that both curves would have coincided. Thus, stress relaxation brings together the MECH and MICR curves, such effect being more pronounced with increases in annealing temperature and strain rate.

4.4.3 Recrystallization Kinetics

Table 4.4 and Figures 4.13 and 4.14 show the volume fraction recrystallized parameters (MICR) for various compression conditions. The values of p were generally higher than for mechanical softening, particularly for unloaded holding, consistent with the shorter time span (Figures 4.10 and 4.11). The magnitude of k was also lower

consistent with the greater delay for initiation. The variation of p (MICR) with temperature and strain rate was similar to that of p (MECH) but it was not smaller for UL than for SR. On the other hand unlike softening, stress relaxation increased k (IA UL vs IA SR (Z_1); IIA UL vs II SR ($100Z_1$)) as does temperature (IA vs IB (UL)) and strain rate (IA vs IIA (UL)). On the whole as for fractional softening, the separation between the SR MICR and UL MICR lines diminished either with increases in temperature (IA vs IB) or strain rate (IA vs IIA).

4.4.4 Metallography

4.4.4.1 Hot worked and Partially Recrystallized Microstructures

The deformation experiments for which metallographic specimens were prepared are shown in Figure 4.16. In addition the initial full recrystallized microstructure before testing appears in Figure 4.17. Figures 4.18 to 4.31 show hot worked and partially recrystallized structures of compressed specimens at a magnification of 75X.

Tests at 450°C, 1.8×10^{-3} s^{-1} (IA). Figure 4.18 shows the immediately quenched structure, Figures 4.19 and 4.20 those after SR for 5 and UL annealing for 20x, respectively. The crystalline grains have a rough etched

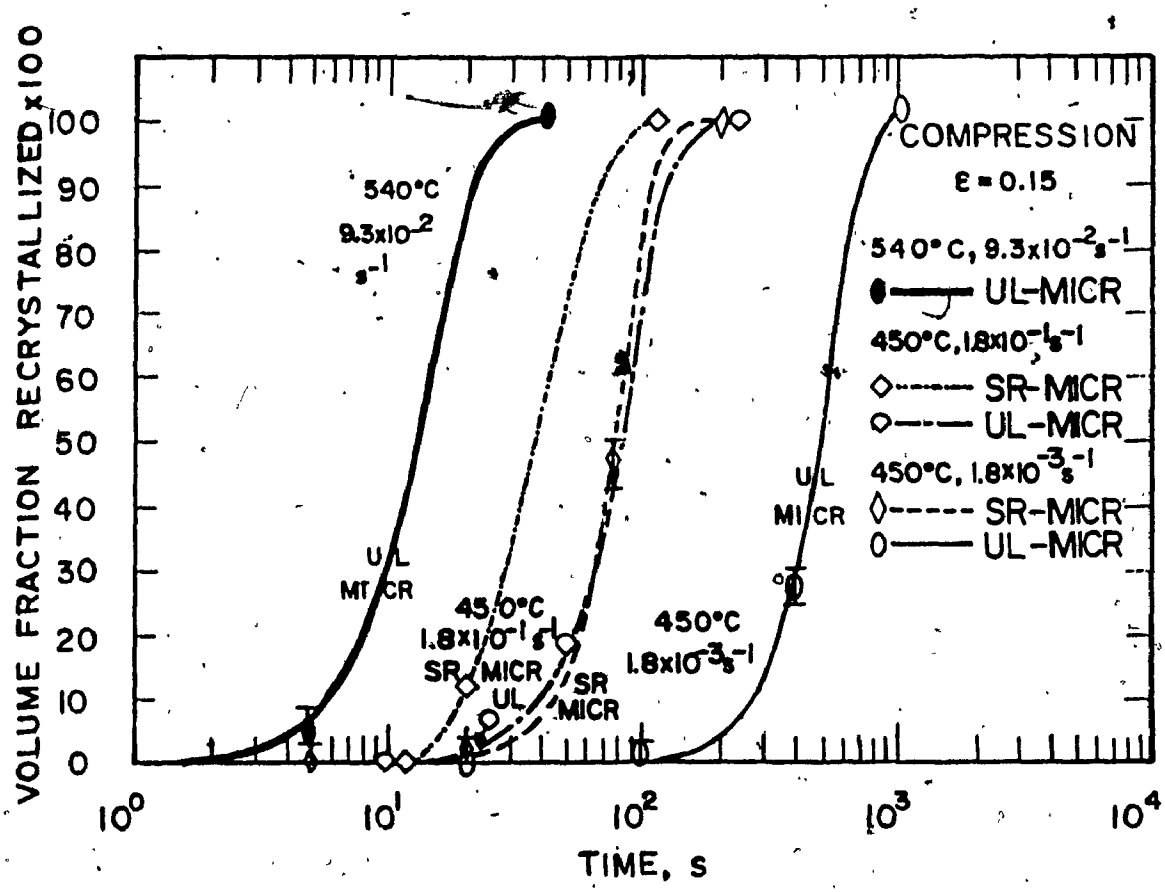

Fig. 4.16 Conditions and times at which samples were selected for metallography.

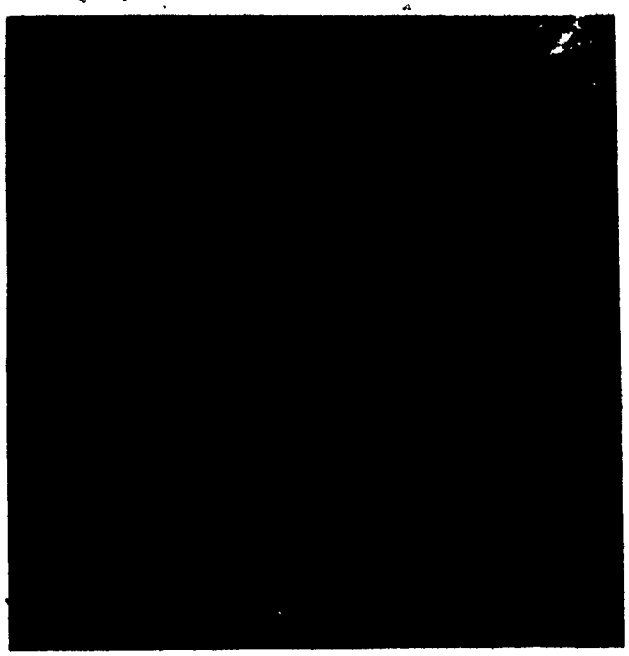

Fig. 4.17. Fully recrystallized microstructure before testing. (300 μm) (75X)

Fig. 4.18 Microstructure from IA, 450°C, 1.8×10^{-3} s^{-1} (Z_1) and immediately quenched. (75X)

Fig. 4.19 Microstructure from IA stress relaxed for 5s. (75X)

Fig. 4.20 Microstructure from IA UL annealed for 20s. (75X)

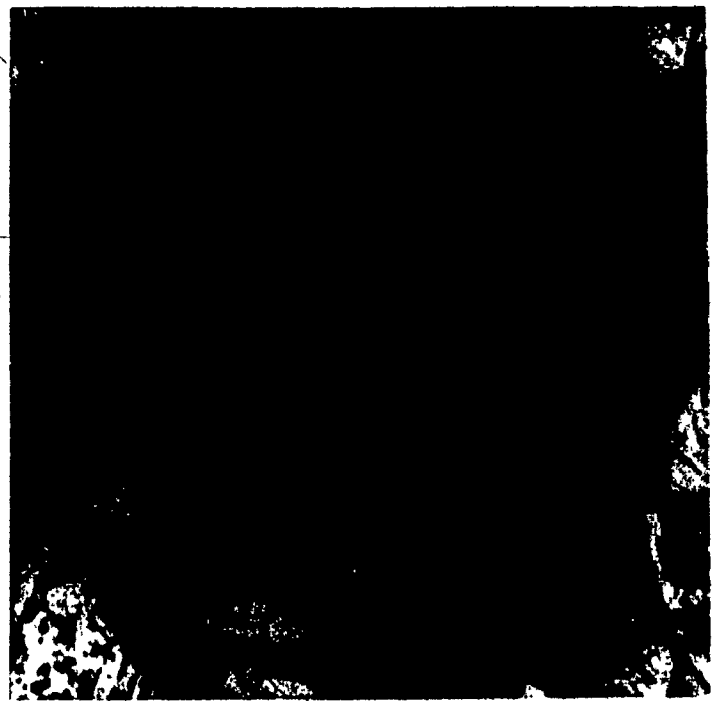

Fig. 4.21 Microstructure from IA SR for 20s. (75X)

Fig. 4.22 Microstructure from IA SR for 80s. (75X)

Fig. 4.23 Microstructure from IA UL annealed for 100s. (75X)

surface and irregular boundaries characteristic of deformed ones. No new grains are observed. In contrast, new grains appear in Figures 4.21, 4.22 and 4.23 for samples SR for 20 and 80s or UL annealed for 100s respectively: recrystallization in the second specimen is more advanced than in the third one. Figure 4.24 after UL annealing for 400s shows a higher population of new grains.

Tests at 540°C, $9.3X10^{-2}$ (IB). Figure 4.25 illustrates the immediately quenched microstructure and Figure 4.26 that of sample UL annealed for 5s. Both micrographs show new grains although the density of new grains is higher in the second sample.

Tests at 450°C, $1.8X10^{-1}$ (IIA). Neither the immediately quenched specimen (Fig. 4.27) or that after SR for 12s (Fig. 4.28) or that UL annealed for 10s (Fig. 4.29) show new grains. By contrast the microstructures SR or UL annealed for 20s (Figures 4.30 and 4.31) exhibit new grains, the density of new grains being more intense in the SR sample. Figure 4.32 shows that after UL annealing for 50s many new grains are evident. As shown in the micrographs above, recrystallization generally took place at existing boundaries. However, a few grains were observed close to inclusions as shown by Figure 4.33.

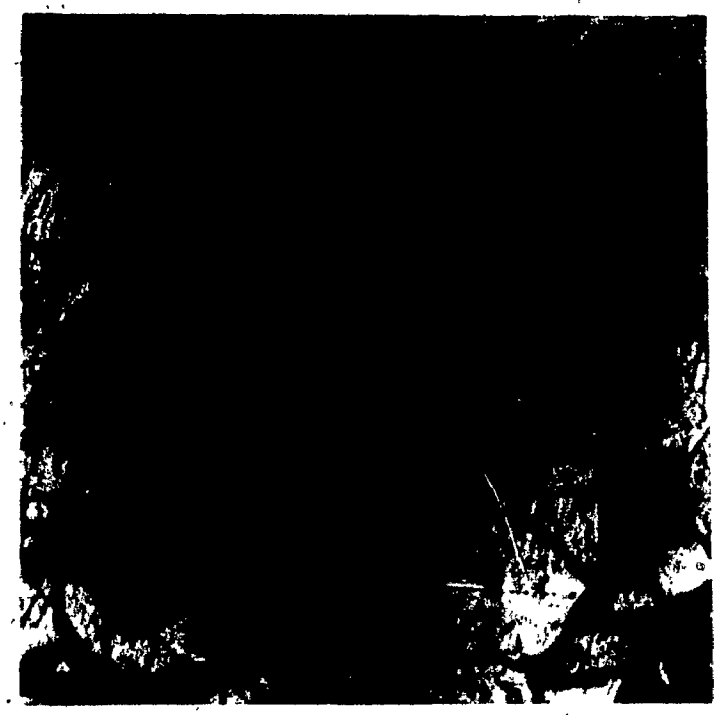

Fig. 4.24 Microstructure from IA UL annealed for 400s. (75X)

Fig. 4.25 Microstructure from IB, 540°C, 9.3×10^{-2} s^{-1} (Z_1), immediately quenched. (75X)

Fig. 4.26 Microstructure from IB UL annealed for 5s. (75X)

Fig. 4.27 Microstructure from IIA 450°C, 1.8×10^{-1} s^{-1} (Z_1) as deformed. (75X)

Fig. 4.28 Microstructure from IIA, SR for 12s. (75X)

Fig. 4.29 Microstructure from IIA, UL annealed for 10s. (75X)

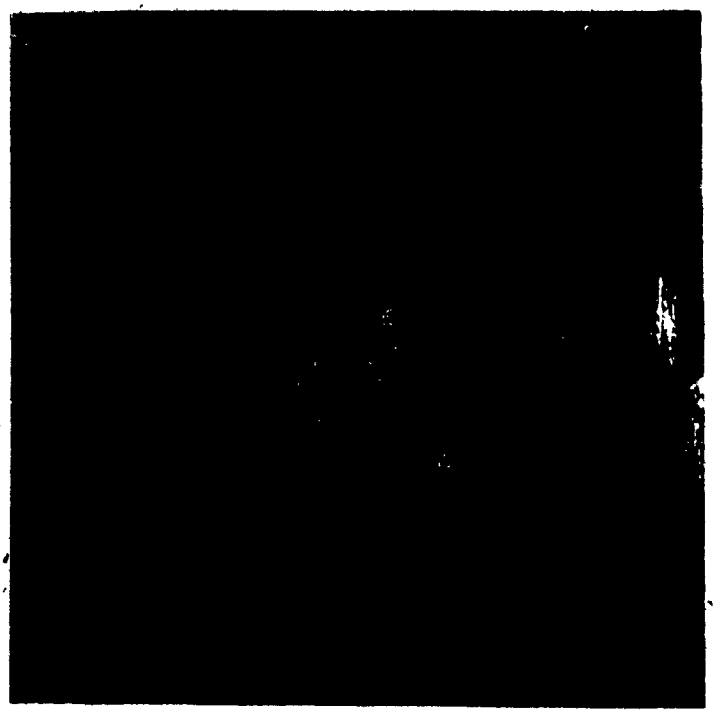

Fig. 4.30 Microstructure from IIA SR for 20s. (75X)

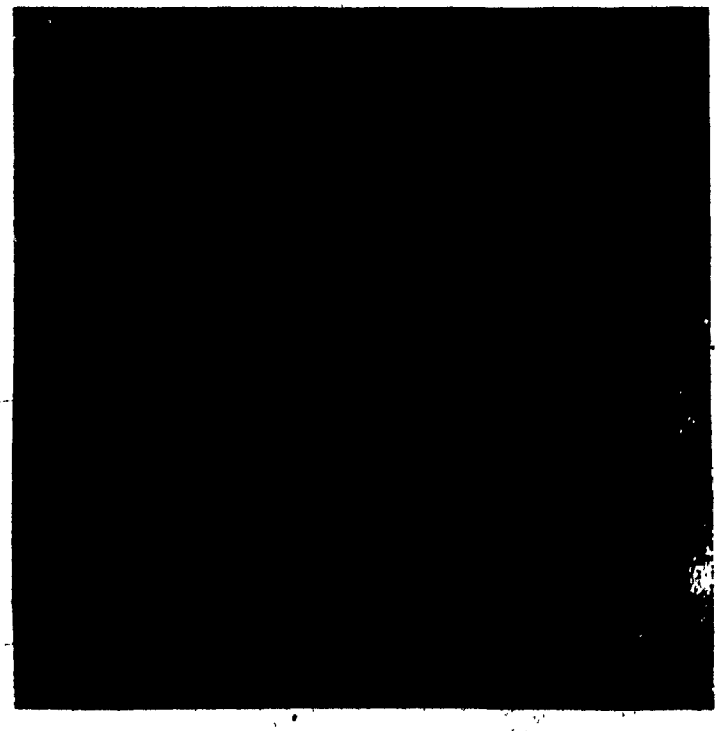

Fig. 4.31 Microstructure from IIA UL annealed for 20s. (75X)

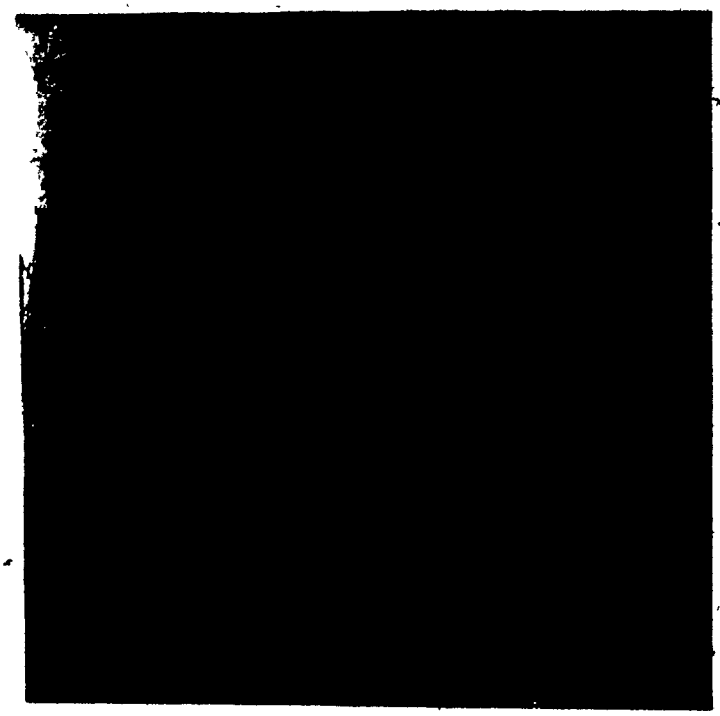

Fig. 4.32 Microstructure from IIA UL annealed for 50s. (75X)

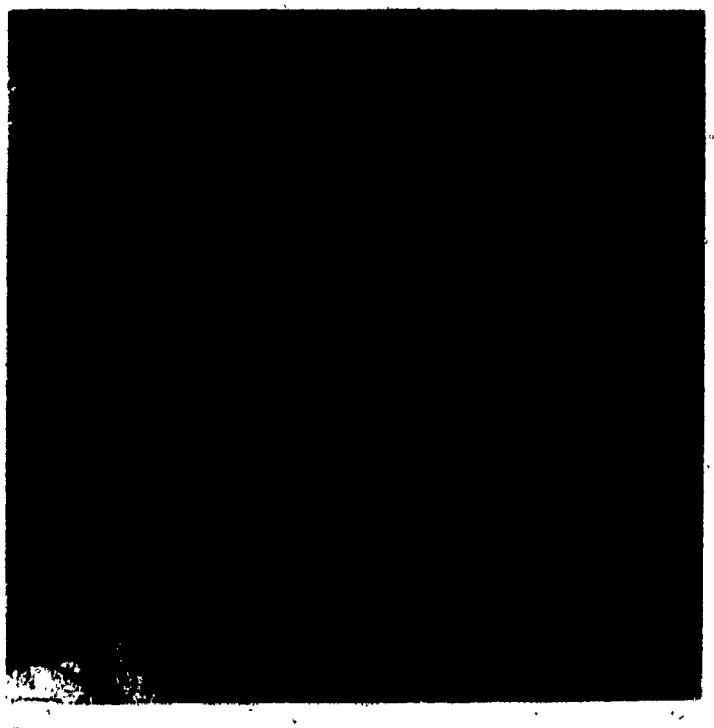

Fig. 4.33 New grains around inclusions, IIA UL annealed for 20s. (250X)

4.4.4.2 Fully Recrystallized Microstructures

Table 4.6 and micrographs 4.34 to 4.43 at 75X present the times and grain sizes of the fully recrystallized material. Fully recrystallized samples either SR or UL annealed after deformation at the same conditions show similar grain sizes, i.e. the grain sizes for IA are 194 μm (SR) and 195 μm (UL) and for IIA 157 μm (SR) and 162 μm (UL). Thus, although stress relaxation altered the kinetics, it did not have any effect on the recrystallized grain size. The grain size decreased considerably with rise in strain rate (IA vs IIA; IA vs IIB) and slightly with temperature (IA vs IB). The deformation mode did not affect the grain size appreciably (IIA vs IIB). The grain size of the sample deformed at 500°C, 1.8 s^{-1} (III) is much smaller than at 450°C, 1.8×10^{-1} s^{-1} (IIB) whereas they were expected to be similar since the two have the same Z. An explanation for such a result could be that the starting grain sizes in III and IV are much smaller since they were given larger intermediate strains than in IIB (Section 3.3.2). The higher Z in condition IV leads to a finer grain size than in III (the initial grain size conditions being similar).

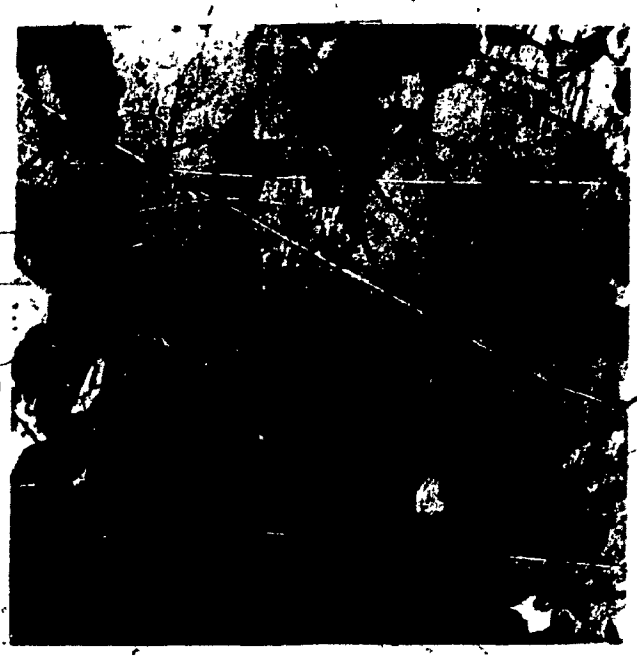

Fig. 4.34 Fully recrystallized microstructure from IA; compression at 450°C, 1.8×10^{-3} s^{-1}, UL annealed for 1000s. (195 μm) (75X)

Fig. 4.35 Fully recrystallized microstructure from IA; SR for 400s. (194 μm) (75X)

Fig. 4.36 Fully recrystallized microstructure from IB; compression at 540°C, $9.3 \times 10^{-2}, s^{-1}$, UL annealed for 40s. (170 μm) (75X)

Fig. 4.37 Fully recrystallized microstructure from IB; SR for 8s. (185 μm) (75X)

Fig. 4.38 Fully recrystallized microstructure IIA; compression at 450°C, 1.8×10^{-1} s^{-1}, UL annealed for 265s. (162 μm) (75X)

Fig. 4.39 Fully recrystallized microstructure IIA; SR for 100s. (157 μm) (75X)

Fig. 4.40 Fully recrystallized microstructure IIB; torsion at 450°C, 1.8×10^{-1} s^{-1}, UL annealed for 200s. (157 μm) (75X)

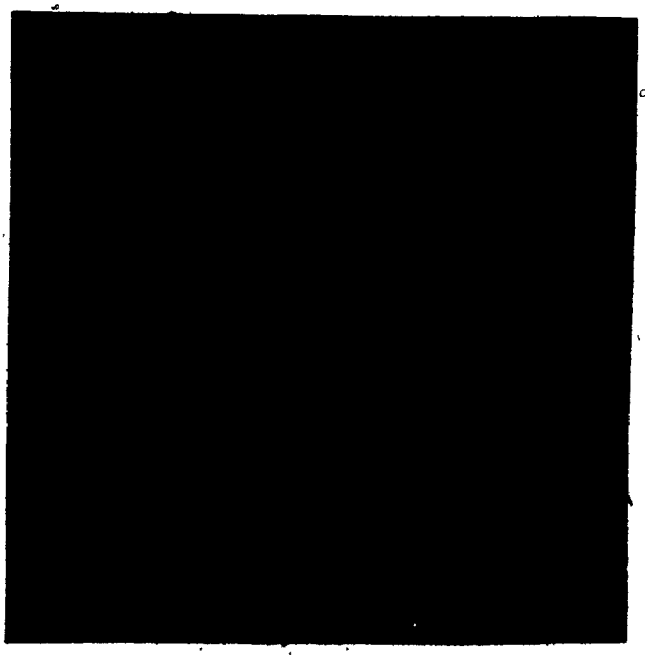

Fig. 4.41 Fully recrystallized microstructure IIB; SR for 100s. (169 μm) (75X)

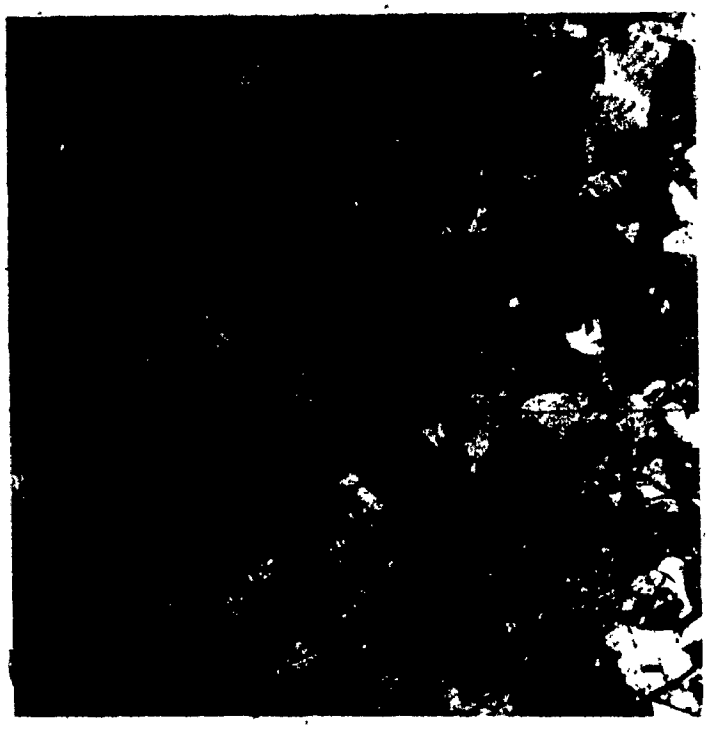

Fig. 4.42 Fully recrystallized microstructure III; torsion at 500°C, 1.8 s^{-1} UL annealed for 30s. (76 μm) (75X)

Fig. 4.43 Fully recrystallized microstructure IV; torsion at 450°C, 1.8 s^{-1} UL annealed for 80s. (62 μm) (75X)

Table 4.6. Fully Recrystallized Grain Size

Set	Test Conditions °C	s^{-1}		$\bar{D}$ μm
IA	450	1.8×10^{-3}	UL	195
			SR	194
IB	540	9.3×10^{-3}	UL	170
			SR	185
IIA	450	1.8×10^{-1}	UL	162
			SR	157
IIB			UL	157
			SR	169
III	450	1.8	UL	62
IV	500	1.8	UL	76

Table 4.7. Recovery Kinetic Parameters

Set	Test Condition °C	s^{-1}		s MPa	t_o s
IA (Z_1)	450	1.8×10^{-3}	UL	22.9	91.6
IA (Z_1)	450	1.8×10^{-3}	SR	20.4	39.4
IB (Z_1)	540	9.3×10^{-2}	UL	34.3	4.3
IIA ($100Z_1$)	450	1.8×10^{-1}	UL	27.2	3.0

4.5 Recovery

The kinetic parameters for recovery after compression s and t_o (Section 2.3.2.2, Eqn. 2.24) are shown in Table 4.7 and Fig. 4.44. The plots depict the rate of decline of the reloading yield stress with time starting when $\sigma_r = \sigma_m$ at t=0.

4.5.1 Recovery Kinetics

For a constant Z it is observed in Table 4.7 and Fig. 4.44 that stress relaxation reduces the slope s slightly (IA UL vs IA SR), but that a higher temperature during annealing greatly increased it (IA vs IB). An increase in strain rate (and stress σ_m) at the same deformation and annealing temperature increases the s value noticeably. On the other hand, stress relaxation, and to a greater degree increase in temperature and strain rate decreases the parameter t_o (IA UL vs IA SR, IB UL, IIA UL). Thus, the net effect of these variations is that SR moderately reduces the rate of recovery but augmentation in temperature and strain rate accelerate it.

4.5.2 Analysis of the Substructure

The samples submitted to inspection by transmission electron microscopy are indicated in Figure 4.45.

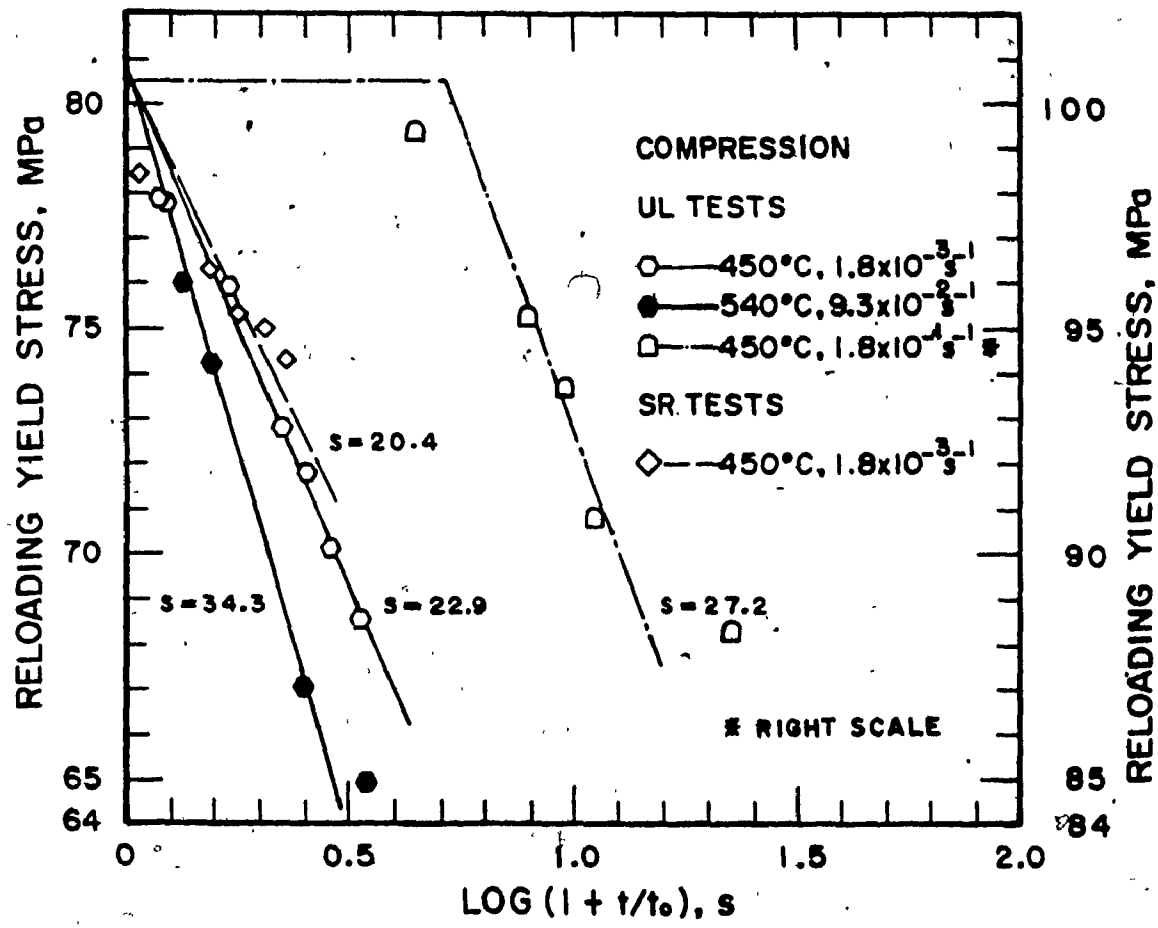

Fig. 4.44 Recovery kinetics under conditions IA UL and SR (Z_1), IB UL (Z_1) and IIA UL (100 Z_1).

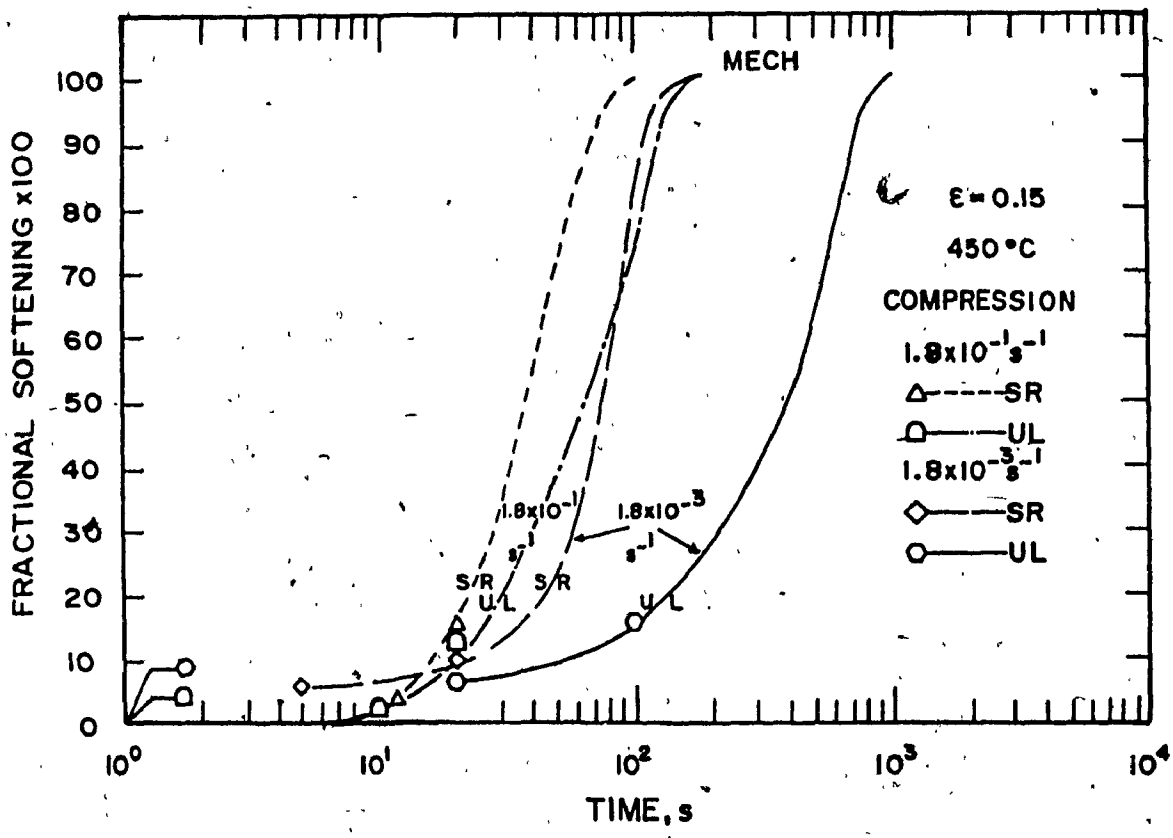

Fig. 4.45 Conditions and times at which samples were selected for TEM.

Tests at 450°C, $1.8X10^{-3}$ s^{-1} (Z_1). Samples immediately quenched after deformation exhibit a range of substructures. Figure 4.46a shows areas of dislocation tangles and small cells, whereas Figure 4.46b exhibits some elongated cells with low interior density indicating some degree of dynamic recovery. After UL annealing for 20s, cells with narrow tangled walls are common (Fig. 4.47a) and regions with larger cells and sharper walls (Fig. 4.47b). After UL annealing for 100s subgrains of larger size and more ordered walls were observed (Fig. 4.48a). However, in some cases dislocation tangles were still observed next to recovered subgrains (Fig. 4.48b). The substructure after SR for 5s resembles that of the immediately quenched sample. It consists in some areas of cells with ragged walls (Fig. 4.49a) and in other areas of dislocation tangles (Fig. 4.49b). After SR for 20s, the cells are better formed but still with thick walls (Fig. 4.50a) and there are still areas with dislocation tangles (Fig. 4.50b).

Tests at 450°C, $1.8X10^{-1}$ s^{-1} ($100Z_1$). The substructure of specimens quenched immediately after deformation contains both areas of dislocation tangles (Fig. 4.51a) and cells with very ragged walls (Fig. 4.51b). High dislocation densities and small cell dimensions required the use of the high magnification indicated in Fig. 4.51. The substructure after UL annealing for 10s is not much

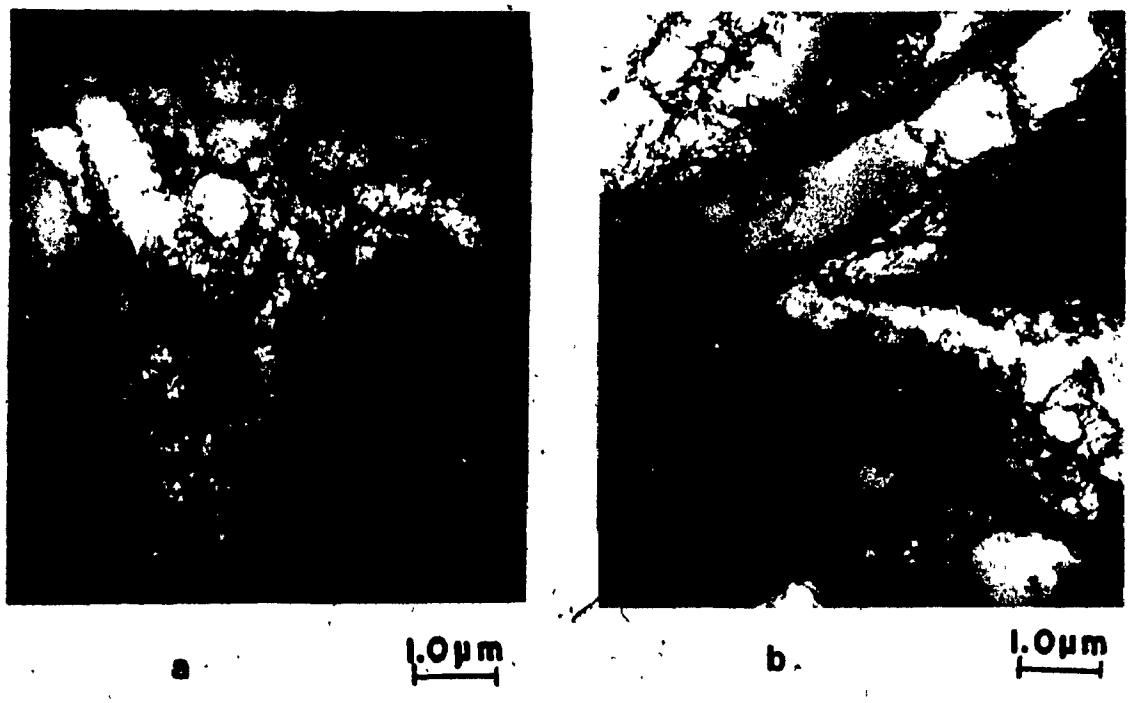

Fig. 4.46 Substructure from IA, 450°C $1.8X10^{-3}$ (Z_1) as deformed.

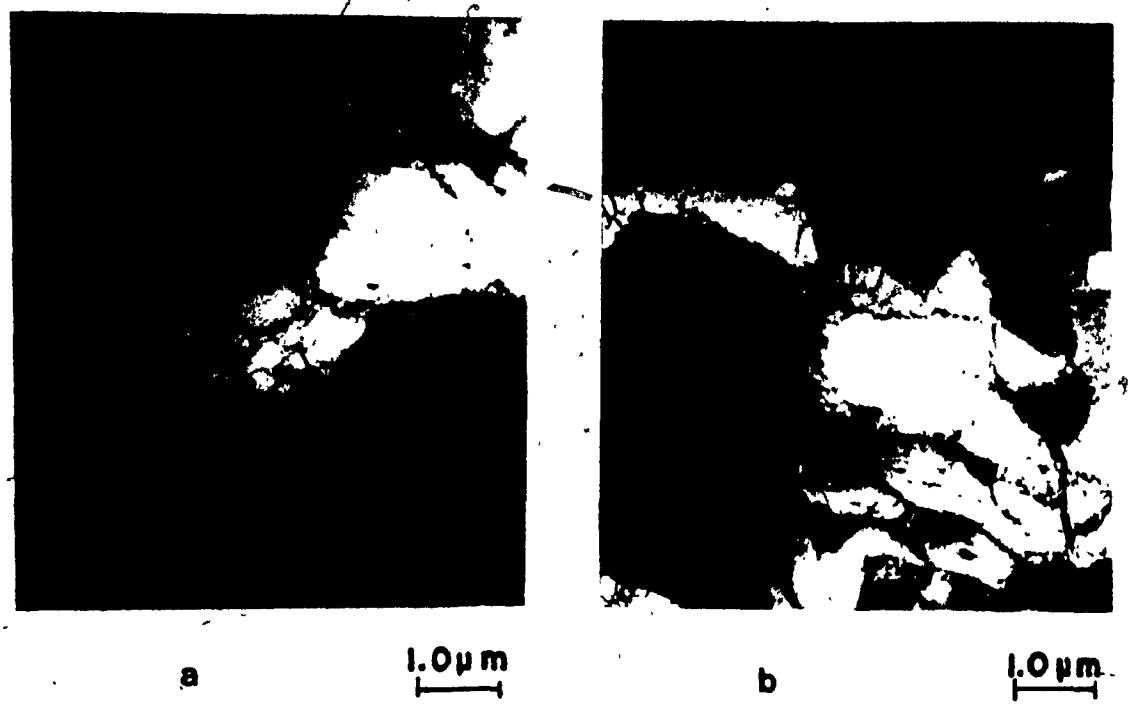

Fig. 4.47 Substructure from IA, UL annealed for 20s.

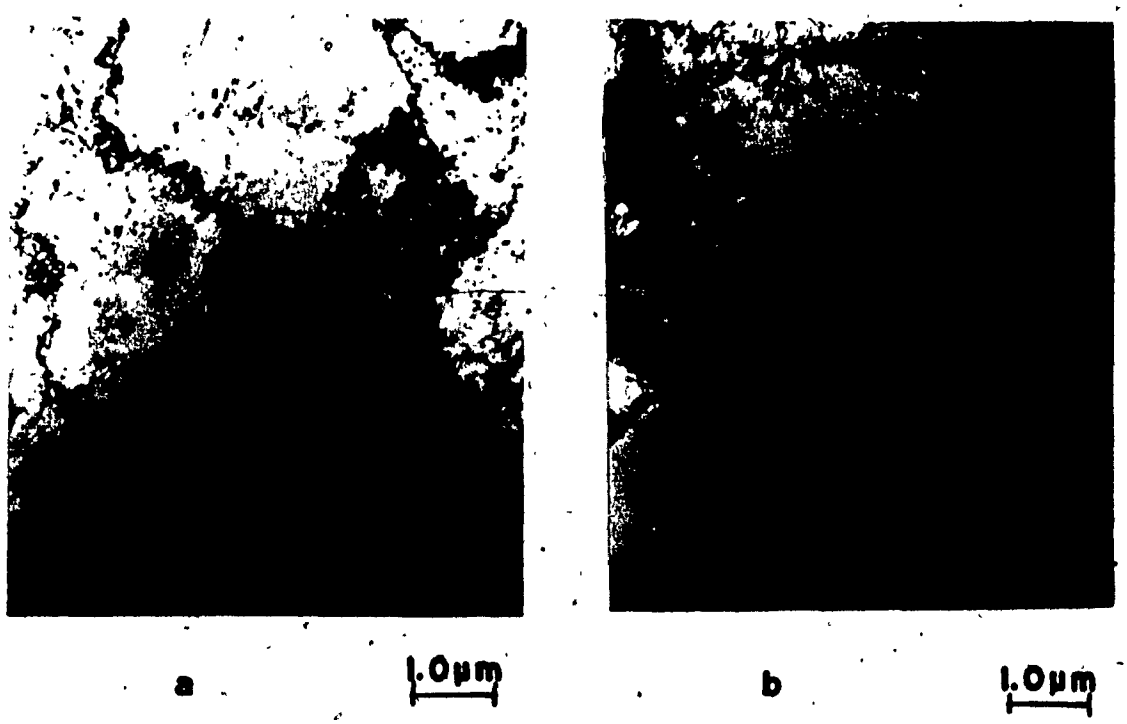

Fig. 4.48 Substructure from IA, UL annealed for 100s.

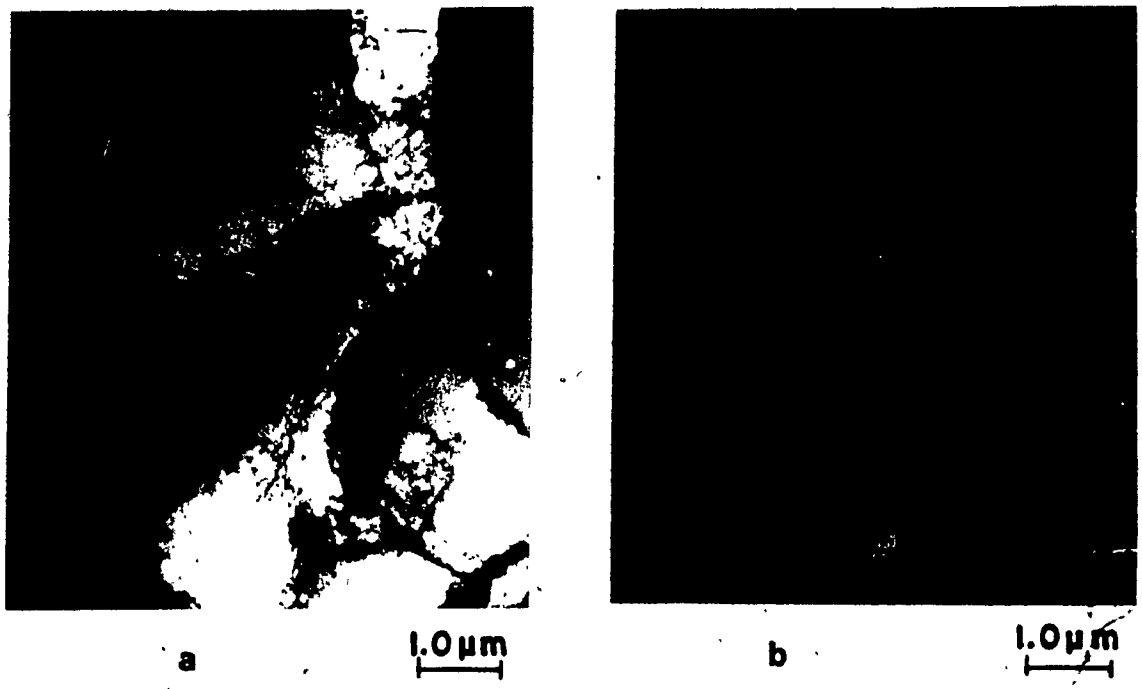

Fig. 4.49 Substructure from IA, SR for 5s.

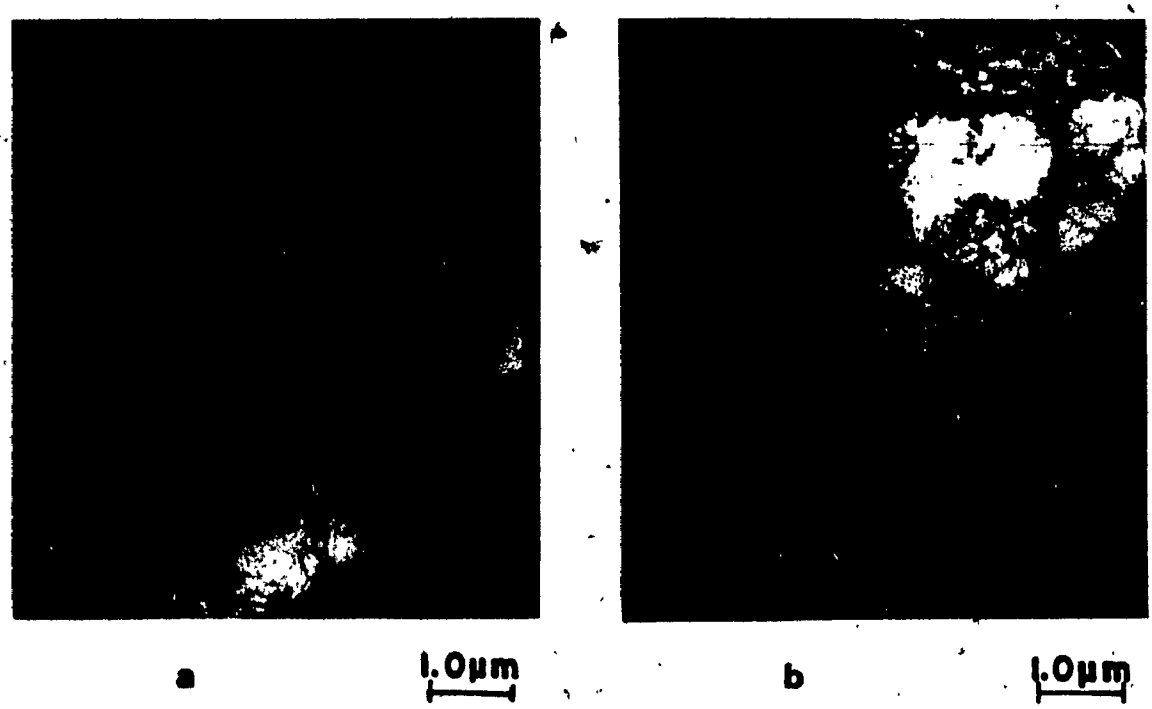

Fig. 4.50 Substructure from IA, SR for 20s.

different from that of the above specimen: poorly formed cells (Fig. 4.52a) and tangles (Fig. 4.52b). Clearly distinguishable cells with thick dense walls characterize the substructure after UL annealing for 20s (Fig. 4.53a,b). The substructure after SR for 12s shows some regions of poorly formed cells (Fig. 4.54a) and others of cells with ragged walls (Fig. 4.54b). After SR for 20s (Fig. 4.55) the substructure is still similar to the above but with noticeable decrease in dislocation density.

Comparison of the substructures produced by deformation IA after 20s of UL (Fig. 4.47) or SR (Fig. 4.50) annealing shows that the former is in a more advanced stage of static recovery in sofar as it has less regions of tangles and more regions of subgrains. Moreover, after 100s, the UL specimen exhibits considerable increase in static recovery whereas the SR specimen has largely recyrstallized (Fig. 4.45). After deformation at the higher strain rate (condition IIA), the substructure is much less dynamically recovered than at the lower rate (IA). In UL or SR annealing up to 20s after IIA (Figs. 4.52-4.55), static recovery clearly proceeds but still does not reach a level much higher than the as-deformed material from IA. Moreover, the range of density and cellularity is so great after either SR or UL annealing that it is not clear which is more advanced.

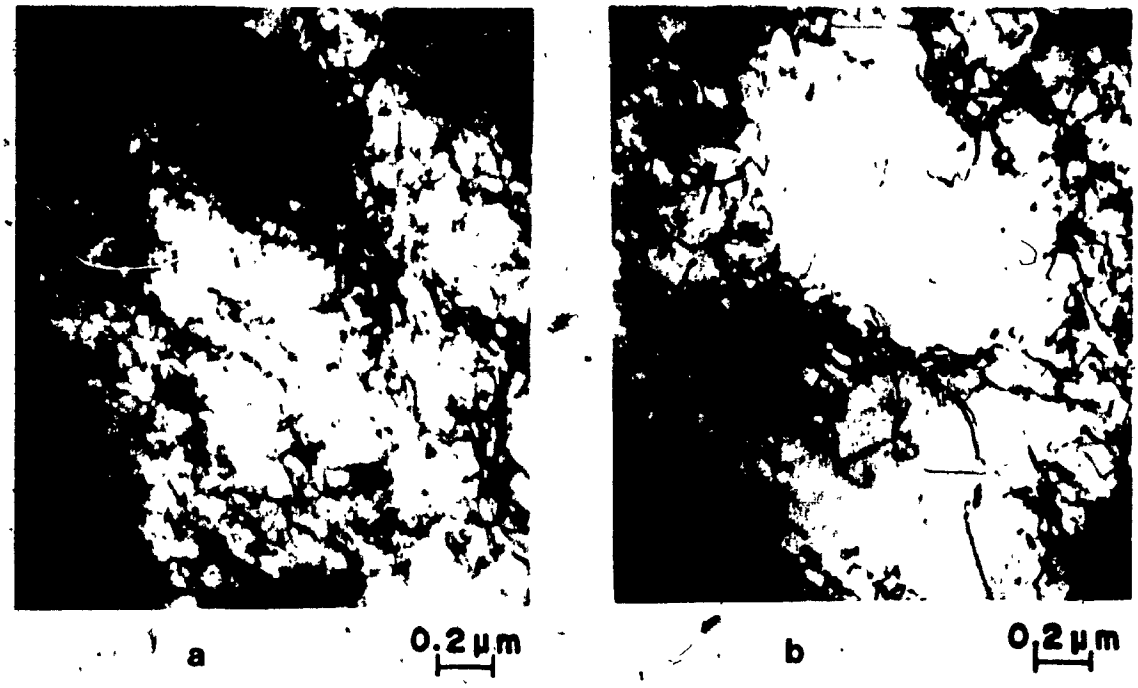

Fig. 4.51 Substructure from IIA, 450°C, 1.8×10^{-1} s^{-1} (100 Z_1) as deformed.

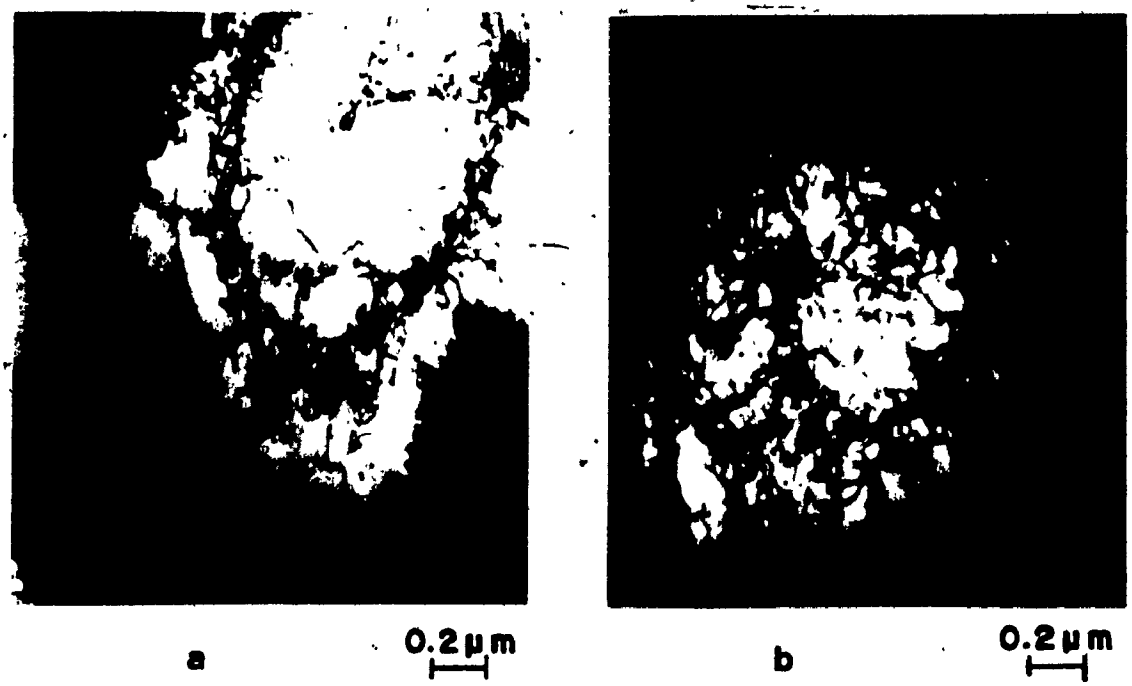

Fig. 4.52 Substructure from IIA, UL annealed for 10s.

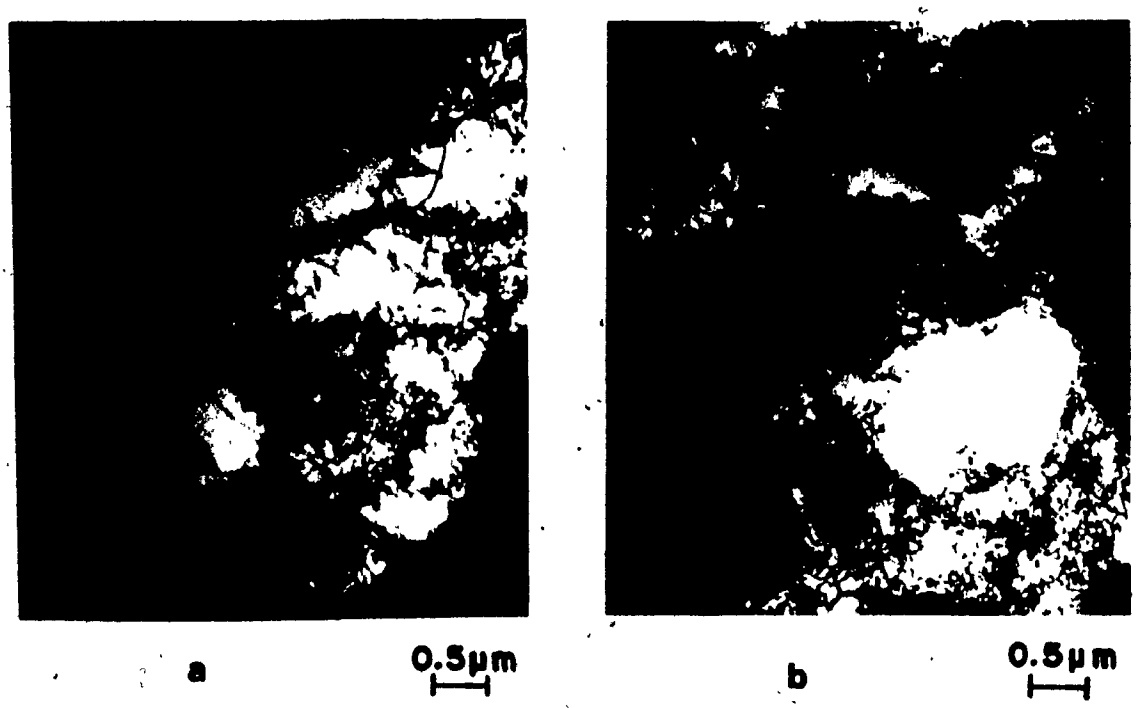

Fig. 4.53 Substructure from IIA, UL annealed for 20s.

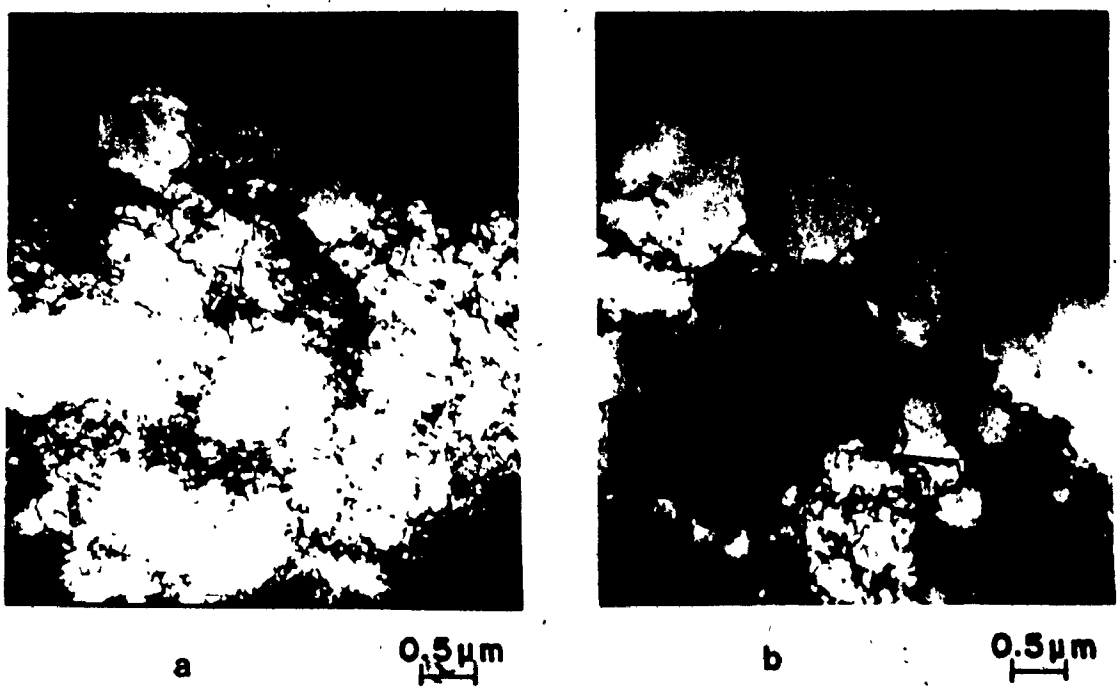

Fig. 4.54 Substructure from IIA, SR for 12s.

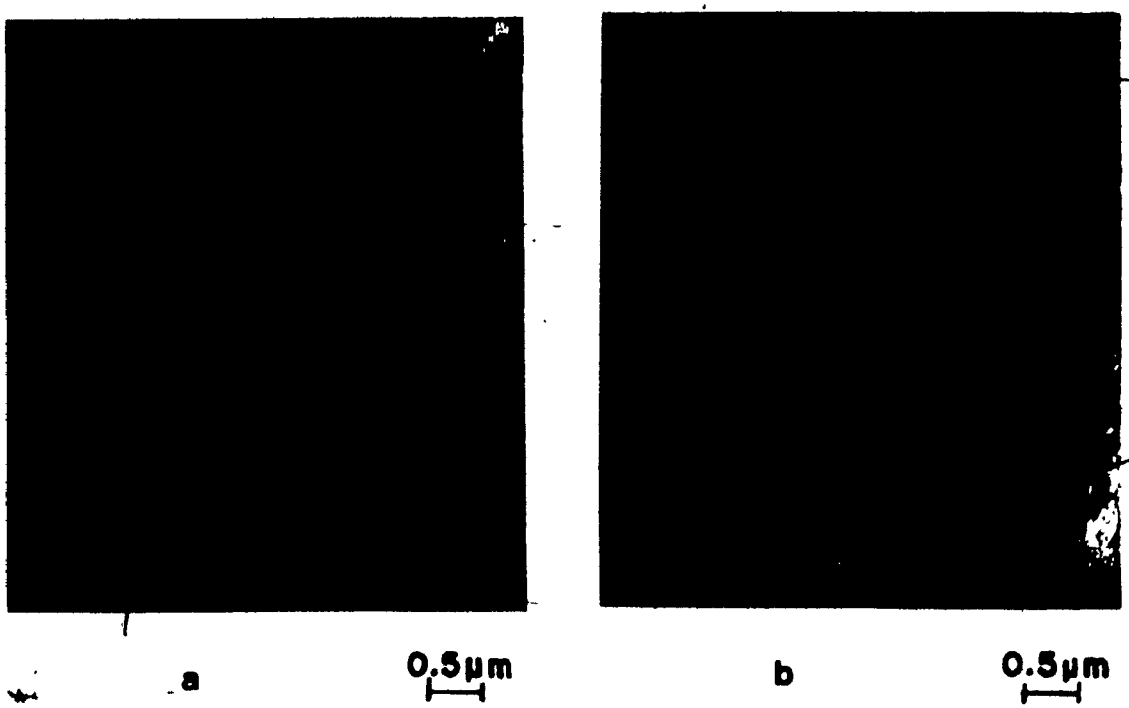

Fig. 4.55 Substructure from IIA, SR for 20s.

4.5.3 Misorientations

The misorientations between cells in the preceeding micrographs were measured; the minimum and maximum misorientation between cells for the different test conditions are listed in Table 4.8. Figure 4.45 is again the key for these results. The misorientations in a sample range from a few minutes to about one degree which are in agreement with the values reported in the literature (135). There appears to be little variation with mode of annealing or strain rate.

Table 4.8. Misorientation between Cells

Test Condition	Annealing time, s	Misorientation Angle min.	max.
450°C, 1.8×10^{-3} s^{-1}	0	9'	40'
IA UL	20	18'	1°7'
	100	9'	20'
IA SR	5	20'	1°11"
	20	7'	1°11'
450°C, 1.8×10^{-1} s^{-1}	0	4'	38'
IA UL	10	7'	16'
	20	4'	49'
IA SR	12	4'	38'
	20	4'	18'

CHAPTER 5

DISCUSSION

5.1 Effect of the Experimental Variables on the Restoration Kinetics

5.1.1 The Unloaded Tests

The effect of temperature on the restoration kinetics can be determined from the data of samples deformed to the same initial stress level and at the same Z, namely, tests IA, IB in compression and IIB, III in torsion. The specimens annealed at the higher temperature, ie IB and III show a faster decrease in the level of the reloading curves (Figs. 4.1a, 4.2a, 4.4a and 4.6). The same trend was observed in previous hot working of Cu (32) and in other reports from the literature (81,174). The annealing times for full softening decrease by the factors 1/25 and 1/6 for changes from 450°C (IA) to 540°C (IB) and from 450°C (IIB) to 500°C (III) (Figs. 4.10 - 4.12). These observations agree well with those in the hot torsion of zone refined iron where, after deformation to the same flow stress, an increase of 50°C yields a decreased time for full recrystallization of 1/10 (58). Samples of Cu compressed only to 0.05 (σ_m=64.1 MPa) showed a decrease in the time for

complete softening of 1/15 for a 50°C rise (32). Such high enhancement factors are consistent with thermally activated, static recovery and recrystallization. The activation energies derived for recrystallization were 233 kJ/mol for UL MECH and 171 kJ/mol for SR MECH. These correspond to values of 290 kJ/mol and 214 kJ/mol for UL and SR respectively after a strain of 0.05 (32). They are reasonably similar to values in the literature.

Because high temperature promotes an early start of recrystallization whereas a low temperature favours extensive recovery both at the beginning and throughout annealing, the softening curves are steep in the first case and less steep in the second (Figs. 4.10 and 4.12). In agreement with the S-shaped curves, a higher annealing temperature corresponds to a higher power p in the Avrami relation (Eqn. (2.27), ie a steeper MECH softening kinetic line in Figs. 4.13 to 4.15. The MECH p's become close to 1 as the temperature declines to 450°C. In previous work for a prestrain of 0.05 (32), a p value of 1.4 for 450°C and of 2.0 for 500°C was observed. A value of p=1.33 for recovery of ETP Cu deformed under similar conditions was determined by Luton et.al. (120) using a modified Avrami equation. The retarding effect of recovery on the softening kinetics is also observed in lower values of the k parameter associated with lower temperatures (Table 4.4) (120).

The accelerating effect of temperature on recrystallization does not affect the rate of growth alone but of nucleation too. An increase of 90°C caused a reduction of the incubation time by 1/100 (Fig. 4.10) as shown above. This cannot be confirmed in the torsion tests II, IV because fast recrystallization prevented observation of incubation. Although temperature rise increases the rates of nucleation and recrystallization, it does not affect the nuclei density, since the final recrystallized grain sizes are about the same (194 μm vs 170 μm) as shown by the micrographs in Figs. 4.34 and 4.36 (see also Table 4.6). The p from metallography (MICR) is slightly higher at the lower temperature for which there is no explanation except experimental error. The great temperature dependence of k (and of recrystallization) is shown by its increase through 6 orders of magnitude with a rise of 90°C (Table 4.4). A similar dependence has been reported before (120).

The effect of temperature on the rate of recovery is also shown by a rise in the slope of the recovery kinetic lines (Fig. 4.44). The rate s increased 1.5 times by changing the temperature from 450°C (IA) to 540°C (IB). On the other hand, t_o decreased by a factor of 1/21 for the same change in temperature. Previously (32), a change from 450°C to 500°C increased s by a factor of 3.5 and diminished t_o by a half. The activation energy determined

for UL recovery was 222 kJ/mol, this compares well with 250 and 212 kJ/mol for UL and SR recovery after a strain of 0.05 (32). As one expects, for a mechanism dependent on dislocation climb, it agrees closely with the Q for diffusion 200-230 kJ/mol (40). Electronmicroscopy of samples tested at 540°C was not carried out, so that comparison with those examined at 450°C was not possible. However optical micrographs of specimens IB immediately quenched showed some new small grains (Fig. 4.25), while samples IA only showed new grains after 100s (Fig. 4.23). Thus, restoration to form nuclei occurred at a higher rate at the higher temperature, but there was much greater opportunity for general recovery at the lower one. The area between the MECH and MICR curves, which can be considered as a measure of the amount of recovery, is evidence that at low temperature (IA) recovery takes place more widely than at high temperature (IB). Because the driving force for both recovery and recrystallization is the dislocation stored energy, as recovery proceeds more extensively, recrystallization occurs at a slower rate (Fig. 4.10).

The effect of strain rate on the restoration can be assessed from the data of experiments carried out at the same temperature, ie tests at IA, IIA in compression and IIB, IV in torsion. Samples deformed at the higher strain rate (IIA and IV) exhibit a quicker decrease in the level

of the reloading curves (Figs. 4.1a, 4.3a, 4.4a and 4.5) as has been observed before (32, 81, 174). For 100 and 10 fold increases in strain rate (Figs. 4.10-4.12), the annealing time for complete restoration diminishes 1/5 and 1/2 respectively. High strain rate hastens both the start and the progress of recrystallization (37). The higher rise in strain rate above led to a reduction of 1/10 in incubation time. Although recovery is also accelerated with increases in strain rate, softening due to recrystallization overshadows that due to recovery and a steeper X vs log t arises with increasing strain rate (Figs. 4.11 and 4.12).

Increases in strain rate raise slightly the values of MECH p and k and accelerate softening. It is a general observation that raising the strain rate diminishes the degree of dynamic recovery so that the material starts static restoration with a high dislocation density and therefore a high driving force for recovery and recrystallization (37, 174). Because the latter process provides a larger proportion of the softening, p and k are larger for tests at the higher strain rate (Figs. 4.13-4.15).

Besides enhancing the rates of nucleation and growth, strain rate increases the nuclei density. As a consequence the full recrystallized grains are finer (IA: 195 μm vs IIA: 162 μm) as shown in Figs. 4.34 and 4.38, and

in Table 4.6. The considerable difference in size between the recrystallized grains of samples IIB and IV must be primarily ascribed to different thermo-mechanical treatments between torsion steps as explained in Section 3.3.2. The MICR p's do not change with strain rate, they are about 3 in compression; no information is available in torsion (Figs. 4.13, 4.14 and Table 4.4). MICR k was increased by 3 orders of magnitude by an increase of the strain rate by a factor of 100.

For the rise in strain rate shown above, the recovery rate s in Fig. 4.44 became 20% higher and t_o decreased 30 times (Table 4.7). The sample deformed at the lower strain rate (IA) exhibits well formed cells before annealing (Fig. 4.46b) whereas that at the higher strain rate is characterized mainly by very thick tangles of dislocations (Fig. 4.51). Of course, substructure IA is closer to the condition for dynamic recrystallization (ε_p=0.21) whereas IIA is quite far from that condition (ε_p=0.52). Both substructures underwent recovery during holding but the differences at the end of hot working made it difficult to reach a conclusion about the influence of strain rate on the progress of static recovery. The appearance of new recrystallized grains after only 20 s of annealing in the higher strain rate specimen compared to 100 s in the lower rate one is indicative that some

non-homogeneous recovery processes are accelerated by the strain rate increase. However, the smaller area between the MECH and the MICR curves for 1.8×10^{-1} s^{-1} (Figs. 4.10 and 4.11) indicate that the total amount of recovery decreased with increase of strain rate.

The difference in σ_m for the same Z (IIA vs IIB) (Figs. 4.3a and 4.4a) is the result of experimental differences in sample preparation and in testing procedures which led to variations in grain size (Sections 3.2.2 and 3.3.2).

The faster yield stress drop (Fig. 4.1-4.6) and earlier softening curves (Figs. 4.11 and 4.12) of the torsion tests when compared with those of the compression ones can be attributed to a gradient of restoration rates in the torsion specimens. The material deformed at a high rate close to the surface, recrystallizes quickly whereas the interior is still undergoing incubation. At the lower strain rate near the center, recovery extends over a longer which explains why the torsion curves do not cross those for compression. Finally, the grain size is finer in torsion which explains why the torsion curves do not cross the compression but are shifted to shorter times. The lower values of p ($\sim$1) in the torsion tests are attributed to the gradient of deformation and softening as explained above. If the experimental differences did not exist one would

expect torsion to yield similar recrystallized grain sizes as compression when the material is deformed under the same conditions (IIA: 162 μm vs IIB: 157 μm) (Figs. 4.38, 4.40 and Table 4.6).

In the above discussion the compression and torsion results are in good agreement. However, there are a number of differences which will be discussed further below. Regrettably, there are quantitative differences in the unloading stress, but scarcity of material prevented repetition of the experiments.

5.1.2 The Stress Relaxation Tests

Temperature affects the restoration kinetics of stress relaxed specimens as it does the kinetics of the unloaded ones. For samples deformed to the same initial stress level and at the same Z in tests IA and IB (Figs. 4.1b and 4.2b), the drop of the reloading flow curve is faster as the temperature is higher. Consequently the annealing time for full softening shortens by a factor of 1/20 for an increase of temperature from 450°C (IA) to 540°C (IB) (Fig. 4.10) similar to the UL ratio. Moreover, the softening curve becomes steeper with increase in temperature (Fig. 4.10) so that the slope p of the MECH kinetic line (Fig. 4.13) increases from 1.6 (IA) to 2.2 (IB) and the k value rises by two orders. In SR restoration of Cu after a

strain of 0.05 at the same Z, almost the same value of p is found for 450°C (1.4) and 500°C (1.3), but a k one order of magnitude higher for the latter temperature (32). The final grain sizes are about the same independent of temperature (IA, 195 μm and IB 185 μm; Figs. 4.35 and 4.37). In IA the MICR p (3.2) is much higher than the MECH p (as in the UL tests). The low value of the latter is related to the recovery included in the softening which is shown by the area between the MECH and MICR curves (Fig. 4.10).

Data from tests IA, IIA in compression show that, as in the UL tests, a faster decrease in the level of the reloading curves accompanies an increase in strain rate (Figs. 4.1b, 4.3b). The times for both full softening and incubation of recrystallization reduce by half as the strain rate increases 100 times (Figs. 4.10 and 4.11). As corresponds with more rapid softening kinetics in Figs. 4.10 and 4.11, higher values of MECH p and k are observed for increasing compression rates (Table 4.4). In test IIA, the fraction recrystallized almost coincides with the fractional softening so that there is little difference in p and k for MICR and MECH. This results in a large difference in MICR p and k with strain rate (Table 4.4). Because of the similarity of the MECH softening curves at 540°C (IB) and 450°C (IIA) one could hypothesize that there would only be a small difference between the MICR (recrystallization)

and MECH (softening) curves and p values at 540°C. The nuclei density increased with strain rate as in the UL case, so the size of the new recrystallized grains is 157 μm (IIA) compared to 194 μm (IA) (Figs. 4.35, 4.39 and Table 4.6). New recrystallized grains appear after SR for 20s at both low (IA) and high strain rate (IIA); however, in the latter case the subsequent progress is faster (Figs. 4.21, 4.30 and Table 4.5).

The recovery kinetic parameter s and t_o were determined from the small difference in the SR MECH and SR MICR curves for 450°C, $1.8X10^{-3}$ s^{-1} IA (Fig. 4.10). At the higher strain rate (IIA) the amount of recovery shown by the area between the MICR and MECH curves is very small (Fig. 4.11) so that, it was not possible to determine the recovery kinetic parameters. At 540°C (IB) the lack of recrystallization data prevents determination of the amount of recovery; however, one expects it to be small as in case IIA. Thus in SR, increase in both temperature and strain rate greatly reduce recovery.

From TEM on tests IA and IIA (IB not available), the as-worked substructure shows a decrease in dynamic recovery with increase in strain rate (Figs. 4.46, 4.51). The progress of static recovery with time is apparent in micrographs from 5, 10, 12 and 20 s (Figs. 4.49, 4.50, 4.54 and 4.55). However because of hetereogeneity of the samples

it is difficult to say whether it proceeds faster in the low or high strain rate material.

Similar patterns of behaviour for the torsion and compression specimens is observed for both the SR and UL tests. A faster yield stress fall (Figs. 4.3b and 4.4b), earlier softening curves (Fig. 4.11) and lower MECH p values (~1) (Fig. 4.14) characterize the torsion experiments as compared with the compression ones. The new recrystallized grain sizes for the two modes of test are about the same as in the UL case (IIA: 157 μm vs IIB: 169 μm) (Figs. 4.39, 4.41 and Table 4.6).

5.1.3 Stress Relaxation and Structural Changes

The relaxation stress σ_{SR} decreases gradually as substructure resisting flow undergoes SRV. However, as SRX occurs the substructure is removed by the advancing grain boundaries so that the stress falls more rapidly. σ_{SR} is primarily supported by the non-recrystallized regions and by some substructure arising from plastic deformation of the new recrystallized grains. When extensive recovery proceeds concurrently with recrystallization (IA, Fig. 4.10 and 4.50) no inflection point is evident. Analysis of Fig. 4.7 shows that the initial fall of stress (Stage I) is very pronounced either when the initial driving force for stress relaxation is high (IIA, VII), as given by a large

difference $\sigma_m - \sigma_{SRST}$ or by a large ratio σ_m/σ_{SRST} (Fig. 4.8 and Table 4.2), or when the temperature is high (IB) enhancing the thermal activation of plastic flow. Otherwise, stage I is very mild (V and VI) or is not noticeable (IA). The duration of the plateau following stage I in IIA corresponds roughly with the incubation time for recrystallization (12s, Fig. 4.11) which gives rise to a sharp inflection as observed by Gronostajski et al. (175). However, in IB an inflection appears at about 4s when recrystallization is already under way (Fig. 4.25 and Table 4.5); thus the inflection may still indicate an acceleration due to recrystallization (175), without precisely pinpointing its start. Stage III saturation is reached sooner and its level is lower as the initial stress σ_m or the temperature is higher (ie when the fractional softening is faster).

The difference between the reloading yield stress and the σ_{SR} value is higher at earlier times than at those close to full recrystallization, with the exception of specimen IA stress relaxed for 2s, where σ_r and σ_{SR} are about the same (Table 4.1). These observations are reflected in the higher values of FR (Eqn. 3.20) when compared with FS ones (Fig.4.9). When compared to X_R which is below FS at short times, the difference is even greater. However, because relaxation saturation is approached very

slowly the FR curves are lower than the FS ones as the latter approach unity. The somewhat larger divergence between the FR and FS curves which are observed in the conditions IIA and IB may be related to the lower values of σ_{SRST} (Table 4.2). Thus while the SR curves give some indication of the start of recrystallization (inflection) or the completion of restoration (saturation), they do not do so precisely and at a given time FR is much greater than FS, or X_R, for values less than 60%.

5.1.4 Comparison of Relaxation and Unloaded Tests

Stress relaxation increases the rate of fractional softening over that of UL annealing (except at very short times) under all the test conditions examined (Fig. 4.1-4.11). As the temperature increases the effect is reduced as can be seen by contrasting the ratios t_{UL}/t_{SR} of IB and IA for different degrees of softening (Table 4.3) or by observing that the separation between the UL MECH and SR MECH curves is less in IB than in IA (Fig. 4.10). In a like manner as the strain rate increases, the effect is reduced for condition IIA compared to IA as indicated by the lower ratios t_{UL}/t_{SR} in Table 4.3 and the smaller spacing of the UL and SR curves (Fig. 4.10 and 4.11). Furthermore the difference between SR and UL is reduced in torsion compared to compression (Fig. 4.11). The results above may be explained as due to the additional strain energy in

comparison to stress-free, strain-free annealing which is introduced to the metal during stress relaxation by the continued forward plastic flow in response to the elastic stress. The greater stored energy available at incubation hastens the onset of recrystallization (Fig. 4.10). Moreover, its further progress, as shown by micrographs at similar SR and UL annealing times (Fig. 4.20-4.23), is accelerated by the energy differential between the new recrystallized grains and their surroundings being higher in the SR samples. In agreement with this analysis, the acceleration of recrystallization by stress relaxation is associated with reduction in the amount of recovery. In evidence of this the area between the MICR and MECH curves is smaller in SR than in UL tests (Fig. 4.10 and 4.11). This reduction of area between MICR and MECH progresses from IA to IIA and presumably to IB where the difficulty in procuring microscopic evidence leads hypothetically to an approximate coincidence between the SR MECH and MICR curves (Fig. 4.10). This is confirmed by the fact that the p and k values of MECH and MICR measurements of the SR tests are not as far apart as those of the UL ones (IA and IIA in Table 4.4).

The deformation conditions which give reduced differences between SR and UL are clearly conditions which have reduced recovery prior to recrystallization as

evidenced by the diminished difference between the MECH and MICR curves in Fig. 4.10 and 4.11. As discussed in Section 5.1.1 for UL and Section 5.1.2 for SR, the reduced recovery at higher ε and T is indicated by the increased slope of the softening curves and the higher p and the lower k derived from them. The retarding influence of SR is thus more effective when it can operate over a longer period of recovery as in IA. The reduced amount of recovery at higher T and higher $\dot{\varepsilon}$ arise because the formation of nuclei due to heterogeneous recovery is speeded up either by the greater thermal activation or by denser substructure. The imposition of the elastic stress and the resulting continued plastic flow in the same direction as the initial deformation causes hardening events which would not take place in the absence of such stress. The reduced recovery rate due to SR is further confirmed by the lower value of s in Fig. 4.44. The reduced recovery continues even after recrystallization commences because the remaining regions of substructure continue to support a large fraction of the load and hence a higher stress (above the average value) than the recrystallized regions. The effect of SR does not alter the final grain size in similarity to the effect of raising the temperature but in distinction from increase in strain rate which does increase the number of grains per unit volume.

5.1.5 Comparison with Other Work

5.1.5.1 Effect of Decreased Strain on Restoration Kinetics

In comparison to the present tests deformation at Z_1 to a strain of only 0.05 (Section 2.1.3) leads to a much slower softening and to a separation of recovery and recrystallization as indicated by the occurrence of a plateau as recovery slows down and as recrystallization nucleates (32). SR decreases the rates of both recovery and recrystallization and also the saturation level of recovery (Fig. 5.1). The differences between UL and SR are more noticeable at higher temperature which is the opposite of the behaviour at the high strain. At 500°C the difference in the amount of softening between the UL and SR tests at the plateau is about 20% compared with 8% at 450°C (Fig. 5.1).

The recovery in UL is more rapid at 500°C as shown by a higher rate constant s in Eqn. (2.24). It is also more extensive reaching 35% at 500°C and 25% at 450°C. Although the recovery is greater in UL and the initial driving force less, recrystallization proceeds more rapidly in UL as evidenced by the higher values of p and k. In detail, values for p of 1.4 in both the SR and UL tests at 450°C and of 1.3 in the SR one at 500°C also suggests an important contribution of recovery to the total softening. On the other hand, a p of 2.0 in the UL 500°C case shows

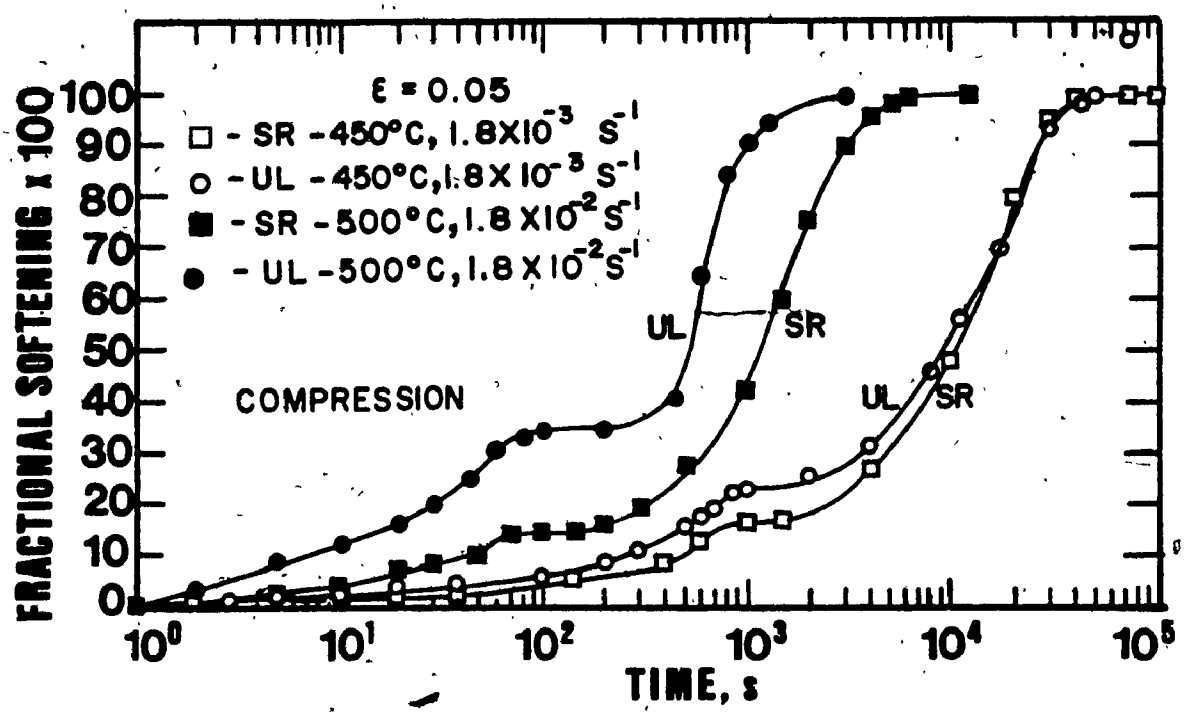

Fig. 5.1 Evolution of softening with load-free and stress relaxation annealing after compression to $\varepsilon = 0.05$ (Z_1, $\sigma_m \sim$ 60 MPa) (32).

that the influence of recovery is much reduced. This is the opposite of the high strain results. It thus appears that there is more recovery occurring in the SR during recrystallization than in the UL. One may argue that this arises because the stress has fallen to a very low value less than half the σ_{SRST} in the high strain tests (Figs. 5.2 and 5.3). After this low strain and high recovery the substructure is much less dense so that the driving force and recrystallization rate are very much less, than in present tests.

5.1.5.2 Restoration under Creep or Constant Strain Rate

Annealing under stress-free conditions allows softening to take place by dislocations moving away from obstacles under the influence of either the back stress inside the subgrains or the forward stress in the sub-boundaries. In the absence of applied stress these dislocation rearrangements result in no hardening events. In stress relaxation, the stress continues to be applied which leads to some forward plastic strain replacing the elastic one. Such dislocation movements in the forward direction lead to hardening events. The applied stress is reduced by the small strain, so that some dislocations move under the internal stresses to attain some softening events. After that little recovery, the applied stress moves additional dislocations and causes additional hardening

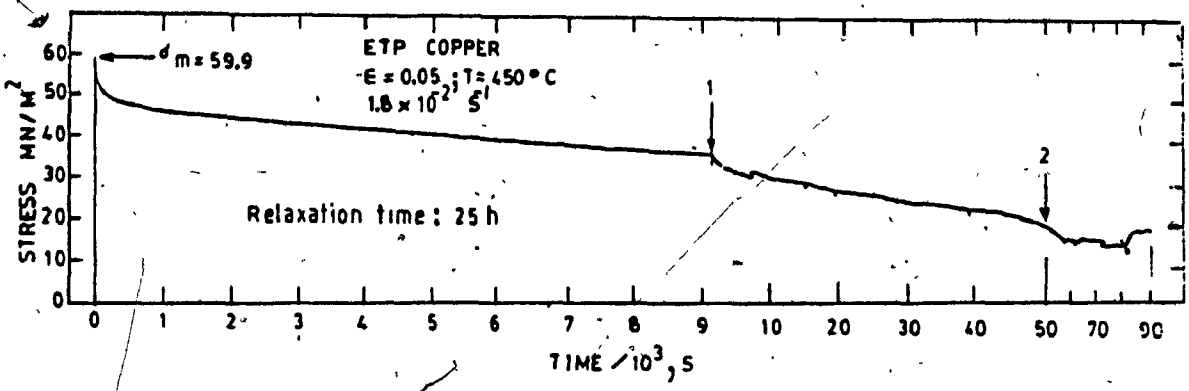

Fig. 5.2 Stress relaxation curve after $\varepsilon = 0.05$ at 450°C, 1.8×10^{-3} s^{-1} (Z_1). Points 1 and 2 denote changes in the chart speed (32).

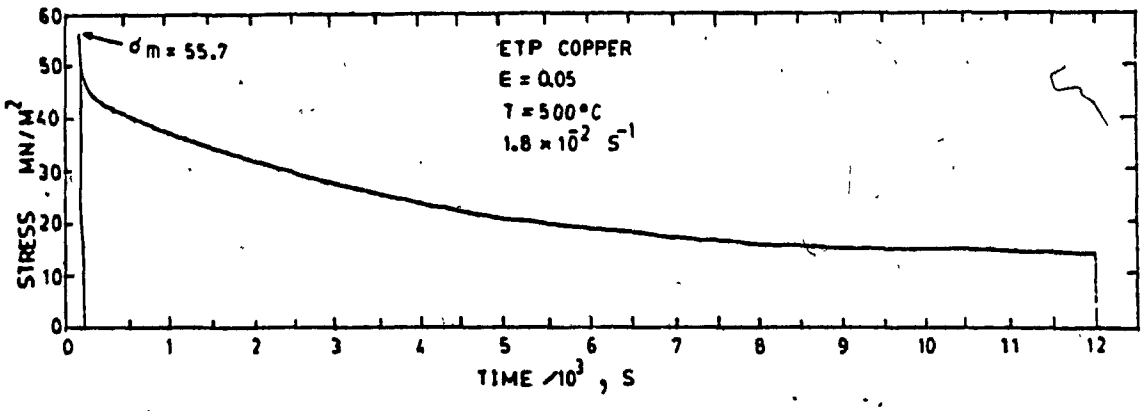

Fig. 5.3 Stress relaxation curve after $\varepsilon = 0.05$ at 500°C, 1.8×10^{-2} s^{-1} (Z_1) (32).

events. The heterogeneous nature of the dislocation substructure and stress fields allows these opposing effects to take place in different yet neighbouring regions. While the stress is high there are thus less softening events and more hardening per unit time than in the stress-free case. When the stress becomes much lower the rate of softening could become higher than in simple annealing because it is then similar to 'stress annealing'.

In the stress annealing experiments, the constant stress, much less than the strength, causes the metal to creep-soften as the substructure alters towards the weaker, more recovered, lower density, larger dimensioned subgrains characteristic of the applied stress. The increased recovery leads to a retardation of recrystallization. This is similar to the present observations that recrystallization is retarded by the lower dislocation density generated by UL holding over stress relaxation, by low strain rate over high and by low strain (0.05) over high (0.15). Within the limits of the stress annealing experiments, increasing the stress in Al always raised the recovery and pushed back the recrystallization, ultimately inhibiting it. In the case of Cu, increasing the stress within a limited range enhanced recovery and retarded recrystallization, but beyond that limit, recovery was reduced and recrystallization enhanced in a manner similar

to that observed in stress relaxation. Because of its low stacking fault energy, dynamic or static recovery in Cu is never as easy as in Al and hence reduces the possibility of enhancing it by stress applied during annealing.

CHAPTER 6

CONCLUSIONS

1. Recovery and recrystallization take place under both stress relaxation and load-free annealing. Recovery both precedes the recrystallization and continues in parallel with it until completion of softening.

2. Total softening and recrystallization obey the Mehl-Avrami relationship. However, the value of p is lower for softening than for SRX because of recovery in the former.

3. Recovery obeys an exponential kinetic law. Recovery was more extensive at the lowest $\dot{\varepsilon}$ and T even though it was faster at higher $\dot{\varepsilon}$ and T.

4. Stress relaxation decreases the rate and amount of recovery. The differences in the amounts of softening due to recovery of the SR and UL samples decrease with rises in temperature and strain rate.

5. Stress relaxation raises the rate of recrystallization (nucleation and growth) determined metallographically. The difference in the recrystallization rates of the SR and UL samples diminishes with increases in

temperature and strain rate due to the decreased influence of recovery under those conditions. For similar conditions (σ_m), the new recrystallized grains are about the same size for both SR and UL annealing independent of the deformation mode.

6. Stress relaxation reduces the time to reach full softening at all the deformation conditions in both compression and torsion. The Avrami constant p is higher for SR than for UL because of the reduced recovery.

7. The stress relaxation curve is able to indicate the completion of recrystallization and in some cases the onset of recrystallization. The fractional relaxation is only approximately related to either the fractional softening or the fraction recrystallized.

8. In industrial processes where tension is exerted on the strip as between one mill stand and either the next one or the coiler, or in continuous annealing, a low stress is likely to retard recrystallization whereas a high one would enhance it. High stresses should be used with caution since they could seriously distort the strip after it has softened.

REFERENCES

1. J.C. Maxwell, Phil.Mag., 35 Series 4 (1868) 129.
2. U.F. Kocks, A.S. Argon and M.F. Ashby, Progr. Mater. Sci., 19 (1975) 260.
3. P. Feltham, Phil. Mag., 6 (1961) 259.
4. P. Groh and R. Conte, Acta Met., 19 (1971) 895.
5. K. Okazaki and Y. Aono, Z. Metallk., 68 (1977) 368.
6. T.O'D. Hanley, A.S. Krausz and D. Maheshwari, Mater. Sci. Eng., 16 (1974) 155.
7. P. Feltham, Phil. Mag., 6 (1961) 847.
8. G. A. Sargent, Acta Met., 13 (1965) 663.
9. I. Gupta and J. C. M. Li, Met. Trans., 1 (1970) 2323.
10. V.I. Dotsenko and A.I. Landau, Mater. Sci. Eng., 22 (1976) 101.
11. E.C. Aifantis and W.W. Gerberich, Mater. Sci. Eng., 21 (1975) 107.
12. Yu. Z. Estrin and V.L. Indenbom, Scripta Met., 10 (1976) 613.
13. B.J. Shaw and G.A. Sargent, Acta Met., 11 (1964) 1225.
14. G.B. Gibbs, Phil. Mag., 13 (1966) 317.
15. J. Kubat and M. Rigdahl, Mater. Sci. Eng., 24 (1976) 223.
16. L.N. Bystrov and S.N. Shakhmaev, Phys. Stat. Sol., 34(a) (1976) k187.
17. G. B. Gibbs, Scripta Met., 17 (1966) 317.
18. A. Fox, J. Mat., 6 (1971) 422.
19. A. Fox, J. Test. Eval., 2 (1974) 32.

20. A. Fox and E.O. Fuchs, J. Test. Eval., 6 (1978) 211.

21. I.A. Oding, V.S. Ivanova, V.V. Burdukskii and V.N. Geminov, "The Creep and Stress Relaxation of Metals", Oliver and Boyd, London (1965).

22. I.A. Oding and V.Z. Tseitlin, Doklady Akad. Nauk USSR, 71 (5) (1950).

23. I.A. Oding and E.N. Volosatova, Doklady Akad. Nauk USSR, 71 (4) (1950).

24. I.A. Oding and E.N. Volosatova, Voprosy Mashinovedeniya, (Problems in Engineering), Izd. Akad. Nauk USSR, (1950) 446.

25. G.A. Sargent, G. Jones and H. Conrad, Scripta Met., 3 (1969) 481.

26. W.A. Wood and J.W. Suiter, J. Inst. Metals, 80 (1951) 501.

27. G.R. Wilms, J. Inst. Metals, 83 (1954-55) 427.

28. J.H. Auld, R.I. Garrod and T.R. Thomson, Acta Met., 5 (1957) 741.

29. P.H. Thornton and R.W. Cahn, J. Inst. Metals, 89 (1960-61) 455.

30. A.H. Ucisik, I. Weiss, H.J. McQueen and J.J. Jonas, Can. Met. Quart., 19 (1980) 351.

31. P.J. Wray, Met. Trans., 6A (1975) 1197.

32. L. Vazquez, Master's Thesis, McGill University, Montreal, Canada (1980).

33. M.F. Ashby and H.J. Frost, "Constitutive Equations in Plasticity", ed. A.S. Argon, The MIT Press, Cambridge, MA. (1975), Chapter 4, 117.

34. H. Mecking, "Work Hardening in Tension and Fatigue", ed. A.W. Thompson, Met. Soc. AIME, Warrendale, PA (1977) 67.

35. A.A. Solomon, C.N. Ahlquist and W.D. Nix, Scripta Met. 4 (1970) 231.

36. H. Mecking and G. Gottstein, "Recrystallization of Metallic Materials", ed. F. Haessner, Dr. Riederer Verlag, Stuttgart (1978), Chapter 9, 17.

37. H.J. McQueen and J.J. Jonas, "Treatise on Materials Science and Technology", Vol.6: "Plastic Deformation of Materials", ed. R.J. Arsenault, Academic Press, N.Y. (1975), 393.

38. D. Hardwick and W.J. Mcg. Tegart, J. Inst. Met., 90 (1961-62) 17.

39. P.R. Swann, "Electron Microscopy and Strength of Crystals", Interscience Publishers, N.Y. (1963), Chapter 3, 135.

40. F. Garofalo, "Fundamentals of Creep and Creep-Rupture in Metals", Macmillan, N.Y. (1965).

41. G. Glover and C.M. Sellars, Met. Trans., 4 (1973) 765.

42. U.F. Kocks, H.S. Chen, D.A. Rigney and R.J. Schaefer, "Work Hardening", eds. J.P. Hirth and J. Weertman, Gordon and Breach, N.Y. (1968), 151.

43. J.F. Bell, Phil. Mag., 10 (1964) 107.

44. M.J. Luton and J.J. Jonas, Proc. 2nd. Int. Conf. Strength of Metals and Alloys, ASM, Metals Park, OH (1970), 1110.

45. J.P. Immarigeon, Ph.D. Thesis, McGill University, Montreal, Canada (1974).

46. H. Lacks, C.D. Wiseman, O.D. Sherby and J.E. Dorn, J. Appl. Mech., ASME, 24 (1957) 207.

47. J.L. Uvira and J.J. Jonas, Trans. TMS-AIME, 242 (1968) 1619.

48. J.P. Immarigeon and J.J. Jonas, Acta Met., 19 (1971) 1053.

49. R.A. Reynolds and W.J. Mcg. Tegart, J. Iron Steel Inst., 200 (1962) 1044.

50. C. Rossard and P. Blain, Mem. Sci. Rev. Met., 56 (1959) 285.

51. D.J. Abson and J.J. Jonas, J. Nucl. Mat., 42 (1972) 73.

52. H. Ormerod and W.J. McG. Tegart, J. Inst. Met., 92 (1963-64) 297.

53. R. Leguet, D. Whitwham and J. Herenguel, Mem. Sci. Rev. Met., 59 (1962) 649.

54. R.A. Petkovic, M.J. Luton and J.J. Jonas, Can. Met. Quart., 14 (1975) 137.

55. M.J. Luton and C.M. Sellars, Acta Met., 17 (1969) 1033.

56. J.P. Sah, G.J. Richardson and C.M. Sellars, J. Aust. Inst. Met., 14 (1969) 292.

57. R.A. Petkovic Djaic and J.J. Jonas, Met. Trans., 4 (1973) 621.

58. G. Glover and C.M. Sellars, Met. Trans., 3 (1972) 2271.

59. J.H. Nichols and P.G. McCormick, Met. Trans., 1 (1970) 3469.

60. G.J. Richardson, C.M. Sellars and W.J. McG. Tegart, Acta Met., 14 (1966) 1225.

61. M.J. Luton and J.J. Jonas, Can. Met. Quart., 11 (1972) 79.

62. I.A. Oding, O.V. Sorokin and N.N. Sazonova, Doklady Akad Nauk USSR, 92 (3) (1953).

63. E. Johnson, "Pipe Flanges Research Committee Third Report", Proc. Inst. Mech. Engrs., 168 (1954) 423.

64. J.D. Lubahn and R.P. Felgar, "Plasticity and Creep of Metals", John Wiley and Sons, N.Y. (1961).

65. K.K. Kanter, Trans. AIME, 143 (1938) 57.

66. C.M. Sellars and W.J.McG. Tegart, Mem. Sci. Rev. Met., 63 (1966) 731.

67. H. Conrad and W.D. Robertson, Trans. AIME, 209 (1957) 503.

68. F. Garofalo, Trans. AIME, 227 (1963) 351.

69. C. Zener and J.H. Hollomon, J. Appl. Phys., 15 (1944) 22.

70. J. Hollomon, Trans. AIME, 171 (1947) 355.

71. J.E. Dorn, A. Goldberg and T.E. Tietz, Trans. AIME, 180 (1949) 205.

72. E.W. Hart, Acta Met., 18 (1970) 599.

73. E.W. Hart, Trans. ASME, 78 (1976) 193.

74. H. Yamada and C.Y. Li, Met. Trans., 4 (1973) 2133.

75. A. Seeger, Phil. Mag., 1 (1956) 651.

76. H. Conrad, Mater. Sci. Eng., 6 (1970) 265.

77. G.I. Taylor, J. Inst. Met., 62 (1938) 307.

78. U.F. Kocks, Acta Met., 6 (1958) 85.

79. G.I. Taylor, Proc. R. Soc., A145 (1934) 362.

80. M.J. Luton and J.J. Jonas, Proc. 3rd. Int. Am. Conf. Mater. Tech., (1972) 910.

81. R.A. Petkovic, Ph.D. Thesis, McGill University, Montreal, Canada (1975).

82. D.H. Sastry, M.J. Luton and J.J. Jonas, Phil. Mag., 30 (1974) 115.

83. J.J. Jonas, J. Sci. Ind. Res., 32 (1973) 528.

84. T. Hasegawa and U.F. Kocks, Acta Met., 27 (1979) 1705.

85. R.E. Cook, G. Gottstein and U.F. Kocks, J. Mater. Sci., 18 (1983) 2650.

86. S. Mader, Ref. 39, Chapter 4, 183.

87. P.B. Hirsch, "Internal Stresses and Fatigue in Metals" Elsevier, N.Y. (1958), 139.

88. J.W. Steeds and P.M. Hazzledine, Discussions Faraday Soc., 38 (1964) 103.

89. J.T. Fourie and R.J. Murphy, Phil. Mag., 7 (1962) 1617.

90. U. Essmann, Phys. Stat. Sol., 3 (1963) 932.

91. S.J. Basinski and Z.S. Basinski, "Recrystallization, Grain Growth and Textures", ASM, Metals Park, OH. (1966), Chapter 1, 1.

92. W.G. Truckner and D.E. Mikkola, Met. Trans., 8A (1977) 45.

93. W.C. Leslie, J.T. Michalak and F.W. Aul, "Iron and Its Dilute Solid Solutions", ed. C.W. Spencer and F.E. Werner, Wiley Interscience, N.Y. (1963) 119.

94. P. Gay and A. Kelly, Acta Cryst., 6 (1953) 185.

95. A. Howie, "Direct Observation of Lattice Defects in Crystals", Interscience, N.Y. (1962), 283.

96. D.L. Holt, J. Appl. Phys., 41 (1970) 3197.

97. A. Kelly, Acta Cryst., 7 (1954) 554.

98. R.L. Segal and P.G. Partridge, Phil. Mag., 4 (1959) 912.

99. D.H. Warrington, Proc. Europ. Reg. Conf. Electron Microscopy, Delft, Nederlandse (1961), 354.

100. W.A. Wong, H.J. McQueen and J.J. Jonas, J. Inst. Met., 95 (1967) 129.

101. H.J. McQueen and J.E. Hocket, Met. Trans., 1 (1970) 2997.

102. H.J. McQueen and S. Bergerson, Met. Sci., 6 (1972) 25.

103. G. Langford and M. Cohen, Trans. ASM, 62 (1969) 623.

104. I.L. Dillamore, P.L. Morris, C.J.E. Smith and N.B. Hutchison, Proc. R. Soc., A239 (1972) 405.

105. H. Hu, "Recovery and Recrystallization of Metals", ed. L. Himmel, Intescience Publishers, N.Y. (1962), 311.

106. R.D. Doherty, Ref. 36, Chapter 3, 23.

107. T. Hasegawa, T. Yakov and U.F. Kocks, Acta Met., 30 (1982) 235.

108. J.J. Jonas and I. Weiss, Met. Sci., 13 (1979) 238.

109. F.J. Humphreys, Met. Sci., 13 (1979) 136.

110. H.J. McQueen and K. Conrod, AIME Symp. N.Y. (1985) to be published.

111. J. Sankar, D. Hawkins and H.J. McQueen, Met. Tech., 6 (1979) 325.

112. N.D. Ryan, H.J. McQueen and J.J. Jonas, Can. Met. Q., 22 (1983) 369.

113. C. Imbert, N.D. Ryan and H.J. McQueen, Met. Trans., 15A (1984) 1855.

114. J.K. Kivilahti, V.K. Lindroos and B. Lehtinen, "High Voltage Electron Microscopy", ed. P.R. Swann et.al., Academic Press, N.Y. (1974) 195.

115. L.S. Darken and R.W. Gurry, "Physical Chemistry of Metals", McGraw Hill, N.Y. (1953).

116. R. Drouard, J. Washburn and E.R. Parker, Trans. AIME, 197 (1953) 1226.

117. J.C.M. Li, Ref. 91, Chapter 2, 45.

118. W. Betteridge, J. Inst. Met., 82 (1953-54) 149.

119. E.C.W. Perryman, Met. Trans. AIME, 203 (1955) 1053.

120. M.J. Luton, R.A. Petkovic and J.J. Jonas, Acta Met., 28 (1980) 729.

121. D. Kuhlmann, G. Masing and J. Raffelsieper, Z. Metallk., 40 (1949) 241.

122. J.T. Michalak and H.W. Paxton, Trans. AIME, 221 (1961) 850.

123. U.F. Kocks and H. Mecking, "Strength Metals and Alloys", ed. P. Haasen, Pergamon, Oxford (1979), Vol. 1, 345.

124. P. Feltham, J. Inst. Met., 89 (1961) 210.

125. F. Haessner, Ref. 36, Chapter 1,1.

126. J. Schey, Acta Tech. (Budapest), 16 (1957) 131.

127. R.A. Petkovic, M.J. Luton and J.J. Jonas, Met. Sci., 13 (1979) 569.

128. E. Hornbogen and U. Koster, Ref. 36, Chapter 8, 159.

129. J.R. Porter and F.J. Humphreys, Met. Sci., 13 (1979) 83.

130. P.R. Mould and P. Cotteril, J. Mat. Sci., 2 (1967) 241.

131. O. Dimitrov, R. Fromageau and C. Dimitrov, Ref. 36, Chapter 7, 137.

132. R. Fromageau, Mem. Sci. Rev. Met., 66 (1969) 287.

133. P.A. Beck and P.R. Sperry, J. Appl. Phys., 21 (1950) 150.

134. P. Gordon, Trans. AIME, 203 (1955) 1043.

135. J.E. Bailey, Ref. 39, Chapter 10, 535.

136. W.A. Johnson and R.F. Mehl, Trans. AIME, 135 (1939) 416.

137. I.M. Avrami, J. Chem. Phys., 7 (1939) 1103.

138. I.M. Avrami, ibid., 8 (1940) 212.

139. R.A. Vandermeer and P. Gordon, Ref. 105, 211.

140. G. Gottstein and U.F. Kocks, Acta Met., 31 (1983) 188.

141. P.J.T. Stuitje and G. Gottstein, Z. Metallk., 71 (1980) 279.

142. J.J. Jonas, H.J. McQueen and W.A. Wong, "Deformation Under Hot Working Conditions", Iron Steel Inst., London (1968) 49.

143. V.K. Lindroos and H.M. Miekk-Oja, Phil. Mag., 16 (1967) 593; 17 (1968) 119.

144. J.J. Jonas and T. Sakai, "Deformation, Processing and Structure", ed. G. Krauss, ASM, Metals Park, Ohio (1982), 185.

145. L. Blaz, T. Sakai and J.J. Jonas, Met. Sci., 17 (1983) 609.

146. T. Maki, K. Akasaka and I. Tamura, "Thermomechanical Processing of Microalloyed Austenite", ed. P.J. Wray and A.J. DeArdo, AIME, Warrendale, PA (1982), 217.

147. C. Ouchi and T. Okita, Trans. Iron Steel Inst., Japan, 22 (1982) 543.

148. T. Sakai, M.G. Akben and J.J. Jonas, Acta Met., 31 (1983) 631.

149. K.J. Gardner and R. Grimes, Met. Sci., 13 (1979) 216.

150. J. Hausselt and W. Blum, Acta Met., 24 (1976) 1027.

151. W.D. Nix and B. Ilschner, Ref. 123, Vol. 2, 1503.

152. W. Blum and H. Schmidt, Res. Mech., 9 (1983) 105.

153. W. Blum and A. Finkel, Acta Met., 30 (1982) 1705,

154. I. Weiss, Ph.D. Thesis, McGill University, Montreal, Canada (1978).

155. T. Sheppard and M.G. Tutcher, Met. Tech., 8 (1981) 481.

156. H.J. McQueen, E. Evangelista, J. Bowles and G. Crawford, Met. Sci., 18 (1984) 395.

157. M.J. Luton, J.P.A. Immarigeon and J.J. Jonas, J. Phys. E. Sci. Inst., 7 (1974) 862.

158. S. Fulop, K.C. Cadien, M.J. Luton and H.J. McQueen, J. Test. Eval., 5 (1977) 419.

159. D.S. Fields and W.A. Backoffen, ASTM Proc., 57 (1957) 1259.

160. M.J. Luton, Ph.D. Thesis, McGill University, Montreal, Canada (1971).

161. G. Canova, Master's Thesis, McGill University, Montreal, Canada (1975).

162. D. Hanson and M.A. Wheeler, J. Inst. Met., 45 (1931) 229.

163. D. McLean, J. Inst. Metals, 80 (1951-52) 507.

164. H.J. McQueen and J.J. Jonas, "Metal Forming, Interrelation Between Theory and Practice", ed. A.L. Hoffmanner, Plenum Press, N.Y. (1971), 393.

165. W.J. McG. Tegart, "Elements of Mechanical Metallurgy", MacMillan Co., N.Y. (1968).

166. M.G. Akben, Ph.D. Thesis, McGill University, Montreal, Canada (1980).

167. G. Dieter, "Mechanical Metallurgy", McGraw Hill, N.Y. (1976), 361.

168. J.J. Jonas, C.M. Sellars, W.J.McG. Tegart, Met. Rev., 14 (1969) 1.

169. C. Rossard, Proc. 3rd. Int. Conf. Strength Metals and Alloys, Pergamon Press, Oxford (1972), 175.

170. L.C. Lovell and J.H. Wernick, J. Appl. Phys., 30 (1959) 590.

171. J.E. Hilliard and J.W. Cahn, Trans. AIME, 221 (1961) 344.

172. J.E. Hilliard, "Quantitative Microscopy", ed. R.T. DeHoff and F.N. Rhines, McGraw Hill, N.Y. (1968), 45.

173. M.H. Loretto, "Defect Analysis in Electron Microscopy" Chapman and Hall, London (1975).

174. R.W. Evans and G.R. Dunstan, J. Inst. Met., 99 (1971) 4.

175. J. Gronostajski, E. Pulit and H. Ziemba, Met. Sc. 17 (1983) 348.

APPENDIX A

ADDITIONAL EXPERIMENTAL DATA

Table A-1. Reloading Stresses and Fractional Softenings for UL Annealing after Compression

Test Conditions	t_{UL} s	σ MPa	X %
IA	1.4	77.1	8.0
MPa	5.4	62.3	39.0
$\bar{\sigma}_o$ = 35.1	10.4	47.6	71.0
$\bar{\sigma}_m$ = 80.8	20.0	39.0	92.0
	40.0	32.1	107.0
IB	13	77.9	6.0
$\bar{\sigma}_o$ = 33.4	16	77.6	6.6
$\bar{\sigma}_m$ = 80.8	62	75.4	12.0
	112	73.0	16.7
	140	70.5	21.3
	170	69.2	24.5
	212	65.0	34.0
	412	58.6	49.5
	600	45.2	74.3
	1000	33.6	102.0
IIA	4.0	100.5	0.0
	10.0	98.7	3.0
$\bar{\sigma}_o$ = 43.1	20.0	95.1	9.6
	25.0	92.6	14.4
$\bar{\sigma}_m$ = 100.5	30.0	87.9	22.7
	60.0	72.4	48.0
	100.0	57.4	73.0
	200.0	41.5	102.9

Table A-2. Reloading Stresses and Fractional Softenings for UL Annealing after Torsion

Test Conditions	t_{UL} s	σ_r MPa	X %
IIB UL	10.0	62.0	40.0
MPa	20.0	47.8	59.0
$\bar{\sigma}_o$ = 17.7	40.0	31.6	81.0
	80.0	23.5	92.0
$\bar{\sigma}_m$ = 91.2	120.0	20.0	97.0
IIB SR	2.0	80.8	14.0
	10.0	53.1	51.9
$\bar{\sigma}_o$ = 17.7	20.0	35.5	75.7
	80.0	24.1	91.3
$\bar{\sigma}_m$ = 91.2	100.0	20.0	96.8
III UL	2.0	64.4	37.3
$\bar{\sigma}_o$ = 32.8	4.0	58.0	50.0
$\bar{\sigma}_m$ = 83.2	8.0	44.1	77.6
	16.0	38.2	89.4
IV UL	10.0	67.6	42.6
$\bar{\sigma}_o$ = 23.9	20.0	48.6	67.6
$\bar{\sigma}_m$ = 100.0	30.0	35.0	85.6